

Numerical Investigation of Tidal Processes and Phenomena in the Weddell Sea, Antarctica

Dissertation
zur Erlangung des Grades eines
Doktors der Naturwissenschaften
– *Dr. rer. nat.* –

dem Fachbereich Physik der
Universität Bremen
vorgelegt von

Adriene Ferreira Pereira

13. Dezember 2001

1. Gutachter: Prof. Dr. Dirk Olbers
2. Gutachter: PD Dr. Aike Beckmann

Tag des Promotionskolloquiums: 21.01.2002

Abstract

In the framework of the BRIOS (*Bremerhaven Regional Ice Ocean Simulations*), a three-dimensional tidal model was developed to investigate tidal processes in the southern Weddell Sea. The model is based on the free surface SCRUM (*S-Coordinate Primitive Equation Ocean Model*), modified to allow for the inclusion of the horizontal component of the Earth's rotation vector, the equilibrium tide and ice shelves.

Barotropic tides are simulated in a regional two-dimensional (x-y) configuration for the Atlantic Sector of the Southern Ocean. In this investigation, the semidiurnal M_2 and S_2 and the diurnal K_1 and O_1 frequencies are considered. For both semidiurnal constituents, maxima amplitudes are found in the southwestern corner of the Filchner-Ronne Ice Shelf (FRIS). Diurnal tides have higher amplitudes at the continental shelf break where they excite continental shelf waves of same period propagating in the along-slope direction.

With the full three-dimensional model, baroclinic tidal currents are studied in the inner Weddell Sea, using an orthogonal curvilinear 3D grid. Semidiurnal and diurnal periods are considered, although the emphasis is on the superinertial frequencies at which free propagating internal tides can be generated at the latitude range of the inner Weddell Sea. The vertical structure of tidal currents in the southern continental shelf region and beneath FRIS are described in detail, including their seasonal variability. The model results show that tidal currents contribute significantly to the turbulent mixing at the shelf break of the southern Weddell Sea and beneath FRIS. They also suggest that tides have a direct effect on both water mass formation through mixing and on water mass modification through heat transport to the upper boundary layer, in the ice shelf cavities and by opening leads in the sea ice.

Zusammenfassung

Im Rahmen des BRIOS (*Bremerhaven Regional Ice Ocean Simulations*) wurde ein drei-dimensionales Gezeitenmodell entwickelt, um die Gezeitenprozesse im südlichen Weddellmeer zu untersuchen. Das auf SCRUM (*S-Coordinate Primitive Equation Ocean Model*) basierende Modell mit freier Oberfläche wurde modifiziert, um die horizontale Komponente des Erdrotationsvektors, die Gleichgewichtsgezeit und die Schelfeisgebiete zu berücksichtigen.

Die halbtägigen M_2 und S_2 sowie die eintägigen K_1 und O_1 Gezeitenfrequenzen werden mit einem zwei-dimensionalen (x-y) Modell für den atlantischen Sektor des Südlichen Ozeans simuliert. Für beide halbtägigen Komponenten werden maximale Amplituden in der südwestlichen Ecke des Filchner-Ronne-Schelfeises (FRIS) gefunden. Eintägige Gezeiten haben die höchsten Amplituden am Kontinentalschelfhang, wo sie Kontinentalschelfwellen gleicher Periode entlang des Hanges anregen.

Mit dem drei-dimensionalen Modell werden barokline Gezeitenströme im inneren Weddellmeer mit einem orthogonal kurvilinearen 3D-Gitter untersucht. Neben halb- und eintägigen Gezeitenperioden werden hauptsächlich superkritische Frequenzen untersucht, bei denen frei propagierende interne Gezeitenwellen für den Breitenbereich des inneren Weddellmeer erzeugt werden können. Die vertikale Struktur der Gezeitenströme in der südlichen Kontinentalschelfregion sowie unter FRIS werden im Detail beschrieben; die jahreszeitliche Variabilität wird dabei berücksichtigt. Die Modellergebnisse zeigen, daß Gezeitenströme einen wichtigen Beitrag zur turbulenten Vermischung am Schelfhang des südlichen Weddellmeeres und unter FRIS leisten. Ferner haben Gezeiten einen direkten Einfluss auf die Wassermassenbildung aufgrund von Vermischung sowie auf die Modifikation der Wassermassen durch Wärmetransport in die obere Grenzschicht in den Schelfeiskavernen und durch die Erzeugung von offenen Rinnen in der Meereisbedeckung.

Acknowledgements

This thesis was written at Alfred-Wegener Institute for Polar and Marine Research (AWI) with the support of Prof. Dr. Dirk Olbers and Prof. Dr. Dieter Wolf-Gladrow. I would like to thank both for giving me the chance to develop this work.

My special thanks goes to PD Dr. Aike Beckmann and Dr. Hartmut Hellmer which were my "day-to-day" advisors. I am grateful for all their help, questions and answers on each day during the development of this work. Both read draft versions of this thesis, making constructive comments to improve it. Several times, Aike helped me to modify the numerical code, having patience enough to teach me and answer all my questions. Hartmut always gave his assistance, including encouraging my husband and me to come to Germany.

Several other people made big and small contributions to this work. I want to thank Dr. Ralph Timmermann to provide the initial density fields employed in the three-dimensional simulations. Ralph was always willing to give advice, to have discussions about the effect of tides on sea ice (and vice versa) and always had 'two minutes' for me (at the end it was probably some hours). Dr. Leo Maas from the Netherlands Institute for Sea Research (NIOZ) helped to interpret the gyroscopic waves obtained in the model results. Dr. Eberhard Fahrbach provided current meter, temperature and salinity data that were used in the first attempts to simulate baroclinic tides in the Weddell Sea and Gerd Rohard converted them to a readable format. Haika Fischer analyzed these current meter data that were used for the model comparison. Chresten Wübbert took care (and much care) of the computer where all my data were stored and also Wolfgang Cohrs made sure that printers and my workstation were always running. To all of you, thanks a lot !

To my colleagues and friends from the BRIOS Group, a big thank you to provide a good atmosphere, especially Inga Hense, Karen Assmann and Dr. Christian Mohn. Inga always had a nice word to say when incentive was necessary.

Last but not least, I want to thank André L. Belém. Obrigada por sempre estar ao meu lado me dando seu apoio e seu carinho. Fico feliz em termos superado juntos mais esta fase de nossas vidas a qual foi também de muito aprendizado para nós dois.

Contents

| | |
|--|------------|
| Abstract | i |
| Zusammenfassung | iii |
| List of Figures | xv |
| 1 Introduction | 1 |
| 1.1 Barotropic and Baroclinic Tides | 2 |
| 1.2 Tides in the Weddell Sea | 4 |
| 2 The Numerical Model | 11 |
| 2.1 System of Equations | 11 |
| 2.1.1 Quasi-nonhydrostatic equations | 12 |
| 2.2 Boundary conditions | 18 |
| 2.3 Horizontal and vertical discretization | 20 |
| 3 Barotropic Tides | 23 |
| 3.1 2D-Model (X-Y) Configuration | 23 |
| 3.1.1 Model domain, grid resolution and bathymetry | 23 |
| 3.1.2 Subgrid-scale parameterization | 24 |
| 3.1.3 Time step, time integration and harmonic analysis | 25 |
| 3.2 Dataset Available for Comparison | 26 |
| 3.2.1 Free surface elevation measurements | 26 |
| 3.2.2 Velocity measurements | 27 |
| 3.3 Barotropic Tides at Diurnal Frequencies: K_1 and O_1 | 27 |
| 3.3.1 Diurnal elevation amplitudes and Greenwich phases | 27 |

| | | |
|----------|--|-----------|
| 3.3.2 | Diurnal barotropic currents | 31 |
| 3.3.3 | Diurnal tidal energy flux | 32 |
| 3.4 | Barotropic Tides at Semi-diurnal Frequencies: M_2 and S_2 | 33 |
| 3.4.1 | Semidiurnal elevation amplitudes and Greenwich phases | 33 |
| 3.4.2 | Semidiurnal barotropic currents | 35 |
| 3.4.3 | Semidiurnal tidal energy flux | 37 |
| 3.5 | Barotropic Residual Currents | 39 |
| 3.6 | Summary | 41 |
| 4 | Baroclinic Tides | 43 |
| 4.1 | Linear Internal Wave Theory and Critical Latitude | 43 |
| 4.2 | X-Z Pilot Study of the Grid Resolution | 46 |
| 4.2.1 | The vertical grid spacing | 47 |
| 4.2.2 | The horizontal grid spacing | 48 |
| 4.3 | 3D-Model Configuration | 51 |
| 4.3.1 | Model domain, grid resolution and bathymetry | 51 |
| 4.3.2 | Subgrid-scale parameterization | 52 |
| 4.3.3 | Model initialization and time step | 55 |
| 4.4 | Density Field and its Seasonal Variation | 56 |
| 4.5 | Generation and Propagation of Internal Tides | 59 |
| 4.6 | Surface Tides in the 3D-Model | 61 |
| 4.7 | Baroclinic Tides at the M_2 Frequency | 62 |
| 4.7.1 | M_2 tidal currents on the continental shelf and at the shelf break | 63 |
| 4.7.2 | M_2 tidal currents beneath Filchner-Ronne Ice Shelf | 73 |
| 4.8 | Baroclinic Tides at the S_2 Frequency | 79 |
| 4.8.1 | S_2 tidal currents on the continental shelf and at the shelf break | 79 |
| 4.8.2 | S_2 tidal currents beneath Filchner-Ronne Ice Shelf | 81 |
| 4.9 | Baroclinic Residual Currents | 84 |
| 4.10 | Summary | 87 |
| 5 | Tidally Induced Mixing | 89 |
| 5.1 | Computation with M_2 and S_2 Tidal Constituents | 89 |

| | | |
|----------|--|------------|
| 5.2 | Combined Effects of Semidiurnal and Diurnal Tidal Constituents | 94 |
| 5.3 | Computation for a Cross-Slice (y-z) Domain | 98 |
| 5.4 | Summary | 100 |
| 6 | Conclusions and Outlook | 103 |
| A | Current Meter Data | 111 |
| B | Tidal Ellipse Complex Demodulation | 113 |
| C | The Effect of the \tilde{f}-Terms in the Model Results | 115 |
| D | Stability Functions in the MY2.5 Scheme | 117 |
| E | Gyroscopic Waves | 119 |

List of Figures

| | | |
|------|--|----|
| 1.1 | Map of the Weddell Sea and bathymetry of the region | 5 |
| 2.1 | Scheme for the vertical topography and ice shelf base-following discretization . | 21 |
| 3.1 | Weddell Sea grid (BRIOS4.3). | 24 |
| 3.2 | Ice shelves and islands of the Weddell Sea as represented by BRIOS4.3 | 25 |
| 3.3 | Spatial distribution of current meters and tide gauges observations in the Weddell Sea | 26 |
| 3.4 | Diurnal tidal amplitudes (cm) and Greenwich phase (degrees) obtained with the grid 4.3 | 28 |
| 3.5 | Representation of continental shelf waves in a coarser grid | 29 |
| 3.6 | Correlation between modeled and observed diurnal amplitudes for the Weddell Sea | 30 |
| 3.7 | K_1 barotropic tidal ellipses | 31 |
| 3.8 | Correlation between modeled and observed diurnal major axis of the tidal ellipse for the Weddell Sea | 32 |
| 3.9 | O_1 tidal energy flux (W m^{-1}) along the inner Weddell Sea | 33 |
| 3.10 | Semidiurnal tidal amplitudes (cm) and Greenwich phase (degrees) obtained with the grid 4.3 | 34 |
| 3.11 | Comparison between observations and modeled tidal amplitudes (cm) obtained with the grid 4.3 | 34 |
| 3.12 | Correlation between modeled and observed semidiurnal amplitudes for the Weddell Sea | 35 |
| 3.13 | M_2 barotropic tidal ellipses | 36 |

| | |
|--|----|
| 3.14 Correlation between modeled and observed semidiurnal major axis of the tidal ellipse for the Weddell Sea | 37 |
| 3.15 M_2 tidal energy flux ($W m^{-1}$) along the inner Weddell Sea | 38 |
| 3.16 Barotropic residual currents ($m s^{-1}$) in the Weddell Sea | 39 |
| 3.17 Barotropic residual currents ($m s^{-1}$) beneath FRIS | 40 |
| 4.1 Idealized shelf-slope topography | 46 |
| 4.2 Contours of overturning stream function obtained by Craig [1987] | 47 |
| 4.3 Investigation of the vertical grid resolution. Overturning stream function ($m^2 s^{-1}$) computed considering a horizontal grid spacing of 625 m | 48 |
| 4.4 Investigation of the horizontal grid resolution. Overturning stream function ($m^2 s^{-1}$) computed considering 25 s-levels, non-equidistantly distributed over the water column | 49 |
| 4.5 Investigation of the horizontal grid resolution considering typical slope and buoyancy frequency of the southern Weddell Sea. Overturning stream function ($m^2 s^{-1}$) computed considering 25 s-levels, non-equidistantly distributed over the water column | 50 |
| 4.6 Inner Weddell Sea grid (BRIOS4.4). | 52 |
| 4.7 Water column thickness, ice shelves and islands of the inner Weddell Sea as represented by BRIOS4.4 | 53 |
| 4.8 Summer and winter vertical stratification (potential density, $kg m^{-3}$) in the southern Weddell Sea | 56 |
| 4.9 Schematic representation of the distribution of water masses in the southern Weddell Sea | 57 |
| 4.10 Vertical profiles of Brunt-Väisälä frequency (s^{-2}) for summer and winter from the slope of the southern Weddell Sea | 58 |
| 4.11 Along- (F_x) and cross-slope (F_y) internal tide forcing function ($10^5 Nm^2$) . . . | 59 |
| 4.12 Distribution of meridional gridlines in the 3D-model domain and location of the M_2 critical latitude | 61 |
| 4.13 Ratio γ related to the M_2 frequency plotted together with bottom topography . | 62 |
| 4.14 Ratio γ related to the S_2 frequency plotted together with bottom topography . . | 63 |

| | |
|--|----|
| 4.15 Tidal amplitudes (cm) and Greenwich phase (degrees) obtained with the grid 4.4 | 64 |
| 4.16 Major axis of the M_2 tidal ellipse (cm s^{-1}) considering summer stratification across vertical slices (y-z) in the southern Weddell Sea | 66 |
| 4.17 Comparison between modeled and observed tidal ellipses at the FRIS edge . . . | 67 |
| 4.18 Phase of the M_2 tidal ellipse for the slices indicated in the inset showing the westward propagation of the internal tide | 68 |
| 4.19 Amplitude of the M_2 vertical displacement (m) considering summer stratifica- tion across the vertical slices (y-z) in the southern Weddell Sea | 69 |
| 4.20 Comparison of M_2 decomposed tidal ellipses between model (lines) and obser- vations (symbols) at the shelf break | 71 |
| 4.21 Contour of potential density (kg m^3) near the surface over approximately two M_2 tidal cycles | 73 |
| 4.22 Position of y-z slices for which model results are shown beneath FRIS | 73 |
| 4.23 Major axis of the M_2 tidal ellipse (cm s^{-1}) considering summer stratification across vertical slices (y-z) beneath Filchner-Ronne Ice Shelf | 75 |
| 4.24 Comparison between modeled and observed tidal ellipses beneath Filchner- Ronne Ice Shelf | 76 |
| 4.25 Vertical profiles of the magnitude of the two components of the decomposed M_2 tidal currents at three different points beneath FRIS | 77 |
| 4.26 Polarization of M_2 tidal ellipses at the base of the Filchner-Ronne Ice Shelf . . | 77 |
| 4.27 Polarization of M_2 tidal ellipses along two y-z slices beneath Filchner-Ronne Ice Shelf | 78 |
| 4.28 Major axis of the S_2 tidal ellipse (cm s^{-1}) considering summer stratification across vertical slices (y-z) in the southern Weddell Sea | 80 |
| 4.29 Comparison of S_2 decomposed tidal ellipses between model (lines) and obser- vations (symbols) at the shelf break | 81 |
| 4.30 Major axis of the S_2 tidal ellipse (cm s^{-1}) considering summer stratification across vertical slices (y-z) beneath Filchner-Ronne Ice Shelf | 83 |
| 4.31 Vertical profiles of the magnitude of the two components of the decomposed S_2 tidal currents in three different points beneath FRIS | 84 |

| | | |
|------|---|-----|
| 4.32 | Polarization of S_2 tidal ellipses at the base of the Filchner-Ronne Ice Shelf . . . | 84 |
| 4.33 | Polarization of S_2 tidal ellipses along two y-z slices beneath Filchner-Ronne Ice Shelf | 85 |
| 4.34 | Baroclinic residual flows (cm s^{-1}) beneath FRIS | 86 |
| 4.35 | Baroclinic residual flow (cm s^{-1}) and its seasonal difference (cm s^{-1}) in a y-z slice | 86 |
| 5.1 | Summer mean (20 days) eddy viscosity coefficients ($\text{m}^2 \text{s}^{-1}$) at the shelf break region of the southern Weddell Sea, considering M_2 and S_2 forcing | 90 |
| 5.2 | Winter mean (20 days) eddy viscosity coefficients ($\text{m}^2 \text{s}^{-1}$) at the shelf break region of the southern Weddell Sea, considering M_2 and S_2 forcing | 91 |
| 5.3 | Summer mean (20 days) eddy viscosity coefficients ($\text{m}^2 \text{s}^{-1}$) beneath Filchner- Ronne Ice Shelf, considering M_2 and S_2 forcing | 93 |
| 5.4 | Summer mean (20 days) eddy viscosity coefficients ($\text{m}^2 \text{s}^{-1}$) at the shelf break region of the southern Weddell Sea, considering the eight main tidal constituents | 95 |
| 5.5 | Power spectral density of the vertical eddy viscosity | 96 |
| 5.6 | Summer mean (20 days) eddy viscosity coefficients ($\text{m}^2 \text{s}^{-1}$) beneath Filchner- Ronne Ice Shelf, considering eight tidal constituents in the forcing | 97 |
| 5.7 | Major axis of the M_2 tidal ellipse cm s^{-1} obtained considering a 2D cross-slope domain | 98 |
| 5.8 | Mean vertical eddy viscosity $\text{m}^2 \text{s}^{-1}$ obtained by forcing the numerical model only with the M_2 frequency and using (a) the 3D approach and (b) considering a 2D cross-slope domain | 99 |
| 6.1 | Schematic representation of regions and processes of tidally induced vertical mixing in the southern Weddell Sea | 105 |
| 6.2 | Percentage of lead formation | 108 |
| B.1 | Decomposition of a tidal current ellipse | 113 |
| C.1 | Major axis of the M_2 tidal ellipse (cm s^{-1}) obtained including (a) and not in- cluding (b) \tilde{f} in the model equations | 115 |
| D.1 | Stability functions according to Galperin <i>et al.</i> [1988] | 118 |

| | | |
|-----|---|-----|
| E.1 | M_2 major axis (cm s^{-1}) in a homogeneous ocean obtained including (a) and not including (b) \tilde{f} in the model equations | 119 |
| E.2 | Amplitude of the M_4 cross-slope component (cm s^{-1}) in a homogeneous ocean obtained not considering \tilde{f} in the model equations | 120 |

Chapter 1

Introduction

The regular tidal movements of coastal seas must have challenged human imagination from earliest times. Indeed, the ancients who were able to link the regular movements of the sea to the movements of the Sun and the Moon regarded tides as a tangible terrestrial manifestation of the power of the celestial gods. Posidonius (135-51 BC) gave the first reasonably correct and detailed account of the tides at Gades (actual Cádiz, Spain) from personal observations and accounts by unnamed local people [Cartwright, 1999]. Several centuries later, many famous mathematicians like Nikolaus Copernicus, Galileo Galilei, Johannes Kepler and René Descartes made inestimable contributions to the theory of tides. But it was only after the law of gravitation, established by Isaac Newton (1642-1727) and the *Mécanique Céleste* by Pierre Simon, Marquis de Laplace, that tides became amenable to theoretical analyses.

Although the theory of tides has been proved only in the 17th century, accurate temporal predictions have been available for certain sites (usually ports) for centuries. Tides are unique among natural physical processes in that one can predict their motions well into the future with acceptable accuracy without knowing anything about their physical mechanism. When Darwin (1809-1882) first formulated the rules of harmonic tide prediction, he virtually produced a cook-book recipe for producing tide-tables for a given place without requiring any reference to Laplace's tidal equations or any kind of hydrodynamical law [Godin, 1972].

Along the world's coasts, the fluctuations of sea level are quite well known and well measured. However, despite many ingenious mathematical solutions and numerical techniques pioneered by Hansen [1949], only few observations were available and no cotidal chart of the global ocean was produced until the beginning of the 1980's decade. It was only recently after the onset of satellite altimetry (i.e. GEOSAT in March 1985) that tides in the open ocean could

be measured, providing unique, almost global tide observations [Kantha, 1995].

Nowadays, the interest in tides is not only to know with high accuracy the tidal elevation of the sea surface and the tidal velocities for any given time and place in the oceans but also, to understand their effects and consequences. Tides have a considerable practical importance, interfering with many other environmental sciences. Tides slowly dissipate the gravitational energy resident in the Earth-Moon system and cause Earth to spin down ever so slightly (about 2 milliseconds per century) and the orbital radius of the Moon to increase by about 3.7 cm every year [Wahr, 1988]. This secular trend is important to astronomy and geophysics. Accurate determination of oceanic tides is germane to understand the inner working of Earth's core [Wahr, 1988]. Tides provide much of the energy for mixing and the accompanying vertical circulation of the deep ocean [Munk, 1966], probably playing an important role in the long-term climate variability [Egbert and Ray, 2000]. All of these effects and many others are still subject of intensive studies.

1.1 Barotropic and Baroclinic Tides

Motions at tidal frequency in the ocean are often composed of a surface (barotropic) tide and an internal (baroclinic) tide. The barotropic tides are the periodic elevations of the sea surface, always observed by man at beaches and ports. They result from the gravitational attraction of the Moon and Sun acting on the rotating Earth. There are related phenomena that occur in the solid Earth and the atmosphere called earth tides and atmospheric tides. Barotropic tides have maximum vertical displacements at the sea surface and have horizontal currents uniform over the whole water column, except for a frictional layer near the sea floor. The theory of tides developed in early years explains this mode that is the astronomically driven movement.

The baroclinic tides were first observed in the ocean by Petterson [1907] who found that a substantial fraction of internal motions (i.e. vertical motion of isopycnal surfaces) in the Kattegat (passage between Denmark and Sweden) were at tidal periods. Internal tides have since been observed in many places of the world ocean, both in mid-ocean and near coasts over continental shelves and slopes [Huthnance, 1989; 1995]. Internal tidal amplitudes can reach 30 m from crest to trough, deforming isopycnals, but the corresponding sea surface height fluctuations reach only a few centimeters. The thousands of years delay in their recognition is the result of the need to have instruments capable of detecting subsurface temperature or

density changes, a development that had to await the invention of Nansen bottles and reversing thermometers.

The wavelengths of the internal and surface tides differ considerably. Roughly, the length scale of the surface tide is some thousands of kilometers while the internal tide is some tens of kilometers. Because of the very short natural wavelength and large amplitude of the baroclinic tides, there is no possibility of a simple coupling of the internal tides with the surface tides, or with the astronomical forcing [Munk and Wunsch, 1998].

Zeilon [1934] was the first to show experimentally that a continental shelf-like topography is an effective generator of internal waves. The motion of the horizontal barotropic tidal currents over variable bottom topography generates vertical motions which create horizontal pressure gradients in the stratified ocean. These are unbalanced and, therefore, act to generate internal waves of the same frequency. Thus, mid-ocean ridges, seamounts and shelf breaks may constitute prime generation sites of internal tides [Kantha and Tierney, 1997; Holloway and Merrifield, 1999]. Various estimates [Wunsch, 1975; Hendershott, 1981] indicate that the global baroclinic tidal energy may be as much as 10-50% of the barotropic tidal energy. While the energy of internal tides is usually a fraction of that in barotropic tides, the currents are of similar magnitude.

The resultant transfer of energy from long barotropic tidal scales to much shorter internal motions is important to mixing and energetics of the interior of the ocean. Internal tides produce shear in the water column that can lead to enhanced dissipation and mixing. Although only a small fraction of the barotropic tidal energy is lost to the internal tide, a large fraction of this internal energy may be available for mixing [Kantha and Tierney, 1997]. In fact, indications are that internal tides may be a dominant source of deep ocean mixing [Munk and Wunsch, 1998; Laurent and Garrett, 2001].

The length scale of the barotropic tides is set by the external Rossby radius of deformation ($R_D = \sqrt{gH}/|f|$, where g is gravity, H is the total water depth, and f the Coriolis parameter) which varies from hundred kilometers in shelf seas to thousands of kilometers in the deep ocean. The wavelength of internal tides, however, is defined by the combined effects of the topographic scale and stratification, usually of the order of the internal Rossby radius of deformation ($R_i = NH/|f|$, where N the Brunt-Väisälä frequency), typically two orders of magnitude smaller than the scale of the barotropic tides.

Such small scale waves can be affected significantly by background currents. In general, baroclinic tides are distorted and rapidly dissipated as they propagate away from their source. Thus, one can expect significant internal tide energy only in the immediate vicinity of topographic features, although there is evidence that the first mode internal tide can propagate many hundred [Hendry, 1977] to one or two thousands of kilometers [Schott, 1977] before its energy is either dissipated or transferred to other frequencies by nonlinear interactions.

Internal tidal mixing affects sediment transport, nutrient and plankton distribution, acoustic propagation, and optical clarity. Additionally, the well-mixed waters produced by internal wave action have been observed to spread laterally along isopycnals into deep water [Ivey and Nokes, 1989]. This lateral spreading has been proposed as a mechanism that might weaken stratification of the ocean interior and account for the large effective eddy diffusivities of $O(10^{-4} \text{ m}^2 \text{ s}^{-1})$ required to explain the mass and heat balances in abyssal plains [Eriksen, 1985]. Besides mixing produced by internal tides, the interaction of barotropic tides with bottom topography increases turbulence in the water column without necessarily the generation of an internal wave. This happens through enhanced near-seabed current shear.

1.2 Tides in the Weddell Sea and Beneath Filchner-Ronne Ice Shelf

Since the 18th century, many scientists have speculated on whether the tides in the Southern Ocean of any species may have special characteristics owing to the uninterrupted, circumpolar extension of the ocean. Whewell [1833] argued that the directly driven tides of the Southern Ocean were the source for Atlantic tides, which were 'derivative' tides. Whewell further argued that the 1-2 days lag between the time of new moon and of maximum spring tidal range (age of the tide) of the semidiurnal tide in the North Atlantic was a consequence of the time necessary for the wave to propagate from the Southern Ocean. Measurements made in June 1835 on both sides of the Atlantic for a fortnight at 28 places [Whewell, 1836], forced Whewell to abandon his earlier ideas and to prepare a chart only for the north-west European continental shelf [Pugh, 1987].

Whewell's studies were the first attempt to derive the tides in the Southern Ocean. One century later, after the launch of TOPEX/Poseidon in August 1992 and, to a lesser extent, after the launch of ERS-1 a year earlier, several tidal global models were developed (see Andersen and Flather, 1995; Shum *et al.*, 1997, for a list of them). The reason for the proliferation of

such models is due to the fact that the tidal signal in altimetric data is the largest contributor to the sea surface height variability and accounts for more than 80% of the signal variance [Ray, 1993]. This signal must be extracted in order to retrieve the geostrophic surface signature of the ocean circulation. Despite the coarse resolution grids used in global tidal models, their results provided the first tidal charts for the Southern Ocean, and consequently, for the Weddell Sea (Fig. 1.1).

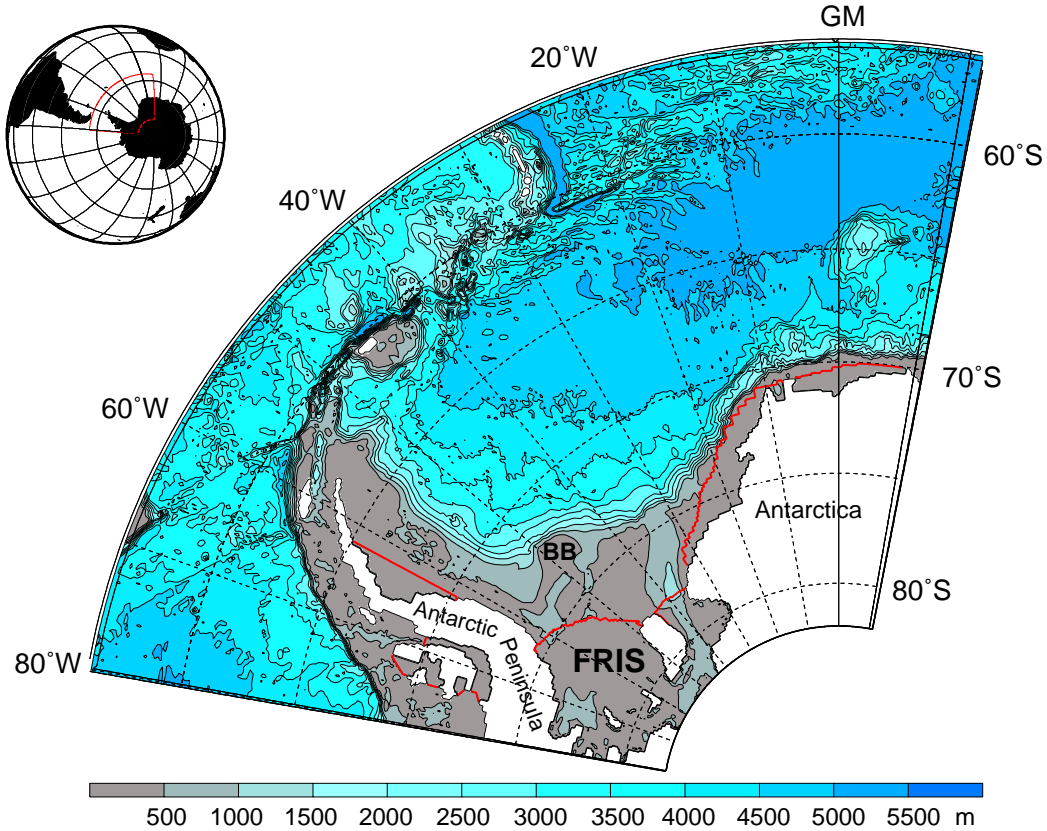


Figure 1.1: Map of the Weddell Sea and bathymetry of the region. The ice shelf boundaries are drawn with a red line and Filchner-Ronne Ice Shelf (FRIS) and General Belgrano Bank (BB) are indicated. All depths are in meters and contour interval is 500 m. Under the ice shelves, depth represents water column thickness.

The sinking of high density water in the Southern Ocean significantly contributes to the Global Thermohaline Circulation, a key component in the regulation of the Earth's climate [Gordon, 1986; Broecker, 1987]. The Weddell Sea has long been recognized as being the major site of Antarctic Bottom (AABW) Water formation and, thus, the predominant source of high density water for the world ocean [Carmack, 1977]. Various estimates of the formation rate of AABW in the Weddell Sea were made [Meredith *et al.*, 2001] and, although an exact value has not been defined until now, the values range between 4.9 [Orsi *et al.*, 1999] to 11 Sv [Mensch *et al.*, 1996].

There are basically two hypotheses concerning the formation of bottom water in the Weddell Sea: Foster and Carmack [1976] suggested that the formation process of high density waters involving a mixture of shelf and/or surface waters and Circumpolar Deep Water (CDW) takes place on the continental shelf, whereas Foldvik *et al.* [1985a] showed that the mixing of different water masses would occur on their way down the continental slope. Several authors speculated about the role of tides in these formation processes. Foldvik *et al.* [1985a] found strong tidal currents ($\approx 20 \text{ cm s}^{-1}$) at the shelf break and suggested tidal mixing as an important mechanism supporting the bottom water formation. Foster *et al.* [1987] suggested that mixing at shelf break would be increased by baroclinic tides at the upper slope. Levine *et al.* [1997] showed that the properties of the plume that flows off the continental shelves to become ultimately AABW will be modified by the increased bottom stirring due to tides.

Middleton *et al.* [1982; 1987] explained the strong diurnal currents at the shelf break of the southern Weddell Sea based on a barotropic continental shelf wave model [Saint-Guilhy, 1976]. These diurnal continental shelf waves would transport the major portion of the eddy heat flux, bringing warmer water from intermediate depths offshore onto the continental shelf [Foster *et al.*, 1987].

Under the Filchner-Ronne Ice Shelf (hereinafter referred as FRIS, Fig. 1.1), High Salinity Shelf Water (HSSW) is modified by the processes at the ice/ocean interface [Foldvik *et al.*, 1985a]. The oscillatory action of tides, tidal divergence, and prevailing winds move the sea ice away from the Filchner-Ronne Ice front and keep a large portion of the ocean surface exposed to the atmosphere which consequentially enhances the production of sea ice and salt release. Mainly in these near-shore leads, HSSW is formed and, following the inclined sea floor, flows underneath the ice shelf. Here, HSSW occupies the lower portion of the water column, and is separated from the ice shelf base by the rising Ice Shelf Water (ISW) except for the grounding line area, where contact with the glacial base initiates its modification to ISW. The latter occurs as part of the upper branch of the "ice pump" [Lewis and Perkin, 1986]. Since the ice cap does not permit any contact between the atmosphere and the ocean, Gill [1973] suggested tidal stirring as a probable mechanism for mixing HSSW up to the ice ocean interface, resulting in melting of the ice shelf base. The same suggestion was made by MacAyeal [1984b] for the Ross Ice Shelf cavity.

Lead formation through tidal divergence occurs, not only near the FRIS edge, but also at the

continental shelf break [Padman and Kottmeier, 2000]. Heat fluxes from ocean to atmosphere are increased by one to two orders of magnitude through the open lead than through the adjacent sea ice [Launiainen and Vihma, 1994]. Due to the consequent sea ice formation and salt flux into the upper ocean, denser water is formed.

With the discoveries of the climatic importance of bottom water formation in the Weddell Sea and the supposed role of tides in this process, a better knowledge of tides in the region was necessary. The key areas for the formation of bottom water are shallow regions which are poorly resolved in global models. Since the resolution reached by this class of models was insufficient, regional tidal models were developed. Genco *et al.* [1994] applied a finite element model to the South Atlantic Ocean and were the first to give a description of M_2 and K_1 amplitude elevations in the Weddell Sea. Smithson *et al.* [1995; 1996] investigated tides in the Weddell Sea and under Filchner-Ronne Ice Shelf, using a finite difference model. Although with finer resolution than Genco *et al.* [1994], they could only reproduce satisfactorily tides under FRIS after increasing the bottom friction coefficient to 50 times the open-ocean value. Thereby, any agreement with observations near the ice shelf edge and in the open ocean was lost. Barotropic tides in the Weddell and Scotia Seas were modeled by Robertson *et al.* [1998]. Their finite difference model included the four major tidal constituents (the semidiurnal M_2 and S_2 and the diurnal K_1 and O_1). Using a high resolution grid (4' latitude and 15' longitude, corresponding to about 7.4 km north-south and 3.4-9 km east-west), Makinson and Nicholls [1999] described in detail barotropic tidal currents under FRIS. All cited studies applied a horizontal, depth-integrated model and did not include baroclinicity. These models provide information about the sea surface elevation and depth mean currents, but give no information about the vertical profile of the tidal current and internal tidal mixing.

In a first attempt to investigate internal tides in the Weddell Sea, Robertson [2001] employed a two-dimensional (x-z directions), cross-shelf model. This model approach does not take into account effects of along-shore variations of the barotropic tide, horizontal density and topographic gradients which may change the characteristics of the internal wave. A three-dimensional tidal model has to be developed which will be one goal of this work.

Although baroclinic tides are supposed to contribute to the energy for mixing in the southern Weddell Sea, they were not observed so far in the region. One reason for this can be the high variability in time and space of the internal tidal field. The internal tide motion is intermittent

(as it is in most places), and this is attributed to varying stratification in the shelf break region on seasonal time-scales. Another reason is the inadequate oceanographic database available for tide investigations. Due to the short wavelength, it is difficult to capture the structure of internal tides with mooring arrays.

The main goal of this work is to provide a better understanding of tidal phenomena and processes in the southern Weddell Sea and beneath Filchner-Ronne Ice Shelf using numerical modeling. Extending two-dimensional model approaches, the use of a three-dimensional tidal model will allow to investigate the internal tide generation, propagation and seasonality, the vertical structure of tidal currents, the bottom boundary layer, and internal mixing in this area.

This work starts with the model description (Chapter 2). The quasi-hydrostatic equations for the external and internal modes are presented, including the equilibrium tide terms. Boundary conditions, the inclusion of the ice shelf cavities into the numerical model, and the horizontal and vertical discretization employed are also described.

The barotropic tides in the Weddell Sea are investigated in Chapter 3 which begins with the description of the model configuration. The available data set used for comparison between model and observations is presented. Details of barotropic tidal velocities, amplitude elevation, residual currents, and energy fluxes are discussed for the semidiurnal M_2 and S_2 and the diurnal K_1 and O_1 tidal constituents. Whenever possible, model results will be compared with observations. The diurnal continental shelf waves, which propagate along the Weddell Sea continental shelf break, are investigated in detail.

The baroclinic results for the M_2 and S_2 tidal frequencies are studied in Chapter 4. It starts with the description of the model configuration used for the three-dimensional model. A pilot study on the grid resolution necessary to have accurate quantitative numerical solutions for internal tides follows, as well as the new three-dimensional grid employed to study the vertical tidal current profile and tidal mixing. The seasonal variability of the internal tide field and the vertical structure of the tidal currents beneath Filchner-Ronne Ice Shelf are investigated. Model results are validated by comparison with observations.

Chapter 5 deals with the tidal mixing in the southern Weddell Sea. A series of sensitivity studies is presented, varying the number of tidal constituents included in the model run. The calculated values of eddy viscosity coefficients are discussed and compared to traditional values accepted for the world oceans to estimate the importance of this mechanism relative to other

mixing processes.

Chapter 6 summarizes the results and presents an outlook for future investigations.

Chapter 2

The Numerical Model

The basis for hydrodynamic modeling of tides are the Navier-Stokes equations, modified to allow for the inclusion of Earth's rotation. In order to simplify this system of equations, approximations are introduced, e.g. incompressibility of the fluid, the Boussinesq and hydrostatic approximations. With these simplifications, the Hydrostatic Primitive Equations (HPE) are formed which are, generally, used in *Ocean General Circulation Models (OGCMs)*.

In the standard numerical model used in this study, the HPE are the full three-dimensional equations for continuity and momentum. Their vertical integration over the water column leads to the two-dimensional equations (the shallow water equations). Both sets of equations are solved in the numerical model using a split-technique to integrate the 2D- (external mode) and the 3D-equations (internal mode) at their respective time steps, a technique usually used in *OGCMs* due to different time scale between barotropic and baroclinic motions. Both system of equations will be presented in this chapter, including details of the numerical model as well modifications introduced to the standard version.

2.1 System of Equations

The numerical model used in this study is based on the S-Coordinate Primitive Equation Ocean Model (SCRUM; Song and Haidvogel [1994]) which, in its standard form, is a hydrostatic primitive equation free surface ocean circulation model. This model uses orthogonal curvilinear coordinates for horizontal discretization and the terrain-following sigma coordinate system for the vertical. For this study, several modifications have been introduced in the model equations:

- addition of the horizontal component of the Earth's rotation vector (\tilde{f});
- inclusion of the equilibrium tide (η_0), and
- inclusion of the ice shelf cavities.

2.1.1 Quasi-nonhydrostatic equations

The hydrostatic approximation assumes an exact balance in the vertical between the pressure gradient force and the gravitational force, thereby excluding the horizontal component of the Earth's rotation vector (\tilde{f}). Recently, some authors reconsidered the inclusion of \tilde{f} -terms in the momentum and pressure gradient equations. Beckmann and Diebels [1994] investigated the inclusion of the horizontal component of the Earth's rotation vector in a study on flow at steep topography. Their results show that in weakly stratified oceans (as high latitude oceans) and at steep topography, where the vertical velocity is large, this term may become important influencing the baroclinic and internal wave motion quite considerably. Baines and Miles [2000] demonstrated that, although the importance of \tilde{f} -terms decreases with increasing distance from the equator, their inclusion increases the barotropic to baroclinic energy conversion and changes the character of the propagating internal tidal wave, specially near the critical latitudes. Since the computational overhead is small and potentially improved results can be expected, the model equations were modified to include the \tilde{f} -terms following Beckmann and Diebels [1994].

In SCRUM, the transformed horizontal coordinates are defined by the relations [Hedström, 1997]

$$(d\mathcal{S})_{\mathcal{X}} = \left(\frac{1}{m}\right) d\mathcal{X} \quad (2.1)$$

$$(d\mathcal{S})_{\mathcal{Y}} = \left(\frac{1}{n}\right) d\mathcal{Y} , \quad (2.2)$$

where $m(x, y)$ and $n(x, y)$ are the scale factors which relate the differential distances ($\Delta\mathcal{X}, \Delta\mathcal{Y}$) to the physical arc lengths $\Delta\mathcal{S}$. The generalized vertical (s) coordinate is

$$s = s \left(\frac{z + \eta(t)}{h} \right) \quad -1 < s < 0 \quad (2.3)$$

where z is depth, η is the free surface elevation, and $h=h(\mathcal{X}, \mathcal{Y})$ is the water column thickness,

and

$$\frac{\partial s}{\partial t} = \Omega(\mathcal{X}, \mathcal{Y}, s, t) = \frac{1}{H_z} \left[w - (1 + s) \frac{\partial \eta}{\partial t} - mu \frac{\partial z}{\partial \mathcal{X}} - nv \frac{\partial z}{\partial \mathcal{Y}} \right], \quad (2.4)$$

where Ω is the vertical velocity in the s -coordinate system and w is the vertical velocity [Haidvogel and Beckmann, 1999]. Under these horizontal and vertical transformations, and with $H_z \equiv \frac{\partial z}{\partial s}$, the resulting nonlinear system of equations for the BRIOS tidal model reads [after Hedström, 1997]:

$$\begin{aligned} & \frac{\partial}{\partial t} \left(\frac{H_z u}{mn} \right) + \frac{\partial}{\partial \mathcal{X}} \left(\frac{H_z u^2}{n} \right) + \frac{\partial}{\partial \mathcal{Y}} \left(\frac{H_z uv}{m} \right) + \frac{\partial}{\partial s} \left(\frac{H_z u \Omega}{mn} \right) \\ & - \left\{ \left(\frac{f}{mn} \right) + v \frac{\partial}{\partial \mathcal{X}} \left(\frac{1}{n} \right) - u \frac{\partial}{\partial \mathcal{Y}} \left(\frac{1}{m} \right) \right\} H_z v + \frac{\tilde{f} H_z}{mn} w = \\ & - \left(\frac{H_z}{n} \right) \left(\frac{\partial P}{\partial \mathcal{X}} + \frac{g \rho}{\rho_o} \frac{\partial z}{\partial \mathcal{X}} + g \frac{\partial \eta}{\partial \mathcal{X}} \right) + \frac{H_z}{mn} (\mathcal{F}_u + \mathcal{D}_u) \end{aligned} \quad (2.5)$$

$$\begin{aligned} & \frac{\partial}{\partial t} \left(\frac{H_z v}{mn} \right) + \frac{\partial}{\partial \mathcal{X}} \left(\frac{H_z uv}{n} \right) + \frac{\partial}{\partial \mathcal{Y}} \left(\frac{H_z v^2}{m} \right) + \frac{\partial}{\partial s} \left(\frac{H_z v \Omega}{mn} \right) \\ & + \left\{ \left(\frac{f}{mn} \right) + v \frac{\partial}{\partial \mathcal{X}} \left(\frac{1}{n} \right) - u \frac{\partial}{\partial \mathcal{Y}} \left(\frac{1}{m} \right) \right\} H_z u = \\ & - \left(\frac{H_z}{m} \right) \left(\frac{\partial P}{\partial \mathcal{Y}} + \frac{g \rho}{\rho_o} \frac{\partial z}{\partial \mathcal{Y}} + g \frac{\partial \eta}{\partial \mathcal{Y}} \right) + \frac{H_z}{mn} (\mathcal{F}_v + \mathcal{D}_v) \end{aligned} \quad (2.6)$$

$$\frac{\partial P}{\partial s} = \tilde{f} H_z u - \left(\frac{g H_z \rho}{\rho_o} \right) \quad (2.7)$$

$$\frac{\partial}{\partial t} \left(\frac{H_z \rho}{mn} \right) + \frac{\partial}{\partial \mathcal{X}} \left(\frac{H_z u \rho}{n} \right) + \frac{\partial}{\partial \mathcal{Y}} \left(\frac{H_z v \rho}{m} \right) + \frac{\partial}{\partial s} \left(\frac{H_z \Omega \rho}{mn} \right) = \frac{H_z}{mn} (\mathcal{F}_\rho + \mathcal{D}_\rho) \quad (2.8)$$

and

$$\frac{\partial}{\partial t} \left(\frac{\eta}{mn} \right) + \frac{\partial}{\partial \mathcal{X}} \left(\frac{H_z u}{n} \right) + \frac{\partial}{\partial \mathcal{Y}} \left(\frac{H_z v}{m} \right) + \frac{\partial}{\partial s} \left(\frac{H_z \Omega}{mn} \right) = 0. \quad (2.9)$$

where (u, v, Ω) are the $(\mathcal{X}, \mathcal{Y}, s)$ components of the velocity vector \vec{v} , ρ is potential density, f and \tilde{f} are the vertical and horizontal components of the Earth's rotation vector respectively ($f = 2\varpi \sin \phi$; $\tilde{f} = 2\varpi \cos \phi$, where ϖ is the angular velocity of the Earth's rotation and ϕ the latitude),

g is gravity and $P(\mathcal{X}, \mathcal{Y}, s, t)$ is the dynamic pressure (p/ρ_0). Forcing and dissipative terms are denoted as \mathcal{F} and \mathcal{D} , respectively. The set of equations includes the Boussinesq approximation, in which deviations from the mean density are considered only when gravitational forces or spatial and temporal variations in density are essential.

Equations 2.5 and 2.6 are the conservation of momentum equations. With the inclusion of the horizontal component of the Earth's rotation vector, the hydrostatic equation (2.7) has an additional term. Equations 2.8 and 2.9 are mass conservation and continuity equations, respectively. The prognostic variables are u , v , Ω , ρ and η . The true vertical velocity w is computed diagnostically from the continuity equation (see Eq. 2.4).

Equilibrium tide and secondary tide-generating forces

The effects of the primary (tidal potential) and the secondary (Earth and loading tides) tide-generating forces were included in the model.

The equilibrium tide theory, developed by Isaac Newton in 1687, is a theoretical concept that assumes that the water covering the face of the Earth instantly respond to the tide-producing forces of the Moon and Sun to form a surface of equilibrium under the action of these forces. The model disregards friction, inertia, and the irregular distribution of the land masses on Earth. The theoretical tide formed under these conditions is known as the equilibrium tide.

The primary tide-generating force is the tidal potential (Π). It is related to the equilibrium tide (η_0) through:

$$\eta_0 = \frac{\Pi}{g}$$

The method of Harmonic Analysis is based on the periodic time dependent behavior of the tides. Following it, the equilibrium tide is decomposed into a series of harmonic partial tides which can reach up to 400 constituents. Usually, for tidal prediction purposes, a simplified spectrum is used keeping only the two major diurnal (K_1 and O_1) and the two major semidiurnal (M_2 and S_2) constituents (Table 2.1). Although the relative strengths of tidal constituents vary with location, these four constituents generally account for about 70-80% of the total tidal elevation [Pond and Pickard, 1978] and are the dominant frequencies in the tidal spectrum in the southern Weddell Sea [Foldvik *et al.*, 1990].

Following Schwiderski [1980], the decomposition can be written as:

$$\eta_0(\phi, \lambda, t) = \sum_{j,n} B_{jn} L_j(\phi) \cos(\sigma_{jn} t + j\lambda + \chi_{jn})$$

where j and n correspond to the tidal specie and tidal constituent, respectively; B_{jn} and σ_{jn} are the equilibrium amplitude and phase, χ_{jn} is the astronomical argument, and ϕ and λ are colatitude (defined as distance from the north pole in degrees) and longitude relative to the Greenwich Meridian. L_j is the geodesic coefficient defined as:

$$\begin{aligned} L_1 &= \sin(2\phi) && \text{for diurnal species, and} \\ L_2 &= \sin^2(\phi) && \text{for semidiurnal species.} \end{aligned}$$

Then the general equation for diurnal (ζ_1) and for semidiurnal (ζ_2) species are:

$$\eta_1(\phi, \lambda, t) = \sum_{1,n} B_{1n} \sin(2\phi) \cos(\sigma_{1n} t + j\lambda + \chi_{1n})$$

$$\eta_2(\phi, \lambda, t) = \sum_{2,n} B_{2n} \sin^2(\phi) \cos(\sigma_{2n} t + j\lambda + \chi_{2n})$$

Table 2.1 lists the parameter values.

Table 2.1: Constants of the Major Tidal Modes

| Constituent | Tidal Mode | B , m | σ , $10^{-4} s^{-1}$ | χ , deg |
|-------------|-----------------------------|----------|-----------------------------|-------------------|
| K_1 | Declination luni-solar | 0.141565 | 0.72921 | $h_0 + 90$ |
| O_1 | Principal diurnal lunar | 0.100514 | 0.67598 | $h_0 - 2s_0 - 90$ |
| M_2 | Principal semidiurnal lunar | 0.242334 | 1.40519 | $2h_0 - 2s_0$ |
| S_2 | Principal solar | 0.112841 | 1.45444 | 180 |

where h_0 and s_0 are the mean longitude of the Sun and the Moon at Greenwich midnight.

Assuming that the solid Earth responds to tidal forcing as an elastic body and in phase, the tide-generating potential and the Earth tide are usually (as carried out by Flather [1987] and Foreman *et al.* [1993]) expressed as $\alpha g \eta_0$ in the depth-integrated shallow water momentum

equations, where

$$\alpha = 1 + k - h$$

with $k=0.302$, $h=0.609$ as the Love numbers relating the body Earth tide (and associated perturbations) to the tidal potential [Wahr, 1981].

In accordance with Pekeris and Accad [1969], the ocean loading tide (the deformation of the elastic earth due to the redistribution of mass in the ocean tide) is assumed to be in phase with the ocean tide, and a fixed percentage of that value (usually 5.4%). As the load tide is expected to have a relatively minor influence, more accurate calculations of that value [e.g., Francis and Mazzega, 1990; Hendershott, 1972] were not considered. For a detailed description of the theory and the parameters above described see Schwiderski [1980].

The vertical component of the tidal potential is of the order of 10^{-7} and is equivalent to a slight increase or reduction in g [Bowden, 1983]. Due to its small value, it can be neglected. Thus, barotropic horizontal currents, caused by the rise and fall of the ocean surface, are the result of the astronomical forcing. For this reason, terms relative to the equilibrium tide will only appear in the 2D-equations which are described next.

The external mode

Surface gravity waves propagate at $C = (gH)^{\frac{1}{2}}$. Therefore, these waves usually impose a shorter timestep than any of the internal processes. The fully three-dimensional model requires, for computational economy, special treatment of the fast barotropic (external) mode and its coupling to the slower baroclinic (internal) mode. This is achieved by a technique called mode-splitting [see, e.g. Haidvogel and Beckmann, 1999], which separates the external and internal mode equations and solving each of them separately at the appropriate time steps, dictated by the respective gravity wave speeds. This technique ensures that the two calculations are consistent and synchronous with each other.

The depth average of a quantity A is given by:

$$\overline{A} = \frac{1}{H} \int_{-1}^0 h A ds$$

where the overbar denotes a vertically averaged quantity and

$$H = \eta(\mathcal{X}, \mathcal{Y}, t) + h(\mathcal{X}, \mathcal{Y})$$

is the total depth of the water column. Then, the vertically integrated equations are [after Hedström, 1997]:

$$\begin{aligned} & \frac{\partial}{\partial t} \left(\frac{H\bar{u}}{mn} \right) + \frac{\partial}{\partial \mathcal{X}} \left(\frac{H\bar{u}\bar{u}}{n} \right) + \frac{\partial}{\partial \mathcal{Y}} \left(\frac{H\bar{u}\bar{v}}{m} \right) - \left(\frac{Hf\bar{v}}{mn} \right) \\ & - \left\{ \bar{v}\bar{v} \frac{\partial}{\partial \mathcal{X}} \left(\frac{1}{n} \right) - \bar{u}\bar{v} \frac{\partial}{\partial \mathcal{Y}} \left(\frac{1}{m} \right) \right\} H - \left\{ \frac{\partial H\bar{u}}{\partial \mathcal{X}} + \frac{1}{2} \frac{\partial H\bar{v}}{\partial \mathcal{Y}} \right\} \frac{\tilde{f}}{mn} = \\ & - \left(\frac{H}{n} \right) \left(\beta g \frac{\partial \eta}{\partial \mathcal{X}} - \alpha g \frac{\partial \eta_0}{\partial \mathcal{X}} \right) + \frac{H\bar{\mathcal{D}}_{hu}}{mn} - \frac{\tau_b^{\mathcal{X}}}{mn} \end{aligned} \quad (2.10)$$

$$\begin{aligned} & \frac{\partial}{\partial t} \left(\frac{H\bar{v}}{mn} \right) + \frac{\partial}{\partial \mathcal{X}} \left(\frac{H\bar{u}\bar{v}}{n} \right) + \frac{\partial}{\partial \mathcal{Y}} \left(\frac{H\bar{v}\bar{v}}{m} \right) + \left(\frac{Hf\bar{u}}{mn} \right) \\ & + \left\{ \bar{u}\bar{v} \frac{\partial}{\partial \mathcal{X}} \left(\frac{1}{n} \right) - \bar{u}\bar{u} \frac{\partial}{\partial \mathcal{Y}} \left(\frac{1}{m} \right) \right\} H - \left\{ \frac{1}{2} \frac{\partial H\bar{u}}{\partial \mathcal{Y}} \right\} \frac{\tilde{f}}{mn} = \\ & - \left(\frac{H}{m} \right) \left(\beta g \frac{\partial \eta}{\partial \mathcal{Y}} - \alpha g \frac{\partial \eta_0}{\partial \mathcal{Y}} \right) + \frac{H\bar{\mathcal{D}}_{hv}}{mn} - \frac{\tau_b^{\mathcal{Y}}}{mn} \end{aligned} \quad (2.11)$$

$$\frac{\partial}{\partial t} \left(\frac{\eta}{mn} \right) + \frac{\partial}{\partial \mathcal{X}} \left(\frac{H\bar{u}}{n} \right) + \frac{\partial}{\partial \mathcal{Y}} \left(\frac{H\bar{v}}{m} \right) = 0. \quad (2.12)$$

where $(\bar{u}, \bar{v})(\mathcal{X}, \mathcal{Y}, t)$ are the components of the depth-averaged horizontal velocity vector \vec{v} , $\eta(\mathcal{X}, \mathcal{Y}, t)$ is the surface elevation, $\eta_0(\mathcal{X}, \mathcal{Y}, t)$ is the equilibrium tidal elevation corresponding to the astronomical Moon and Sun forcing, α and β are the parameters to account for the Earth and loading tides ($\alpha=0.693$ and $\beta=0.946$), $\bar{\mathcal{D}}_{hu,v}$ is the horizontal viscosity and τ_b is the bottom stress term. All other variables are defined as before.

Equations 2.10 and 2.11 are the depth-integrated shallow water momentum equations and equation 2.12 is the vertically integrated continuity equation. The prognostic variables are \bar{u} , \bar{v} and η .

2.2 Boundary conditions

Tidal elevations

At the open boundary of a regional model domain, tidal elevation is prescribed as a boundary condition for η (free surface elevation). The model in this study is forced with a barotropic tidal wave computed with tide height coefficients obtained from the model TPXO.5 [Egbert and Erofeeva, 2000]. TPXO.5 is a global inverse model for barotropic ocean tides which assimilates TOPEX/POSEIDON altimeter data and is a significantly improved version of TPXO.3 [Egbert *et al.*, 1994]. Its solution fits the altimetry data significantly better than previous coarse global barotropic tidal models [Egbert and Erofeeva, 2000]. The tide height coefficients were determined through harmonic analysis of its state solution. Some subroutines were adapted and implemented into the BRIOS tidal model.

The tidal elevation for a given point in time and space can be computed as a sum of n partial tides of each single constituent ($n_{max} = 10$). Thus, it is possible to use for the open boundary forcing only those constituents which are interesting for this study. For the investigation of barotropic tides in the Weddell Sea (Chapter 3), the four main tidal constituents (M_2 , S_2 , K_1 and O_1) were included in the open boundary forcing; the same included in the equilibrium tide (Subsection 2.1.1). For the study of the baroclinic tides (Chapter 4), only the semidiurnal M_2 and S_2 were used.

Radiation and free-slip condition

For the barotropic flow normal to the boundaries, a radiation condition is applied at the open boundary:

$$\bar{v}_\perp = \bar{v} + \frac{C}{H}(\eta - \eta_{forc})$$

where \bar{v}_\perp is the radiated depth mean current, η_{forc} is the prescribed free surface elevation, \bar{v} and η are the normal component of the barotropic tidal current and the elevation calculated in the actual timestep, $C = (gH)^{\frac{1}{2}}$ is the phase speed and H is the total water column thickness, including the instantaneous sea surface elevation. By using a radiation condition, the velocity is not clamped on the open boundary, and waves can propagate out of the region. Vertically averaged currents parallel to boundaries are subject to a free-slip condition.

Flow-relaxation scheme condition

In order to avoid reflection of offshore propagating internal gravity waves at the open boundary, a flow relaxation scheme [Martinsen and Engedahl, 1987] is applied for the baroclinic flow and potential density. The relaxation zone consists of the last five grid points at the northern boundary of the grid domain. The relaxation scheme updates the prognostic variables v and ρ by the equation:

$$QR_i = a_i Q_b + (1 - a_i) Q_c, \quad i = 1, 2, \dots, 5$$

where QR_i and Q_c are the variable relaxed and unrelaxed values, respectively, Q_b is the boundary ($i = 1$) value. In this application, the baroclinic velocity is relaxed to zero ($Q_b = 0$) and the density to the initial value ($Q_b = \rho_{init}$). a is a relaxation parameter which varies quadratically from 0.04 to 1 within the relaxation zone:

$$a_i = \left(\frac{6 - i}{5} \right)^2.$$

Inclusion of ice shelf cavities

Ice shelves are assumed to float freely and, thus, having the same surface elongation as the ocean beneath. This treatment is invalid only in the so-called "hinge zone" between the grounded ice sheet and the floating ice shelf that accommodate differential movement and suffers cyclic flexure at the tidal frequency [Holdsworth, 1977]. Ice shelf flexure may have a significant influence on tidal wave propagation and tidal energy dissipation [Doake, 1978] within a few kilometers (approximately between 1.5 and 5 km) of the ice shelf grounding line [Vaughan, 1995]. However, considering the grid resolution employed in this numerical study (see Subsections 3.1.1 and 4.3.1), this effect is considered to be minor. The elastic strength of the ice shelf and its inertia with respect to vertical motions are disregarded in this study. Ice shelf flexure in both horizontal directions (beam-like at the hinge zones, two-dimensional for ice shelf center and edge) is also not taken into account.

The pressure gradient term in equations 2.5 and 2.6 was modified to allow for the inclusion of the ice shelf cavities. Basically, the same modifications described in Beckmann *et al.* [1999] were made. The quasi-hydrostatic pressure at the base of the ice shelf is required to compute

the horizontal pressure gradient in the model. Assuming that the ice shelf is in isostatic equilibrium, this pressure can be approximated by the integral over the depth of the reference density profile:

$$P_\phi(-h) = \frac{g}{\rho_0} \int_0^{-h} \bar{\rho}(z) dz$$

where $P_\phi(-h)$ is the pressure at the base of the ice shelf, $\bar{\rho}$ is the reference density profile and ρ_0 is the Boussinesq density.

No buoyancy and momentum fluxes occur through the sea surface and ice shelf base.

2.3 Horizontal and vertical discretization

The numerical model is formulated on an Arakawa C-grid [Arakawa and Lamb, 1976] which belongs to the class of staggered grids. In a C grid, quantities such as η and ρ are at the center of the grid, while the east-west component of baroclinic and barotropic velocities are displaced half a grid to the west of the center and their north-south components are displaced half a grid to the south of the center.

As already mentioned and explicitly described for the model equations, as vertical discretization, the model uses a s -coordinate system which follows the bottom topography and the ice shelf base (Fig. 2.1). In the expression 2.3,

$$s = 0 \quad \text{at the upper boundary and,}$$

$$s = -1 \quad \text{at the bottom.}$$

This implies that the upper boundary is no longer at $z = 0$ but follows the ice shelf base at $z = -(h + \eta(\mathcal{X}, \mathcal{Y}, t))$.

This vertical coordinate system avoids the step-like representation of bottom topography which produces spurious effects associated with discontinuities [Haidvogel and Beckmann, 1999]. As a trade-off, the horizontal pressure gradient force has a systematic error which, however, can be reduced by subtraction of a reference density profile and is generally small for weak stratification and high horizontal resolution. When compared to the linear σ -transformation, the s -discretization has the advantage of increasing resolution near the surface and near the bottom

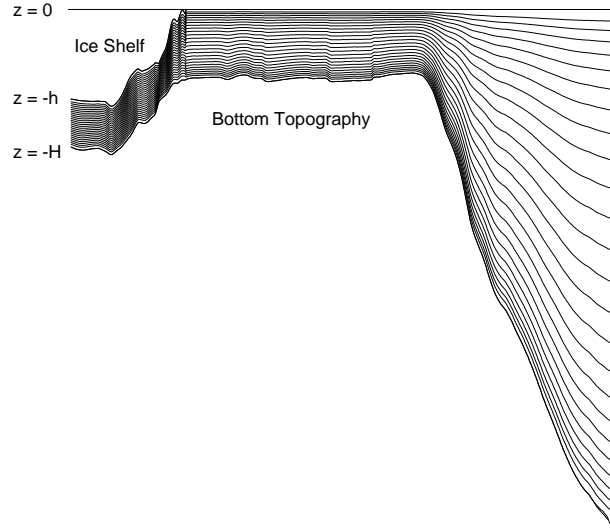


Figure 2.1: Scheme showing the vertical topography and ice shelf base-following discretization.

through the parameters θ_s and θ_b . Their ranges are $0 < \theta_s \leq 20$ and $0 < \theta_b \leq 1$, respectively. With a larger value of θ_s , more resolution is kept above a prescribed depth (usually the depth of the pycnocline, $Tcline$). For $\theta_b=0$, the vertical resolution near the surface increases with increasing θ_s . Resolution of the surface and bottom layers increases equally with increasing θ_s for $\theta_b=1$. In the three-dimensional model, these parameters were set to $\theta_s=3$, $\theta_b=1$ and $Tcline=200$.

Such stretching enables processes to be solved in both boundary layers with higher accuracy. This is particularly important for the investigation of the vertical structure of internal tidal currents, because near the seabed and the pycnocline, tidal current shear can be large.

Chapter 3

Barotropic Tides in the Weddell Sea

The barotropic tidal results presented in this chapter are obtained using the external mode (Eqs. 2.10-2.12) of the full three-dimensional model. The model is applied in the Weddell Sea sector and is used to investigate the elevation amplitude and barotropic currents of the two main semidiurnal (M_2 , S_2) and the two main diurnal (K_1 , O_1) tidal constituents. The main goal of this chapter is to investigate the tides in the Weddell Sea at their basic mode before starting the study of their interaction with stratification.

3.1 2D-Model (X-Y) Configuration

3.1.1 Model domain, grid resolution and bathymetry

The model domain covers the Weddell Sea sector from 56°S to 83°S and from 80.65°W to 12°E (Fig. 3.1). The horizontal grid will be hereafter referred as BRIOS4.3. It has an isotropic resolution of 0.25° in the zonal and $0.25^\circ\cos\phi$ in the meridional direction, resulting in a grid spacing of ≈ 17 km at the northern boundary and 3 km at the southern edge.

Bottom topography was taken from the $2'$ resolution data set of Smith and Sandwell [1997]. South of 72°S , this is supplemented by data from the AWI bathymetry group [Schenke *et al.*, 1998]. For computational reasons, the minimum water column thickness was set to 100 m. Six ice shelves are represented in the model (Fig. 3.2): George VI (GE), Larsen (A), Filchner-Ronne (FRIS), Brunt (B), Riiser-Larsen (C) and Fimbul (F), where the third is included with as much detail as possible [Johnson and Smith, 1997]. Due to the lack of detailed bathymetric and ice thickness data, all the others are represented in a cruder way assuming a thickness of 200 m for ice and water column. The water column thickness is shown in Fig. 1.1. Seven islands

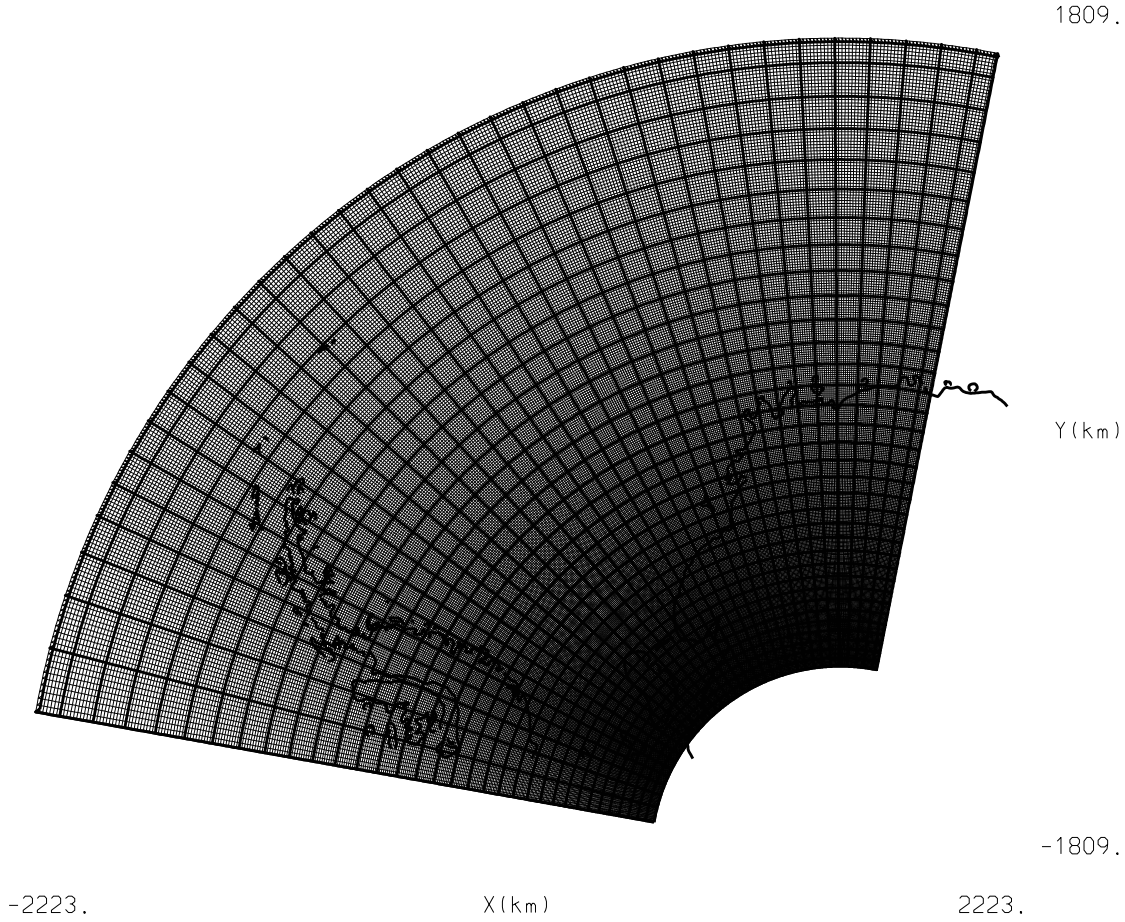


Figure 3.1: Weddell Sea grid (BRIOS4.3).

are represented in the model domain (Fig. 3.2): Alexander (AI), Adelaide (AD), King George (KG), South Orkney (SO), South Sandwich Island complex (SI), Berkner (BI) and Henry-Korff Ice Rise complex (HK).

3.1.2 Subgrid-scale parameterization and treatment of the ice shelves

In the 2D-model, dissipation occurs through horizontal viscosity and stress at the ocean bottom and at the ice shelf base. The bottom stress is taken as a nonlinear function of the depth-averaged velocity according to the quadratic bottom drag law:

$$[\tau_{bx}, \tau_{by}] = \mathcal{C}_D [\bar{u}, \bar{v}] \sqrt{\bar{u}^2 + \bar{v}^2}$$

and \mathcal{C}_D is the drag coefficient. Its value was chosen as 0.0025. In barotropic tidal models, this is a classical value [e.g., Flather, 1980; Kantha, 1995; Fanjul *et al.*, 1997]. \mathcal{C}_D is 0.005 in ice shelf areas to account for the additional drag at the ice-water interface [MacAyeal, 1984a].

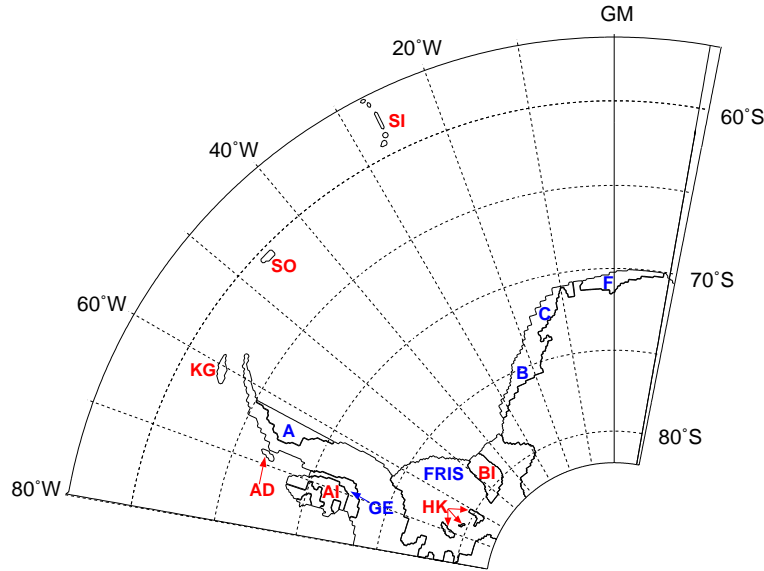


Figure 3.2: Ice shelves and islands of the Weddell Sea sector as represented by BRIOS4.3 grid. Ice shelves included are (blue letters): George VI (GE), Larsen (A), Filchner-Ronne (FRIS), Brunt (B), Riiser-Larsen (C) and Fimbul (F). Islands (red letters): Alexander (AI), Adelaide (AD), King George (KG), South Orkney (SO), South Sandwich (SI), Berkner (BI) and the Henry and Korff Ice Rises (HK).

The lateral viscosity was set to $1000 \text{ m}^2 \text{ s}^{-1}$. Several tests made with the model varying its value demonstrated that this parameter has little influence on the model results.

3.1.3 Time step, time integration and harmonic analysis

The 2D-model is advanced in time using a trapezoidal-leapfrog time-stepping scheme. According to the Courant-Friedrichs-Lewy condition, the time step was set to 20 s.

The model integration begins in January 1, 1992. This date was chosen only because this is the time zero for the TPXO.5 software. Since tides are periodic and all model results are harmonically analyzed, producing time-independent results, the starting data is not fundamental for tides investigations as it is for forecast studies. Starting from a state of rest, the model was integrated for 60 days. The last 30 days of model results (vertically averaged horizontal velocities and free surface elevation) were harmonically analyzed using the algorithms developed by Foreman [1977; 1978]. In a numerical model, such relatively short span of data can be used for tidal analysis [Foreman and Henry, 1989], because no fluctuations in the data exist due to other effects, e.g., meteorological forcing. These can produce a significant part of the "noise" in observed time series and thus, require a full synodic period of data (the minimum length of data necessary to separate a pair of constituents according to Rayleigh criterion) for an accurate analysis.

3.2 Dataset Available for Comparison

There are two kinds of observational data that can be used to validate the model results: elevation and velocity measurements. In this section, the dataset available for comparison with model results is presented, mainly to show that tidal measurements in the Weddell Sea are sparse and cannot be considered representative for a statistical analysis. Details about the observational data, as record observed depth, position, etc., will be given along the following chapters when the data is used for comparison.

3.2.1 Free surface elevation measurements

A tide gauge measures and records fluctuations in hydrostatic pressure due to changes in the water level at regular time intervals. Thus, the recorded data consist of elevation time series which are harmonic analyzed to obtain amplitude and phase of several tide constituents. All the tide gauge data used for comparison with model results were obtained from published papers (Fig. 3.3, red triangles). Most of them are located at coastal stations on islands or at the coast of the Antarctic Continent. At the southern shelf break, only two measurements are available. At the western side of the Weddell Sea, there are no observations.

Because of the ice barrier, tide gauges cannot be employed to measure the hydrostatic pressure beneath FRIS. For this reason, indirect measurements are made using tiltmeters and gravimeters. The first instrument measures the tilting of the ice shelf, while the second, converts

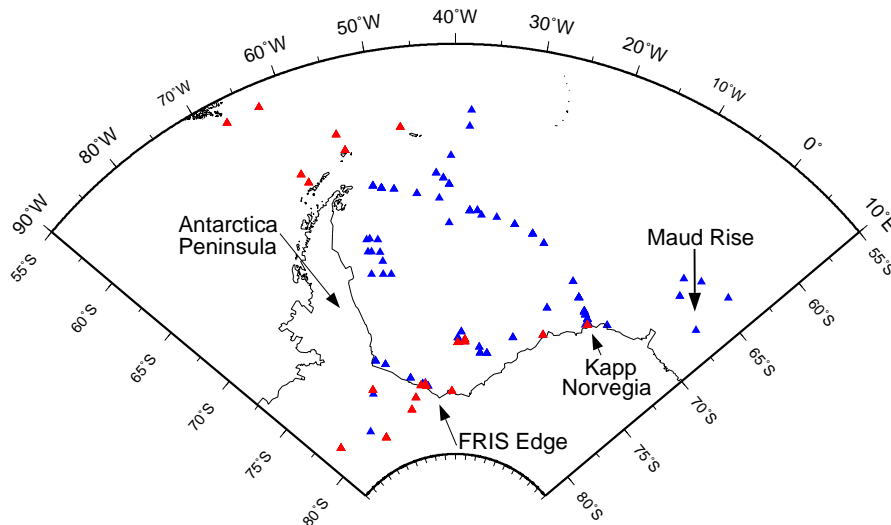


Figure 3.3: Spatial distribution of current meters (blue triangles) and tide gauges (red triangles) observations in the Weddell Sea.

variations in gravity to tidal displacements [Thiel *et al.*, 1960]. There are eight tidal amplitude and phase measurements made at FRIS; three of them are located near the ice shelf edge (some positions are so close to each other that they overlap on the map).

3.2.2 Velocity measurements

Tidal currents are obtained after harmonic analysis of time series of recorded velocities. These are recorded using current meters deployed in moorings. When velocity data is collected beneath FRIS, current meters are deployed through the ice shelf.

Most current meters are located in deep ocean (Fig. 3.3, blue triangles), especially in a transect between the top of the Antarctica Peninsula and Kapp Norvegia. Also around Maud Rise ($\approx 65^\circ\text{S}$, 0°E), velocity data from five instruments can be used for model validation. At the southern shelf break of the Weddell Sea, eight measurements are available. Such as for elevation, there are no velocity data collected at the southwestern Weddell Sea shelf break. In front of Larsen ice shelf, tidal velocity data from several current meters is available. Beneath FRIS, only two velocity measurements are available and four for its edge.

As will be shown in this and next chapters, tidal currents have a high variability in time and space. For an accurate statistical analysis, a more homogeneous and higher spatial distribution of tidal observations would be necessary. For this reason, along the presentation of model results, observed data will be compared directly with model results.

3.3 Barotropic Tides at Diurnal Frequencies: K_1 and O_1

3.3.1 Diurnal elevation amplitudes and Greenwich phases

We begin investigating diurnal period tides. Both main diurnal frequencies, K_1 and O_1 , present similar characteristics. They have maximum amplitudes beneath FRIS, reaching approximately 50 cm (K_1) and 36 cm (O_1), and at the shelf break where both reach up to 60 cm (Fig. 3.4).

As already investigated by Middleton *et al.* [1982; 1987], at diurnal frequencies continental shelf waves develop at the Weddell Sea shelf break which are visible in Fig. 3.4 through the higher and lower circular modulations found especially at the southern shelf break (they were found also at the west side of the Antarctica Peninsula). Although these waves have not been documented along the Ronne ice front, Rignot *et al.* [2000] suggested their existence in this

area as well. Using radar images and interferometry techniques, they found a bump-and-dimple feature along the ice front which was explained based in these shelf waves. In the model results (Fig. 3.4), there is a modulation near the Ronne ice front that can support Rignot *et al.*'s [2000] hypothesis.

Continental shelf waves

Shelf waves of predominantly K_1 and O_1 tidal frequencies were first observed in current meter records from the shelf region of the outer Hebrides off western Scotland [Cartwright, 1969]. Since then, continental shelf waves are commonly observed features of coastal oceanic regions.

Thomson and Crawford [1982] gave a detailed explanation for the generation mechanism and propagation of these waves and the following discussion is based in his work. Shelf waves occur in response to the along-shore component of the bottom Reynolds stress associated with the tidally induced time-independent boundary layer. They are necessarily of subinertial frequencies and that is the reason why they only develop at diurnal frequencies in the latitude range of the Weddell Sea.

Contrary to Kelvin waves which are little affected by detailed bathymetry of the continental margin due to their large scales, continental shelf waves are strongly dependent of the shelf-slope topography. The forcing mechanism for their generation is limited to sections of a coast having sufficiently broad shelves or steep slopes. But their quantitative characteristics (as wavelength and wavenumber) are dependent of the along-slope topographic variations. This

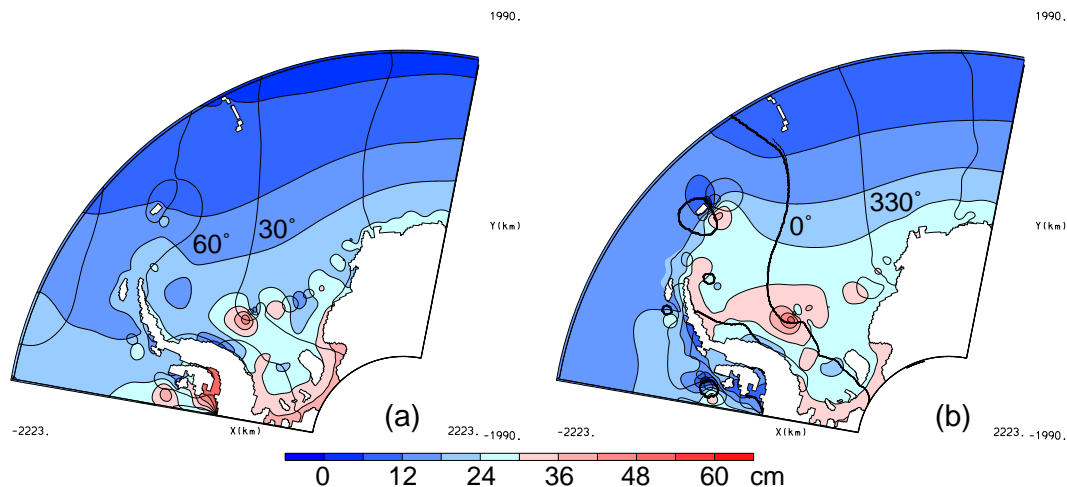


Figure 3.4: Tidal amplitudes (cm) and Greenwich phases (degrees) for tidal frequencies K_1 (a) and O_1 (b) obtained with the grid 4.3.

is exemplified comparing Fig. 3.4a and Fig. 3.5. In the last figure, a grid with 6 times less resolution (1.5° in the zonal, $1.5^\circ \cos\phi$ in the meridional direction) was used to simulate the diurnal tides. In this case, continental shelf waves appear as a single circular modulation in the center of the Weddell Sea.

Middleton *et al.* [1987] and Foldvik *et al.* [1990] estimated the wavelength of the continental shelf waves using a dispersion diagram and current meter data from the southeastern Weddell Sea shelf break, respectively. Using the dispersion diagram, the K_1 wavelength was found to be between 300 and 200 Km. Foldvik *et al.* [1990] found that at K_1 and O_1 periods, these waves have between 334 and 226 km and 275 and 181 km length, respectively. At approximately the same positions of Foldvik *et al.* [1990] observations, the modeled wavelengths were 420 (K_1) and 376 km (O_1) that are around 100 km longer than the observed values. These results indicate that a finer grid resolution would be necessary to represent quantitatively the continental shelf waves in the model domain.

Most of the tide gauge data available for model comparison were collected at coastal stations or at places where topography changes abruptly as near the continental shelf break and near FRIS edge (Fig. 3.3). As can be seen in Table 3.1, all these regions are not appropriate for model comparison because modeled and observed depths tend to have a large discrepancy. This results in a relatively poor correlation between modeled amplitudes and observations (Fig. 3.6). The worst correlation is found with the data collected at FRIS, a region where the difference between modeled and observed water column thickness can be large. The correlation between Greenwich tidal phases are similar to that of diurnal tidal amplitudes and for this reason are not shown. It would be helpful to compute the error associated with each of the measurements

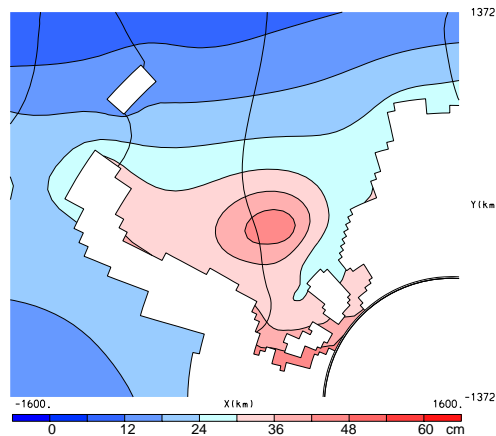


Figure 3.5: K_1 tidal amplitudes (cm) obtained using a grid with 6 times coarser resolution than grid4.3.

Table 3.1: Positions and observed depths of tide gauge data used for comparison with model results

| Lat | Lon | Depth _{obs} (m) | Depth _{mod} (m) | Reference |
|---------|---------|--------------------------|--------------------------|--------------------------------|
| 59°08'S | 37°58'W | 2870 | 551 | Foldvik <i>et al.</i> [1985d] |
| 74°26'S | 39°24'W | 475 | 412 | Foldvik <i>et al.</i> [1990] |
| 77°16'S | 49°00'W | 260 | 251 | Foldvik <i>et al.</i> [1990] |
| 56°32'S | 67°00'W | 500 | 792 | Smithson <i>et al.</i> [1996] |
| 56°29'S | 62°59'W | 3925 | 3969 | Smithson <i>et al.</i> [1996] |
| 61°28'S | 61°17'W | 3946 | 3209 | Smithson <i>et al.</i> [1996] |
| 62°08'S | 60°41'W | 500 | 724 | Smithson <i>et al.</i> [1996] |
| 59°44'S | 55°30'W | 3690 | 3590 | Smithson <i>et al.</i> [1996] |
| 60°51'S | 54°43'W | 1020 | 1094 | Smithson <i>et al.</i> [1996] |
| 71°03'S | 11°45'W | 430 | 575 | Smithson <i>et al.</i> [1996] |
| 60°03'S | 47°05'W | 2010 | 2347 | Smithson <i>et al.</i> [1996] |
| 72°53'S | 19°37'W | 461 | 620 | Smithson <i>et al.</i> [1996] |
| 74°23'S | 37°39'W | 470 | 507 | Middleton <i>et al.</i> [1982] |
| 74°26'S | 39°24'W | 450 | 412 | Foldvik <i>et al.</i> [1985d] |
| 77°07'S | 49°03'W | 260 | 266 | Smithson <i>et al.</i> [1996] |
| 76°45'S | 64°30'W | NaN | 343 | Doake [1992] |
| 77°43'S | 41°08'W | 792 | 854 | Thiel <i>et al.</i> [1960] |
| 77°08'S | 50°30'W | NaN | 175 | Smithson <i>et al.</i> [1996] |
| 77°53'S | 52°45'W | NaN | 174 | Smithson <i>et al.</i> [1996] |
| 78°37'S | 55°08'W | NaN | 370 | Smithson <i>et al.</i> [1996] |
| 79°44'S | 67°21'W | NaN | 335 | Smithson <i>et al.</i> [1996] |
| 76°57'S | 49°04'W | 270 | 266 | Foldvik <i>et al.</i> [2001] |

and to plot it together with the graphics above discussed. Unfortunately, the available data for model comparison consist of amplitudes and phases of the main tidal constituents, and not, the raw time series data. Many of these data are older than 15 years (Table 3.1) and it is not possible to find the majority of them nowadays.

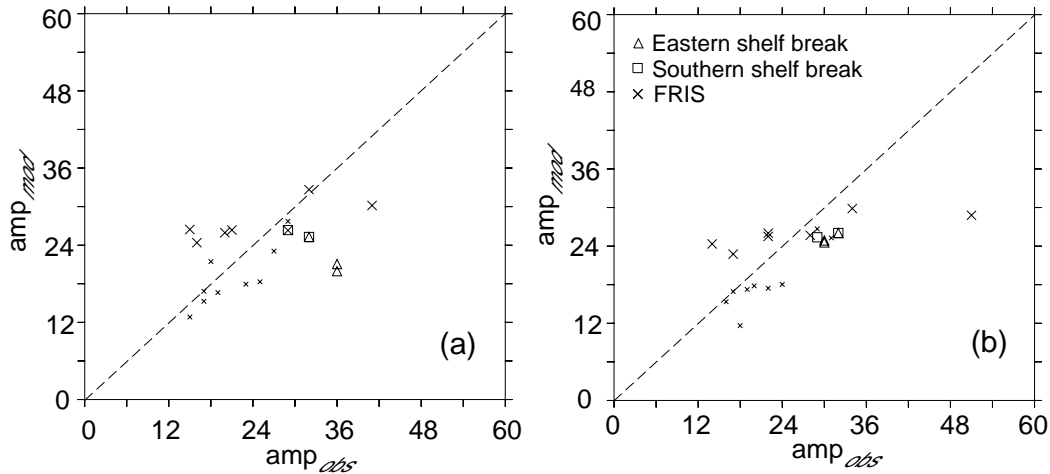


Figure 3.6: Correlation between modeled and observed K_1 (a) and O_1 (b) amplitudes (cm) for the Weddell Sea. The dashed line indicates perfect agreement between model results and observations. Below (above) the dashed line, modeled amplitudes are underestimated (overestimated). Each symbol indicates a region listed in (b). For other areas, the symbol small "x" is used.

3.3.2 Diurnal barotropic currents

Maxima diurnal barotropic currents are found in regions with strong topographic gradient as the shelf break and ice shelf edges (Fig. 3.7). At the southern Weddell Sea shelf break, observations [Foldvik *et al.*, 1990] and modeling confirm that diurnal tidal currents are stronger than the semidiurnal (compare Fig. 3.7b with Fig. 3.13b). The strongest diurnal currents are found at General Belgrano Bank (see Fig. 1.1 for reference) reaching 30 cm s^{-1} . Beneath FRIS, diurnal velocities are not increased as that at located at the shelf break. K_1 tidal ellipses rotate counterclockwise at the shelf break, continental shelf and beneath Ronne ice shelf near its edge. In deep ocean and in the southern portion of the FRIS cavity, they rotate clockwise. O_1

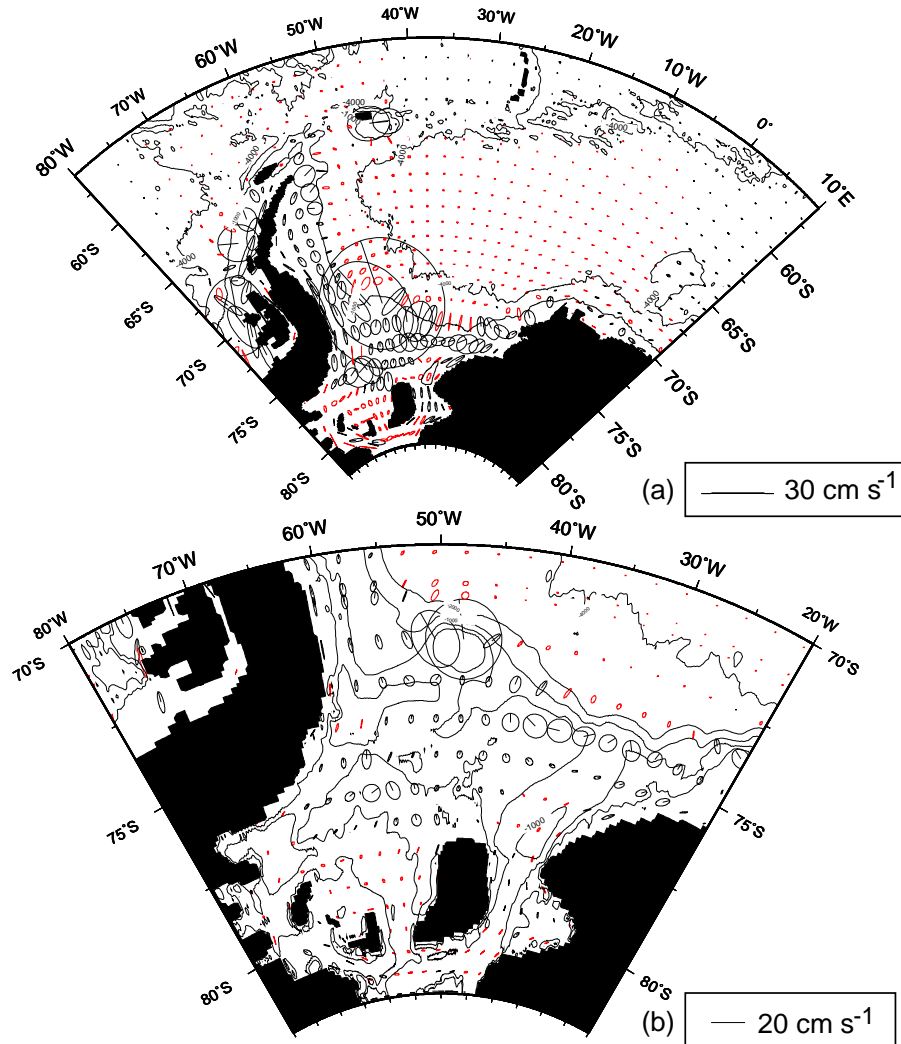


Figure 3.7: K_1 barotropic tidal ellipses for the all Weddell Sea (a) and a zoom on the continental shelf and FRIS area (b). Black (red) ellipses indicate counterclockwise (clockwise) rotation and the line from the center gives the direction of the current vector at the time of maximum tidal potential (Greenwich phase). Fig. a and b have different color scales.

barotropic currents (not shown) had roughly the same characteristics as that at K_1 frequency.

In general, the model tends to overestimate diurnal tidal currents, especially at the southern Weddell Sea continental shelf break (squares in Fig. 3.8). As discussed in the subsection before, in that region the continental shelf waves propagate along the slope. Since the model resolution is not fine enough to represent them accurately, a poor correlation is found between model results and observations. The best agreement occurs with current meter data from deep ocean (small crosses in Fig. 3.8) where tidal currents are not strongly affected by small scale topographic features and where modeled and observed depths are not so different. In Appendix A, a table containing details about the data used in this analysis is presented. The raw data were not available, only the processed data.

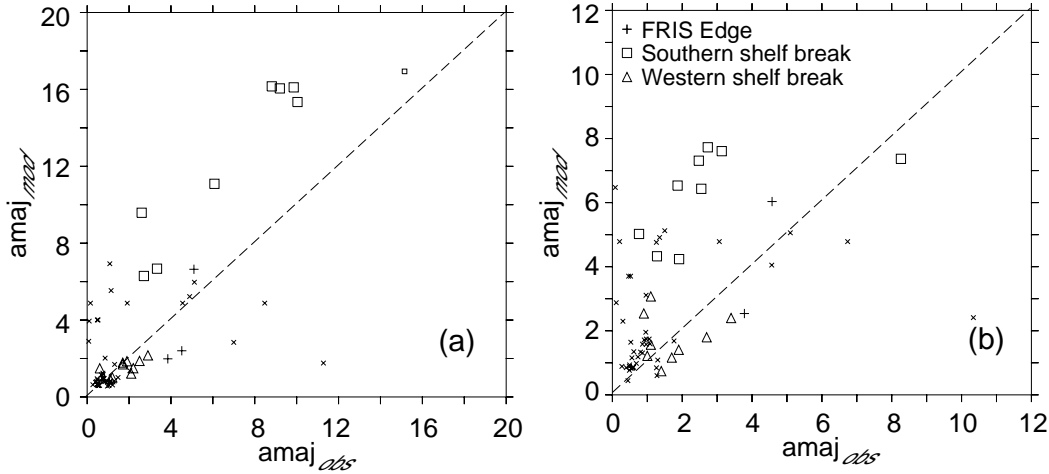


Figure 3.8: Correlation between modeled and observed K_1 (a) and O_1 (b) major axis (cm s^{-1}) for the Weddell Sea. The dashed line indicates perfect agreement between model results and observations. Below (above) the dashed line, modeled amplitudes are underestimated (overestimated). Each symbol indicates a region listed in (b). For other areas, the symbol small "x" is used.

3.3.3 Diurnal tidal energy flux

Propagation of the barotropic tide may be examined from consideration of depth-integrated energy-fluxes associated with each tidal constituent. These fluxes are determined from the harmonic analysis, through [Bowden, 1983]

$$E_u = \frac{1}{2} \rho g h A_{tc} u_{tc} \cos(\phi_{u_{tc}} - \phi_{amp_{tc}}) \quad (3.1)$$

$$E_v = \frac{1}{2} \rho g h A_{tc} v_{tc} \cos(\phi_{v_{tc}} - \phi_{amp_{tc}}) \quad (3.2)$$

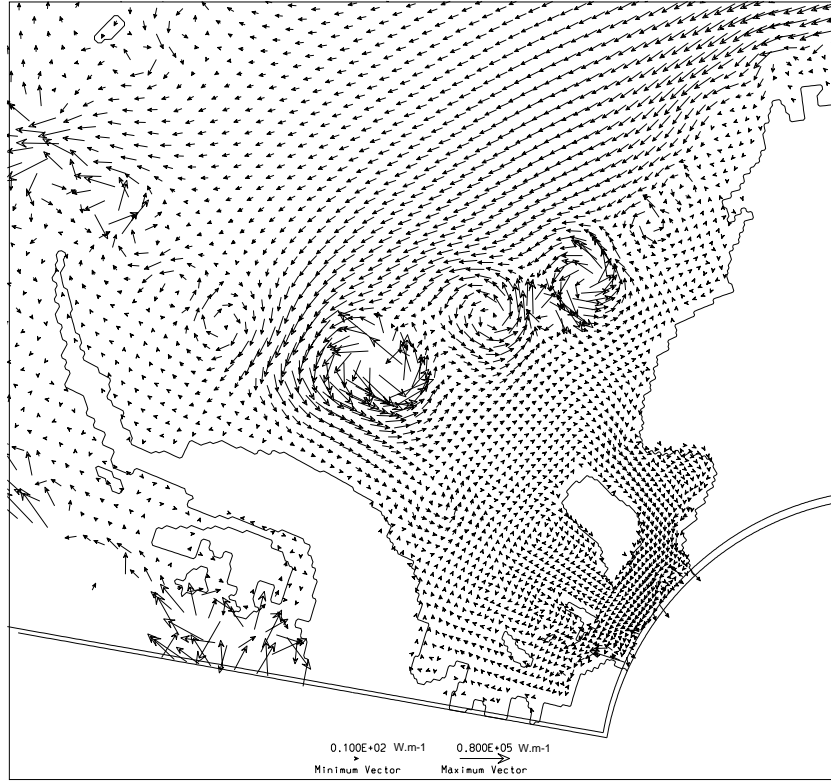


Figure 3.9: O_1 tidal energy flux (W m^{-1}) along the inner Weddell Sea.

where ρ is a reference potential density, h is depth, A_{tc} and $\phi_{amp_{tc}}$ are the amplitude and phase of the free surface elevation for a tidal constituent, u_{tc} and v_{tc} are the magnitude of the tidal velocity in the zonal and in the meridional direction, respectively, and $\phi_{u_{tc}}$ and $\phi_{v_{tc}}$ their respective phases.

The general trend of the energy of diurnal tides is to propagate westward, although a complex structure of eddies along the shelf break of the inner Weddell Sea is found. These are related to the modulations caused by the continental shelf waves. The strongest of these gyres is located at the General Belgrano Bank. Relative little diurnal energy enters the FRIS cavity but enough to form a weak clockwise flux.

3.4 Barotropic Tides at Semi-diurnal Frequencies: M_2 and S_2

3.4.1 Semidiurnal elevation amplitudes and Greenwich phases

Both M_2 and S_2 surface barotropic tides have the highest amplitudes near the coast in the FRIS cavity. They reach 1.6 m and 1.0 m at the southwestern corner of Ronne Ice Shelf for M_2 and

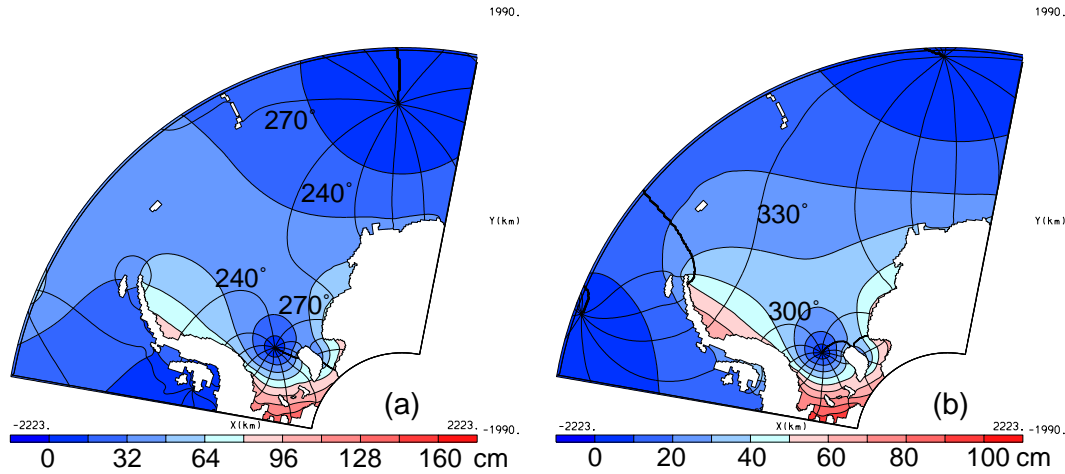


Figure 3.10: Tidal amplitudes (cm) and Greenwich phases (degrees) for tidal frequencies M_2 (a) and S_2 (b) obtained with the grid 4.3. Fig. a and b have different color scales.

for S_2 , respectively (Fig. 3.10). There is an amphidromic point located near the FRIS edge with the wave rotating clockwise for both semidiurnal frequencies.

In Fig. 3.11, the amplitude of the surface tide for M_2 and S_2 are plotted against tide gauge observations from the FRIS edge Doake [1992]. Due to the amphidromic point, semidiurnal tidal elevation is minimum near the ice shelf front. For both M_2 and S_2 frequencies, modeled tidal amplitudes fit the observed data for this region.

The modeled semidiurnal barotropic amplitudes show a good correlation with the observed elevations (Fig. 3.12). The data used for comparison is the same described in Table 3.1. For M_2 (Fig. 3.12a), most of the data that have poor correlation is located at FRIS. In this region due to the lack of accurate bottom topography and ice shelf thickness, the model has a less accurate solution than in open water, as discussed for the correlation at diurnal frequencies. In other

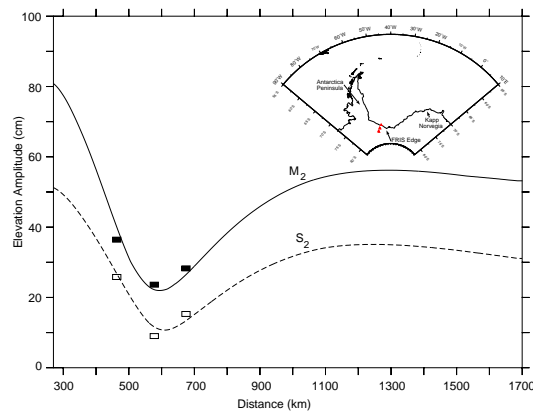


Figure 3.11: Comparison between modeled M_2 (solid line) and S_2 (dashed line) amplitudes and observations (M_2 , black rectangles and S_2 , white rectangles) through a section in the model domain. Tide gauge positions used for this comparison are indicated in the inset.

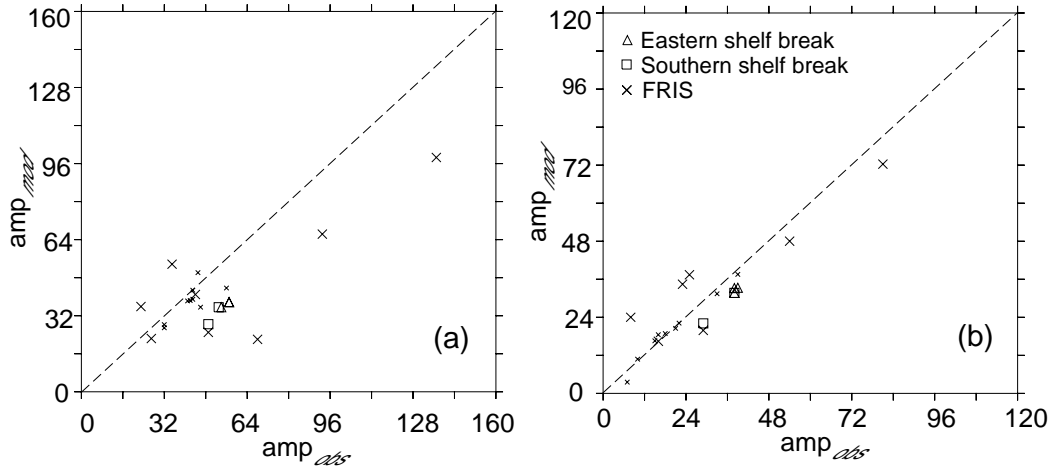


Figure 3.12: Correlation between modeled and observed M_2 (a) and S_2 (b) amplitudes (cm) for the Weddell Sea. The dashed line indicates perfect agreement between model results and observations. Below (above) the dashed line, modeled amplitudes are underestimated (overestimated). Each symbol indicates a region listed in (b). For other areas, the symbol small "x" is used.

points where poor correlation is found, the main reason is due to differences between the observed and modeled depth (see Table 3.1). S_2 modeled tidal amplitudes show good agreement with observations. The same explanations described for the poor correlation in some points for the M_2 frequency apply to S_2 tidal elevations. The correlation between Greenwich tidal phases are similar to that of semidiurnal tidal amplitudes and for this reason are not shown.¹

3.4.2 Semidiurnal barotropic currents

Barotropic tidal ellipses for M_2 are shown in Fig. 3.13a plotted every thirtieth (twentieth) grid point in the east-west (north-south) direction. A zoom in the southern Weddell Sea and FRIS cavity is shown Fig. 3.13b. In the deep ocean, tidal currents are weak (≈ 1 to 2 cm s^{-1}) and only in shallower areas ellipses have a significant magnitude. On the shelf, typical barotropic tidal currents are 10 cm s^{-1} reaching the highest values in the FRIS cavity close to its edge ($\approx 30 \text{ cm s}^{-1}$). At the shelf break and on the continental shelf, tidal ellipses have a circular pattern indicating strong currents in both along and cross-slope directions. Near the coast, they become more elongated and parallel to it. The major axis of the tidal ellipses has a normal orientation to

¹Comparing the results presented in this chapter with those from previous numerical modeling works in the same region [Robertson *et al.*, 1998; Makinson and Nicholls, 1999] which do not considered \tilde{f} -terms, the inclusion of the horizontal component of the Coriolis term did not produce significant differences. As demonstrated by Beckmann and Diebels [1994], the effects of \tilde{f} is hardly detectable in the barotropic mode of motion because the characteristic velocity introduced by this additional term in the propagation of a long surface wave (as tides) is

$$c_{\tilde{f}} = \frac{1}{2} \tilde{f} h. \quad (3.3)$$

Thus, in deep ocean $c_{\tilde{f}}$ is only 0.1 m s^{-1} while surface wave speed is about 200 m s^{-1} .

the southeastern shelf break and the FRIS edge (Fig. 3.13b). In the central Weddell Sea and at shallow areas, as at the shelf break and continental shelf, tidal ellipses rotate counterclockwise. In most of the FRIS cavity, ellipses rotate clockwise.

Similar characteristics of the tidal ellipses are found for S_2 , but their magnitudes are reduced by a factor of 2 to 2.5 compared to M_2 . This characteristic is valid worldwide, except in regions where continental boundaries and bottom topography modify it; e.g., at George VI Ice Shelf the M_2 signal is damped, thus surface elevation is higher and tidal currents are stronger for S_2 than that at M_2 frequency [Potter *et al.*, 1985]. The M_2 constituent represents the rotation of the Earth with respect to the Moon and S_2 the rotation of the Earth with respect to the

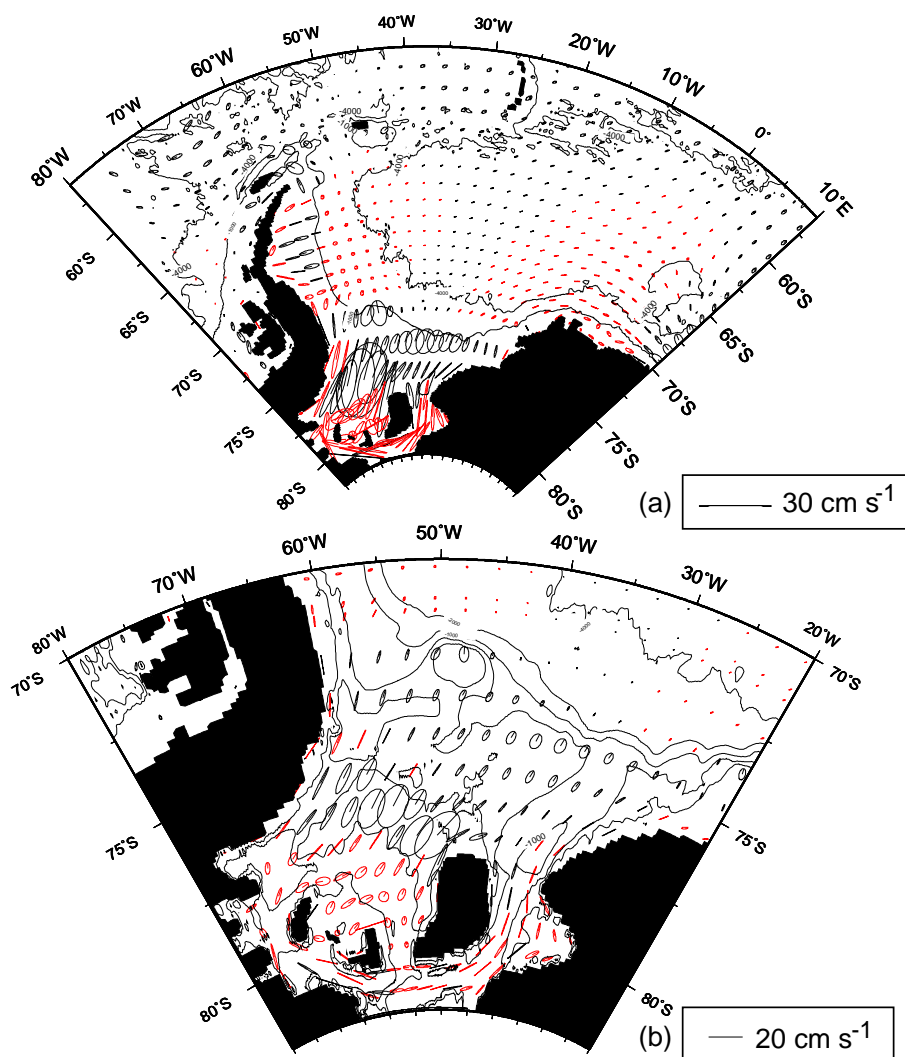


Figure 3.13: M_2 barotropic tidal ellipses for the all Weddell Sea (a) and a zoom on the southern shelf break and FRIS area (b). Black (red) ellipses indicate counterclockwise (clockwise) rotation and the line from the center gives the direction of the current vector at the time of maximum tidal potential (Greenwich phase). Ellipses are plotted every thirtieth (twentieth) grid point in the east-west (north-south) direction. Fig. a and b have different color scales.

Sun. Following Newton's law of gravitational attraction, although the Moon is much smaller than the Sun, it is, nevertheless, more important for the tidal potential due to its proximity to the Earth (the tide-generating force of the Sun is only $\approx 46\%$ of that from the Moon) [Pugh, 1987].

As it was made for semidiurnal tidal amplitudes, Fig. 3.14 shows the correlation between modeled and observed semidiurnal major axis of the tidal ellipse. Compared to tidal elevations, tidal currents have higher variability. They are much more affected by small scale topographic features than the surface tidal wave. For this reason, it is expected that observations and modeled data are not very well correlated. Along the western shelf break (defined as the shelf break parallel to the eastern coast of the Antarctica Peninsula), modeled semidiurnal tidal currents are underestimated, while in the southern shelf break and at the FRIS edge, they are overestimated. Although the phase of the tidal ellipse (not shown) had the same kind of correlation as found for the major axis, a better agreement was found for the minor axis and the ellipse inclination which have a smaller variability than the phase and the major axis.

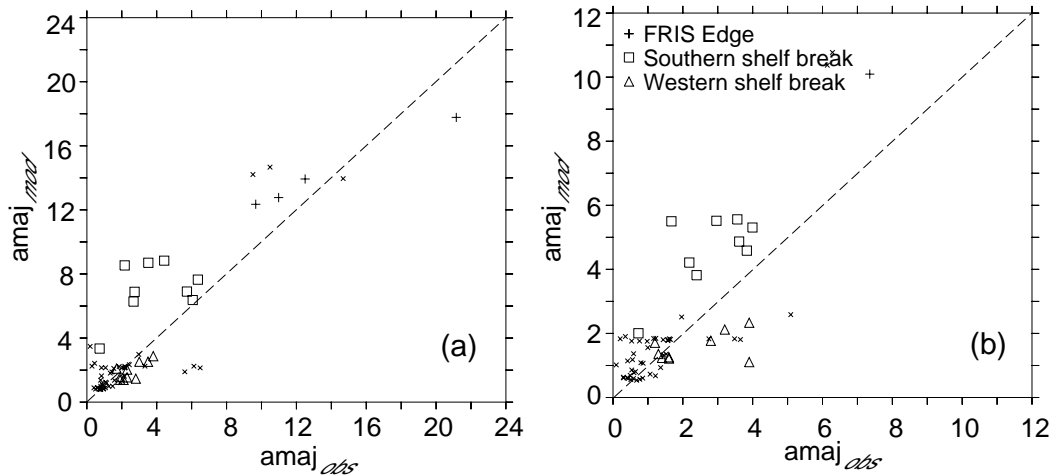


Figure 3.14: Correlation between modeled and observed M_2 (a) and S_2 (b) major axis (cm s^{-1}) for the Weddell Sea. The dashed line indicates perfect agreement between model results and observations. Below (above) the dashed line, modeled amplitudes are underestimated (overestimated). Each symbol indicates a region listed in (b). For other areas, the symbol small "x" is used.

3.4.3 Semidiurnal tidal energy flux

In the inner Weddell Sea, both M_2 (Fig. 3.15) and S_2 (not shown) frequencies propagate as a Kelvin wave with the energy flux vectors parallel to the coast. The biggest part of the semidiurnal tidal energy enters the FRIS cavity, propagating in clockwise sense. The energy flux vectors

follow the Antarctic coast with high cross-slope component occurring almost perpendicularly on the eastern and western sides of the southern continental shelf break (Fig. 3.15). Looking in a smaller spatial scale, at these places at the shelf break where the tidal wave reaches it almost in a normal angle, the tidal wave can be assumed to propagate as a Poincaré wave. This idea will be important in the next chapter.

Another important aspect of this analysis is related to areas where internal tide generation can occur. As will be explained in the next chapter, the barotropic mode is the forcing term generating an internal tide. For areas at the continental shelf break and slope where cross-shelf energy flux normal to the shelf break exist [Weigand *et al.*, 1969], maximum barotropic tidal forcing for internal tide generation is expected. In these regions, the cross-slope component (or the major-axis) of the barotropic M_2 tidal ellipses (Fig. 3.13) is largest, and stratified fluid is forced most vigorously up and down the continental slope.

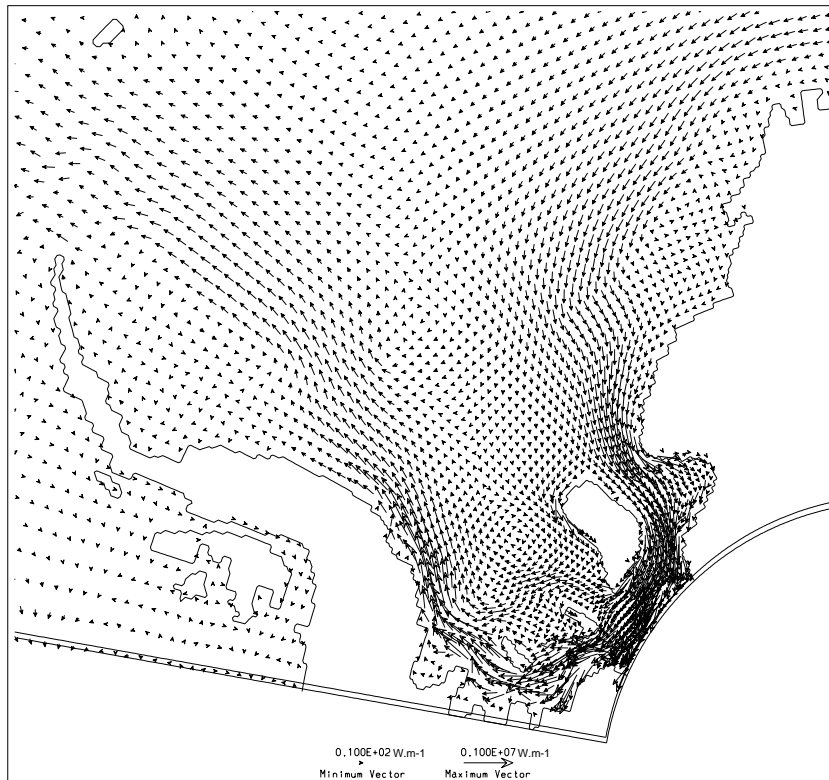


Figure 3.15: M_2 tidal energy flux (W m^{-1}) along the inner Weddell Sea.

3.5 Barotropic Residual Currents

Residual circulation is produced by tidal oscillation advecting positive and negative vorticity, generated by tidal flow over topographic features (as a shelf break), in opposite directions [Robinson, 1981]. This induced time-independent flow is directed along isobaths with the shallower water at the left side in the case of the southern hemisphere.

Residual currents are weak in the deep ocean where typical values are of the order of few millimeters per second (Fig. 3.16). Only at the shelf break, they assume a considerable magnitude, especially in the western Weddell Sea. Maximum residual flow in this area reaches 1 m s^{-1} at General Belgrano Bank due to the significant diurnal amplification and steep topographic gradients. Along the shelf break of the eastern side of the Antarctica Peninsula, strong residual currents flow northward, while at the shelf break at its western side, a complex pattern is found. Besides continental shelf waves which also developed in this area and thus, generating time-independent currents, imperfect radiation condition at the western boundary of the model domain may also contribute to increase the residual flow nearby.

Tidal currents flowing across the step change in water column thickness present at the ice shelf edge will generate a residual flow along the barrier with the ice shelf on the left with currents reaching 5 cm s^{-1} (Fig. 3.17). Beneath FRIS, maximum residual currents are found near

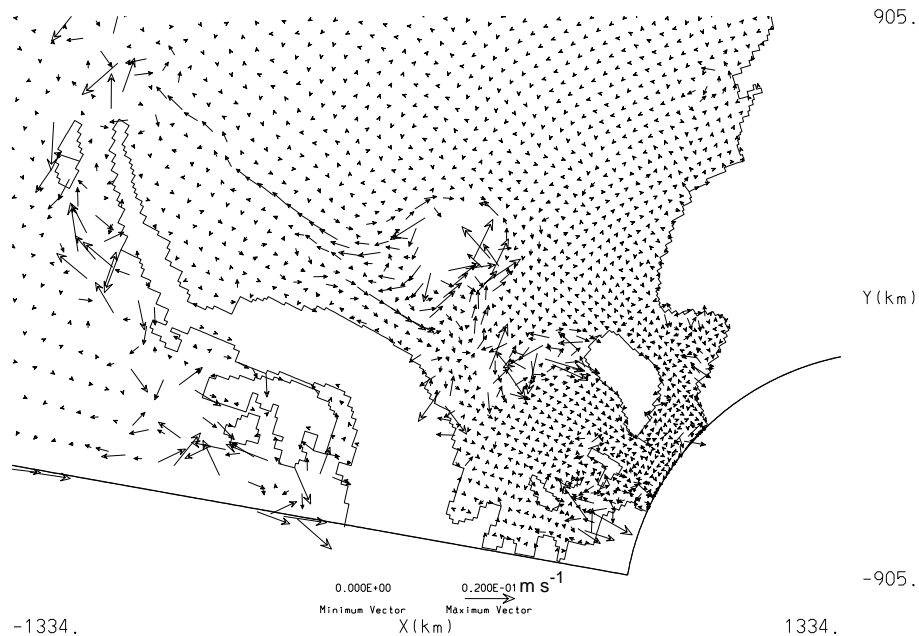


Figure 3.16: Barotropic residual currents (m s^{-1}) in the Weddell Sea. Vectors greater than 0.2 m s^{-1} are not plotted.

the ice shelf front where residual currents follow the contours of the complex local bathymetry. As modeled by Makinson and Nicholls [1999], there is a counterclockwise residual flow around Berkner Island. But the modeled barotropic residual currents are about 50% weaker than those obtained by Makinson and Nicholls [1999].

The strength of the mean flow depends on the horizontal and vertical length scales of topography, and the magnitude of the tidal current. For this reason, there are indications that, if the grid spacing underestimates the topographic gradients or the tidal excursion ($E = V_{tidal} * \omega_{tidal}$, V_{tidal} is the tidal current and ω_{tidal} the tidal period) is small compared with the grid size, residual currents will be underestimated [Robinson, 1981]. An estimate of the maximum residual flow at a sharp topographic step such as occurs at the shelf break and ice shelf front, is given by [Robinson, 1981]:

$$R_{max} = 0.15 \times 10^{-4} E \left(\frac{\Delta h}{h} \right) \quad (3.4)$$

where $\Delta h/h$ is the depth change ratio of the topographic feature. Following Makinson and Nicholls [1999], at the Ronne Ice Shelf edge, tidal excursion is about 8 km perpendicular to the ice front with a step gradient of 200 m. Thus, a residual velocity of approximately 8



Figure 3.17: Barotropic residual currents (m s^{-1}) beneath FRIS.

cm s^{-1} will be induced. In this region, grid resolution is about 7 km in both east-west and north-south directions, practically the same value of the tidal excursion. It indicates that the model resolution is not fine enough to fully represent barotropic tidal residuals. Makinson and Nicholls [1999] had to increase their grid resolution from 15 to 35 nodes per degree of latitude and from 4 to 8 nodes per degree of longitude in order to improve the estimation of residual currents in the FRIS region.

3.6 Summary

Diurnal and semidiurnal tides have been modeled using a barotropic model applied to the Weddell Sea. Comparison with observations shows reasonable agreement, given that the bottom topography is important and not well known especially in regions as the FRIS cavity and the western inner Weddell Sea.

The most interesting aspect related to diurnal tides in the Weddell Sea is the development of continental shelf waves. These produce the strongest barotropic currents along the Weddell Sea shelf break. Beneath FRIS, K_1 and O_1 produce currents of few centimeters per second ($\approx 5 \text{ cm s}^{-1}$), although at the Ronne Ice Shelf front they can reach 14 cm s^{-1} . While semidiurnal barotropic tides are only weakly dependent on the grid resolution, diurnal tides show a strong dependence. This requires the use of fine grids in both zonal and meridional directions to have an accurate representation of them.

The characteristics of the simulated semidiurnal amplitude, phase, and barotropic tidal currents can be explained in terms of Kelvin wave dynamics. Such wave has highest amplitudes near the coast with an exponential offshore decay [LeBlond and Mysak, 1978]. Furthermore, their current ellipses and energy flux vectors are aligned parallel to the coast. A crude estimate of the distance between Kapp Norvegia and the tip of the Antarctic Peninsula following the coast, is 3000 km. Assuming an average depth of 400 m, the M_2 and S_2 wavelengths are 2800 km and 2706 km, respectively. Therefore, similar to the Ross Sea [MacAyeal, 1984a], only one wave can be supported inside the Weddell Sea, and the amphidromic point is caused by the phase difference of the wave at each opposite side of the inner Weddell Sea. Their strongest currents are found in shallow areas as the continental shelf and beneath FRIS.

Similarly to the representation of the continental shelf waves along the shelf break, the magnitude of the residual currents is also strongly dependent on the grid resolution. Although

general characteristics and direction of propagation of the modeled residual flow agree with previous numerical results for the Weddell Sea and FRIS [Makinson and Nicholls, 1999], its magnitude is underestimated about 30% because tidal excursion is small compared to the grid size.

Chapter 4

Baroclinic Tides in the Weddell Sea

In this chapter, baroclinic tidal currents and the resulting residual currents in the inner Weddell Sea and beneath Filchner-Ronne Ice Shelf will be examined, as well as their seasonal variability caused by different stratification. Only the M_2 and S_2 semidiurnal frequencies will be considered. The 3D-model configuration will be described, beginning with an y-z pilot study regarding grid resolution. A brief description of the stratification field of the inner Weddell Sea, based on water mass characteristics, will be presented. Model results will be compared to the linear internal wave theory and the critical latitude effect will be introduced. The simulated baroclinic residual currents will also be examined.

4.1 Linear Internal Wave Theory and Critical Latitude Singularity

Model validation and interpretation of the results will use the linear internal wave theory, which is outlined here briefly.

Laboratory experiments [e.g. Baines and Xin-Hua, 1985] and theoretical models [e.g., Prinsenbergh and Rattray, 1974] indicate that near an internal wave generation site (e.g., shelf break), internal tide energy is confined to beams propagating along characteristics in the cross-isobath direction. These beams can be represented by the general theory of rays and ray tracing techniques [LeBlond and Mysak, 1978], which are the basis used by the linear internal wave theory [Baines, 1973; 1974].

In a continuously stratified medium, the energy associated with a plane internal wave travels at an angle with the horizontal determined by the radian wave frequency ω , the inertial frequency f , and the buoyancy frequency N . The slope c of the energy flux or group velocity

(the wave characteristic), derived from the dispersion relation for linear inertial-internal waves, can be expressed as [Gill, 1982]

$$c^2 = \tan \theta = \frac{(\omega^2 - f^2)}{(N^2 - \omega^2)}$$

where θ is the angle the group velocity has with the horizontal. As stratification decreases, the angle of the group velocity with respect to the horizontal increases. The ratio γ introduced by Baines [1973] is the critical parameter determining the existence and propagation of internal tides:

$$\gamma = \frac{h_y}{c}$$

where h_y is the slope of the seabed in the cross-slope direction.

Internal wave energy incident upon bathymetry that is steeper than the wave characteristic (i.e., supercritical slope: $\gamma > 1$) will reflect back toward deeper water and little energy will propagate onshore. Waves which are incident on subcritical bathymetry ($\gamma < 1$) will be focused into shallower water, but some energy can still propagate offshore. Few, if any, internal waves will be generated. Internal wave generation is strongest where the bottom slope is critical ($\gamma = 1$) for the given frequency. In this situation, the plane of the forcing motion, dictated by the bottom slope, and the plane of the particle motion for the free internal wave coincide. When this form of resonance exists, even very weak barotropic tidal currents can generate strong internal tides which then propagate along-slope.

In order to achieve these results, the linear internal wave theory neglects friction, viscosity, and the non-linear terms, and assumes N to be constant throughout the water column. Furthermore, the observation that the continental shelf break and slope could often be considered as slowly varying in the along-slope direction, led to the reduction of the internal tidal problem to two dimensions (y-z). This simplification implies that rotation does not change the character of the motion, limiting the applicability of the linear theory to Poincaré waves. Despite these simplifications, the linear internal wave generation theory is able to explain some observations [e.g., Holloway, 1985] and certain laboratory experiments [e.g., Baines and Xin-Hua, 1985], especially for $\gamma \rightarrow 1$.

The theory is valid if the forcing frequency ω is superinertial and below the buoyancy

frequency N . Within this frequency band, the oscillations may propagate away from the generation site as plane internal waves. If $\omega < f$, free internal wave propagation is not possible. As a result, any generated internal wave motion is trapped locally (c is imaginary). This is the case for diurnal frequencies at the latitude range of the inner Weddell Sea (see Table 4.1).

Table 4.1: Critical Latitudes in Each Hemisphere for the Four Major Tidal Constituents

| Tidal Constituent | Critical Latitude (N/S) |
|-------------------|-------------------------|
| S_2 | $85^\circ 45' 54''$ |
| M_2 | $74^\circ 28' 18''$ |
| K_1 | $30^\circ 00' 00''$ |
| O_1 | $27^\circ 36' 47''$ |

For a propagating Poincaré wave at the *critical latitude* ($\omega = f$) the rays are turned back equatorward [Middleton and Denniss, 1993] and there is no internal wave propagation poleward. For Kelvin waves, this singularity at the critical latitude does not exist, and they can occur for frequencies on both sides of the local inertial frequency as well as at the inertial frequency itself [LeBlond and Mysak, 1978].

The inclusion of the horizontal component of the Coriolis term (\tilde{f}) can change the spectrum range where free wave propagation is possible ($f < \omega < N$), with free waves propagating also, e.g., at subinertial frequencies ($f > \omega$). But visible effects caused by \tilde{f} affecting this spectrum can only be expected for sufficiently weak stratification [Beckmann and Diebels, 1994] (see also Appendix B) or for a homogeneous ocean (see Appendix E).

In Table 4.1, the critical latitude of the four major tidal constituents is listed. Near the critical latitude, both theoretical and empirical studies [Prinsenbergh and Bennett, 1989; Nøst, 1994; Furevik and Foldvik, 1996] of the tidal profile reveal an increasing benthic boundary layer thickness. Foldvik *et al.* [1990] described semi-diurnal currents at the southern Weddell Sea continental shelf break, and observed that the M_2 tidal currents are strongly dependent on depth near its critical latitude ($74^\circ 28' 18''$).

In analogy with Ekman's theory for wind-driven currents, two rotary boundary layer thicknesses can be defined for a constant eddy viscosity ν_0 [Davies, 1985]:

$$\Delta_+ = \pi \sqrt{\frac{2\nu_0}{|f + \omega|}} \quad \Delta_- = \pi \sqrt{\frac{2\nu_0}{|f - \omega|}}.$$

The thickness of the bottom boundary layer is defined as the distance at which the velocity

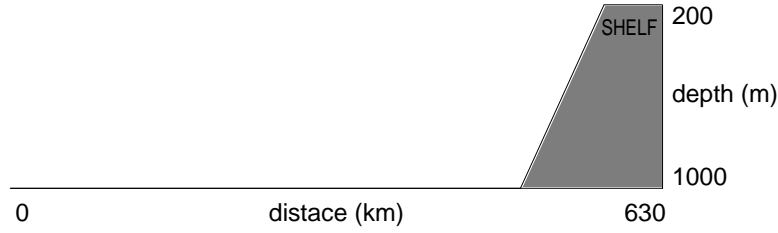


Figure 4.1: Idealized shelf-slope topography used in the 2D-pilot study.

magnitude is reduced by e^{-1} . In the southern hemisphere ($f < 0$), the counterclockwise component (Δ_+) goes to infinity when the Coriolis frequency approaches the frequency of the tidal constituent, explaining the increased thickness of the benthic layer and the depth-dependence of currents observed near critical latitudes. The boundary layer thickness of the clockwise component (Δ_-) is limited to the distance where bottom friction still produces shear in the water column.

4.2 X-Z Pilot Study of the Grid Resolution

Craig [1987] developed an analytical model to study the generation of internal tides through the interaction of barotropic tides with linear topography, applied to an idealized shelf edge (see Fig. 4.1). The model considers an incompressible, inviscid, stably stratified fluid. The motion is assumed hydrostatic, without along-slope variation. Frictional, nonlinear and rotational effects are not included. The aim of this set of experiments is to simulate the generation of internal tides with the numerical tidal model. A range of horizontal and vertical resolutions is used to determine the grid spacing necessary to obtain similar results as presented by Craig [1987]. The tidal model was configured as close as possible to its analytical counterpart. The linear form of the hydrodynamic equations with Coriolis and all diffusion (momentum and density) terms set to zero were solved.

The idealized shelf edge consists of a continental shelf of 50 km width and 200 m depth; a shelf slope with water depths increasing to 1000 m over a distance of 80 km, with a 1000 m deep ocean extending 500 km further offshore (Fig. 4.1). The model domain is periodic in the along-slope direction. The onshore (offshore) boundary (right (left) in Fig. 4.1) is closed (open). Assuming this domain and model configuration, the model is bidimensional: all gradients are zero in the along-slope direction. The model is forced at the offshore boundary with a barotropic tidal wave of 1 m amplitude and a $1.40518 \times 10^{-4} \text{ s}^{-1}$ frequency of which

corresponds to the M_2 tidal constituent.

Craig [1987] based his analysis in the linear internal wave theory, varying the slope from supercritical ($\gamma=1.1$) to subcritical ($\gamma=0.9$). His two figures which will be used for comparison with the results of the BRIOS tidal model are shown in Fig. 4.2.

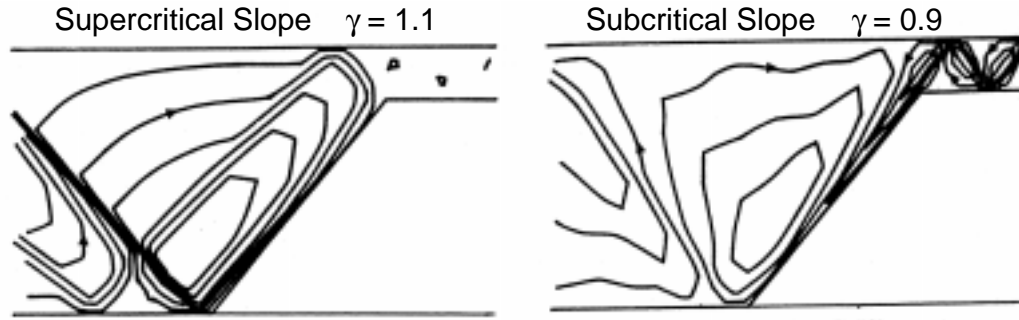


Figure 4.2: Contours of overturning stream function (streamline interval is $0.5 \text{ m}^2 \text{ s}^{-1}$) obtained by Craig [1987]. Supercritical and subcritical slopes are indicated in the figure.

4.2.1 The vertical grid spacing

Linear stratification identical to that of Craig [1987] ($N^2=2.39 \times 10^{-4} \text{ s}^{-2}$ for $\gamma=1.1$ and $N^2=1.60 \times 10^{-4} \text{ s}^{-2}$ for $\gamma=0.9$), was used. For the first series of experiments, the horizontal grid spacing was set to 625 m.

With 50 s-levels, non-equidistantly distributed over the water column (Fig. 4.3, top), the numerical results obtained were comparable to the analytical solutions presented by Craig [1987]. There is a small phase difference between plotted analytical and modeled results, but the main characteristics of the internal tide are visible. For $\gamma=0.9$ (Fig. 4.3, top right side), the internal tide is generated at the base of the slope and energy propagates on- and off-shore. On the shelf, a first mode internal tide is found. For $\gamma=1.1$ (Fig. 4.3, top left side), the internal tide is generated and reflected at the base of the slope to the deep ocean, propagating along a ray path. Although most of the energy propagates offshore, some still propagates onshore resulting in a second mode internal tide on the shelf. As in the analytical results, the major stream function values are within the rays. Considering 25 s-levels (Fig. 4.3, center), all the major characteristics of the internal tide (magnitude and propagation path) are still represented for both supercritical and subcritical slopes. A grid resolution of 12 s-levels yields reasonably accurate solutions, especially on the shelf, but on deep ocean, the stream function starts to show

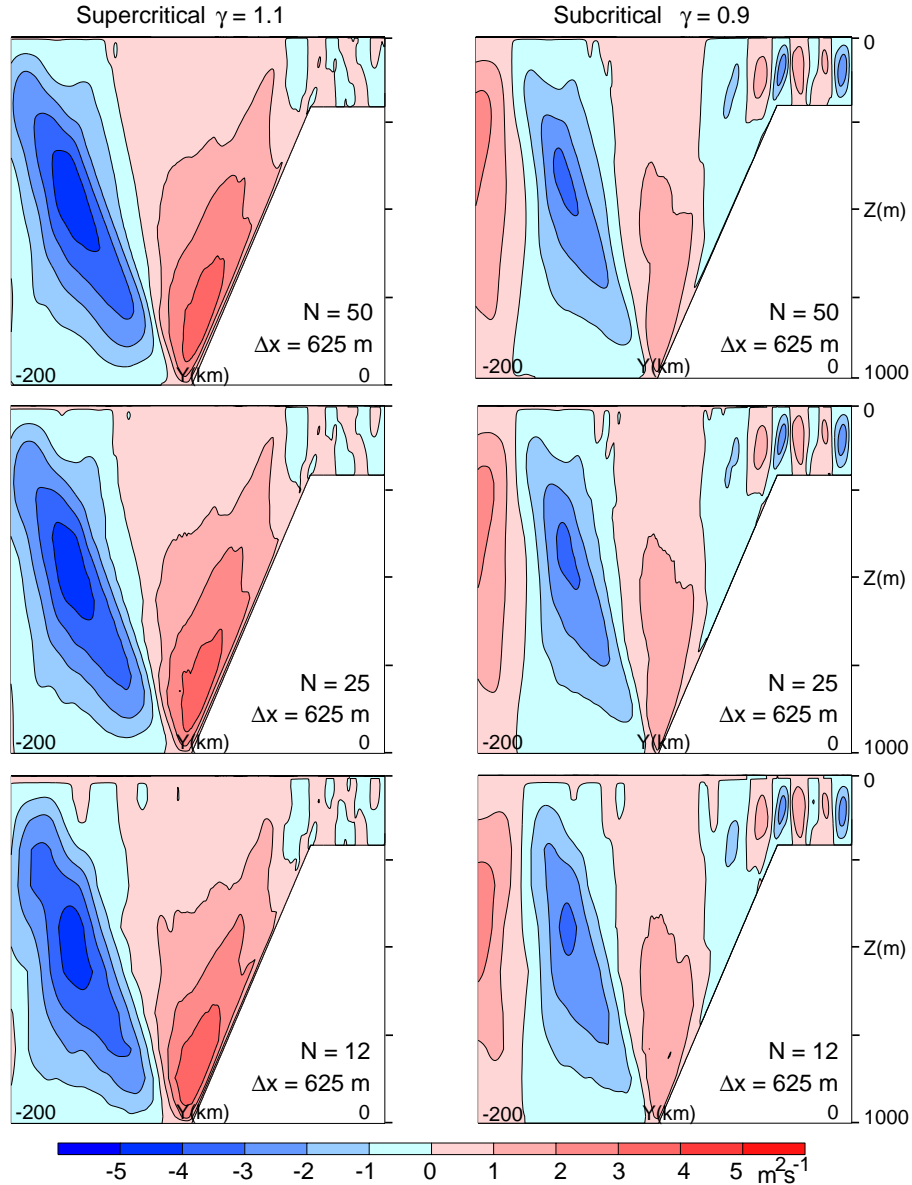


Figure 4.3: Investigation of the vertical grid resolution. Overturning stream function ($\text{m}^2 \text{s}^{-1}$) computed after 46 hours of integration and considering a horizontal grid spacing of 625 m. Supercritical and subcritical slopes are indicated in the figure, as well the number of vertical s-levels employed (N) for each simulation.

some differences compared to the analytical results, especially for $\gamma=1.1$. These results suggest that 25 s-levels are enough to represent quantitatively and qualitatively an internal tide with this numerical model.

4.2.2 The horizontal grid spacing

Such fine resolution (625 m) would require large computational resources. Furthermore, this resolution is ≈ 4.8 times higher than the topographic data set available for the Weddell Sea. To verify if a horizontal grid spacing coarser than 625 m could be used, four additional cases

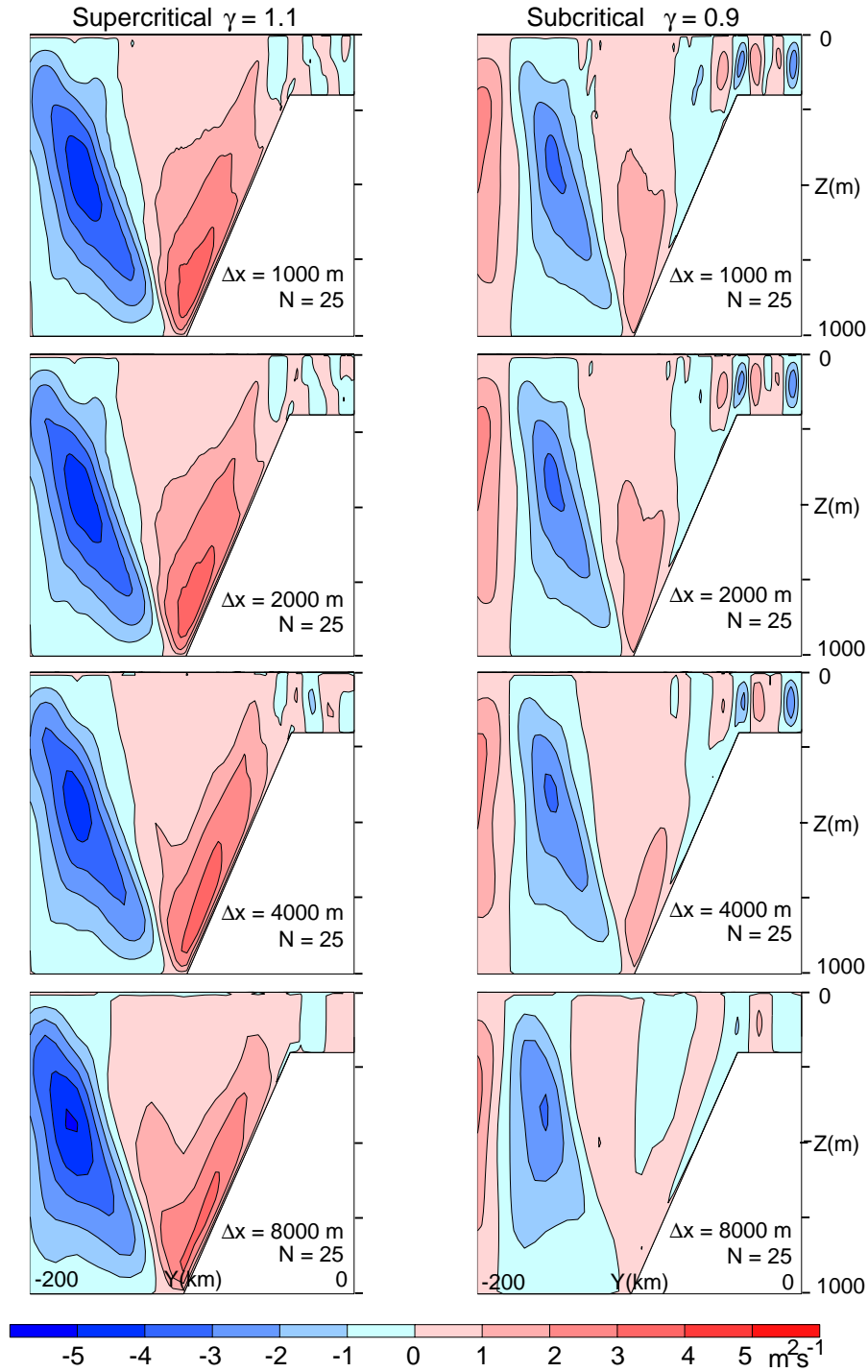


Figure 4.4: Investigation of the horizontal grid resolution. Overturning stream function ($\text{m}^2 \text{s}^{-1}$) computed after 46 hours of integration and considering 25 s-levels, non-equidistantly distributed over the water column. Supercritical and subcritical slopes are indicated in the figure, as well the horizontal grid spacing employed (Δx) for each simulation.

were tested, with grid spacing ranging from 1000 m to 8000 m. In all simulations, 25 vertical s-levels, non-equidistantly distributed over the water column were used.

Fig. 4.4 shows that for a horizontal resolution of 2000 m, the main features of the internal

tide are still present. For increasing grid spacing, the numerical solution deviates further from the analytical solution for both super- and subcritical slopes; especially on the shelf, the magnitude and vertical structure of the internal tide are different compared to solutions computed with finer grid spacing. Based on these results, a horizontal grid spacing of 2000 m in the cross-slope direction was considered to be sufficient to represent Craig's results.

The above set of experiments validates the model with respect to the analytical solution by Craig. The parameters of that configurations, however, are not representative of the Weddell Sea. Therefore, four other semi-idealized experiments were made varying the horizontal grid resolution and considering slope ($h_x \approx 1.45 \times 10^{-2}$) and buoyancy frequency ($N^2 = 2 \times 10^{-6}$, see also Section 4.4) closer to those conditions found in the southern Weddell Sea. Stratification and slope are linear; maximum and minimum depth are 4500 m and 800 m, respectively. Horizontal viscosity ($1000 \text{ m}^2 \text{ s}^{-1}$) and quadratic bottom friction ($C_D = 0.0025$) are included, as well as rotational effects ($f = -1.4 \times 10^{-4} \text{ s}^{-1}$).

Again, the same dependence on resolution was found as before. There is a clear difference

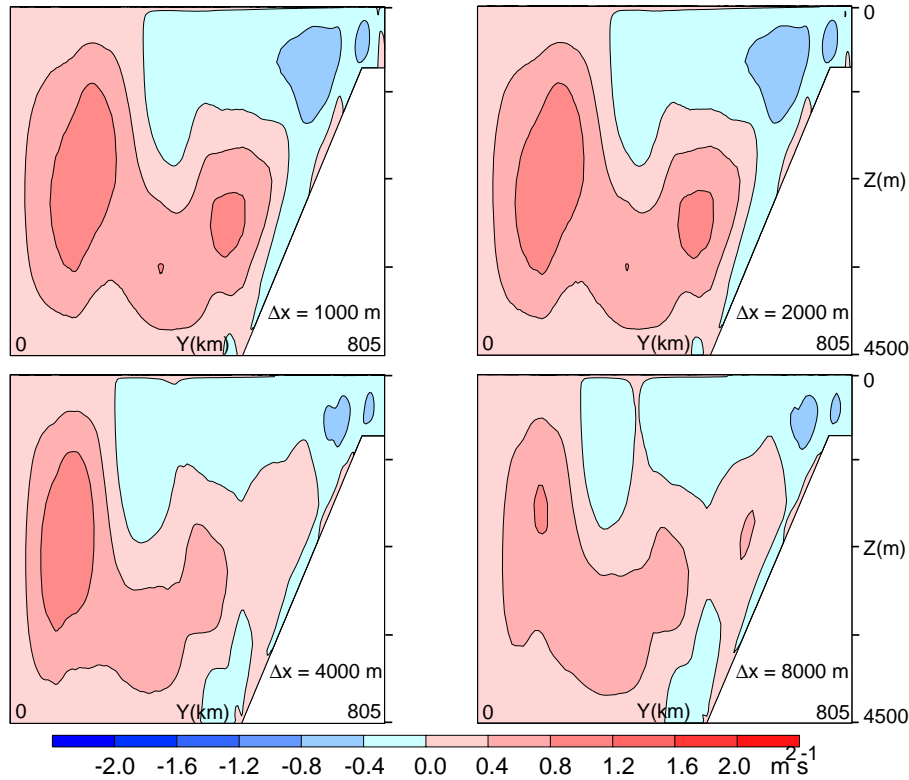


Figure 4.5: Investigation of the horizontal grid resolution considering typical slope and buoyancy frequency of the southern Weddell Sea. Overturning stream function ($\text{m}^2 \text{ s}^{-1}$) computed after 24 hours of integration and considering 25 s-levels, non-equidistantly distributed over the water column .

between solutions computed using 1 or 2 km (Fig. 4.5 upper) to those with 4 or 8 km grid spacing (Fig. 4.5 lower). Similarly to the previous idealized study, using 4 and 8 km resolution the model fails to represent the main features of the internal motion while the numerical solution has converged at 2 km.

Finally, the results presented in this Section suggest that a grid resolution of approximately 2 km is enough to have an accurate representation of internal tides with the BRIOS tidal model.

4.3 3D-Model Configuration

4.3.1 Model domain, grid resolution and bathymetry

Based on the results from the previous pilot-study, the three-dimensional grid was set up for internal tide investigations. Since this study is concerned with the influence of the slope topography on the vertical structure of tidal currents, and internal tide generation and propagation, it is desired to employ a grid as fine as computationally acceptable in the *cross-shelf* direction.

The orthogonal curvilinear grid covers the entire inner Weddell Sea, from the tip of the Antarctic Peninsula to Kapp Novergia (Fig. 4.6). It has 28 grid points in east-west direction and 800 grid points in north-south direction; due to computational restrictions, it was not possible to use a fine grid in both directions. For this reason, the focus of this study is on the southern Weddell Sea, the most probable region for internal wave generation, because the barotropic tidal wave encounters the continental shelf break almost perpendicular (see Subsection 3.4.3). Although along-slope topographic variations may generate internal waves as well, it is expected that these contribute less than the cross-slope variations (see Subsection 4.5).

The highest grid resolution in \mathcal{Y} direction (mostly north-south) is 2 km on the southern shelf and shelf break, increasing to 8 km near the northern boundary. In the east-west direction, the maximum and minimum resolutions are 10 km beneath the Ronne Ice Shelf and 120 km in the western Weddell Sea near the Antarctic Peninsula.

An increase of the number of vertical levels from the standard 25 s-levels (Fig. 2.1) showed no significant changes in the model results providing the grid was refined near the ocean floor and surface layer. The nonlinear stretching leads to a vertical grid spacing near the upper and lower boundaries of 6 m on the shelf and 28 m in deep ocean.

Bottom topography and ice shelf thicknesses were taken from the same data sets described

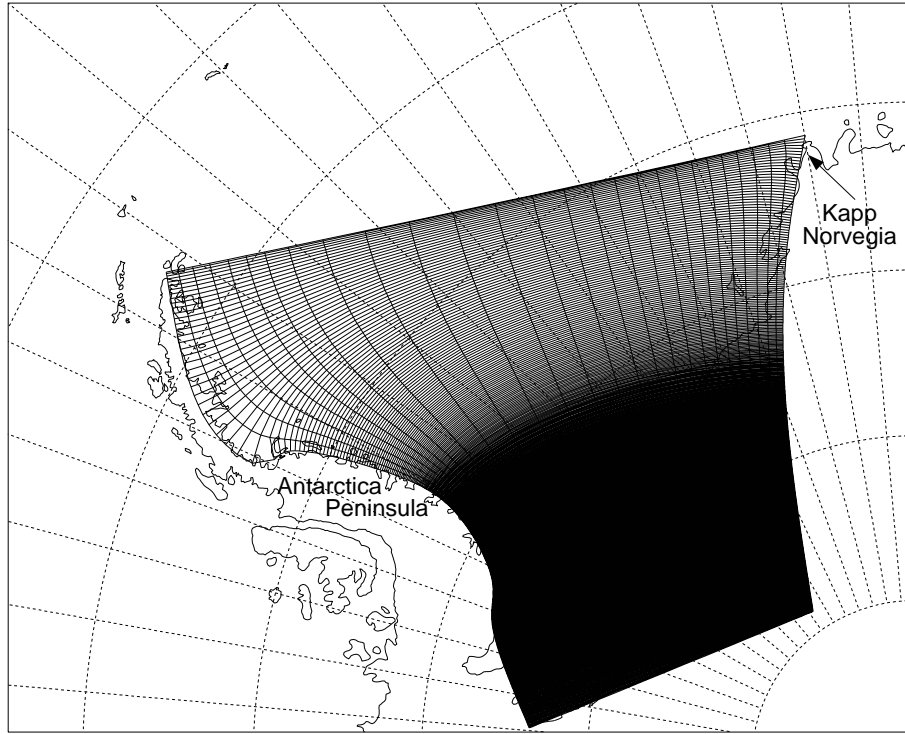


Figure 4.6: Inner Weddell Sea grid (BRIOS4.4).

in Subsection 3.1.1 and are shown in Fig. 4.7. For computational reasons, the minimum water column thickness was set to 200 m. Four ice shelves are represented in the model (Fig. 4.7): Larsen (A), Filchner-Ronne (FRIS), Brunt (B) and Riiser-Larsen (C); and two islands: Berkner (BI) and Henry-Korff Ice Rise complex (HK). In the next Sections, this grid will be referred as BRIOS4.4.

In the following investigations, only the major semidiurnal M_2 and S_2 tidal constituents will be included in the model forcing. To resolve accurately all four frequencies, as in the study of the barotropic tides (Chapter 3), a fine grid in both east-west and north-south directions would be necessary because of the dependence of the diurnal continental shelf waves on the along-slope grid resolution (see Subsection 3.3.1).

4.3.2 Subgrid-scale parameterization

A two-equation turbulence closure model, the level 2.5 scheme of Mellor and Yamada [1982], with modification by Galperin *et al.* [1988], is used to compute vertical viscosity (AKv) and diffusivity (AKd) coefficients. This parameterization (hereafter MY2.5) was used by many other tidal modeling studies (Holloway [1996], Xing and Davies [1998], Han [2000] among

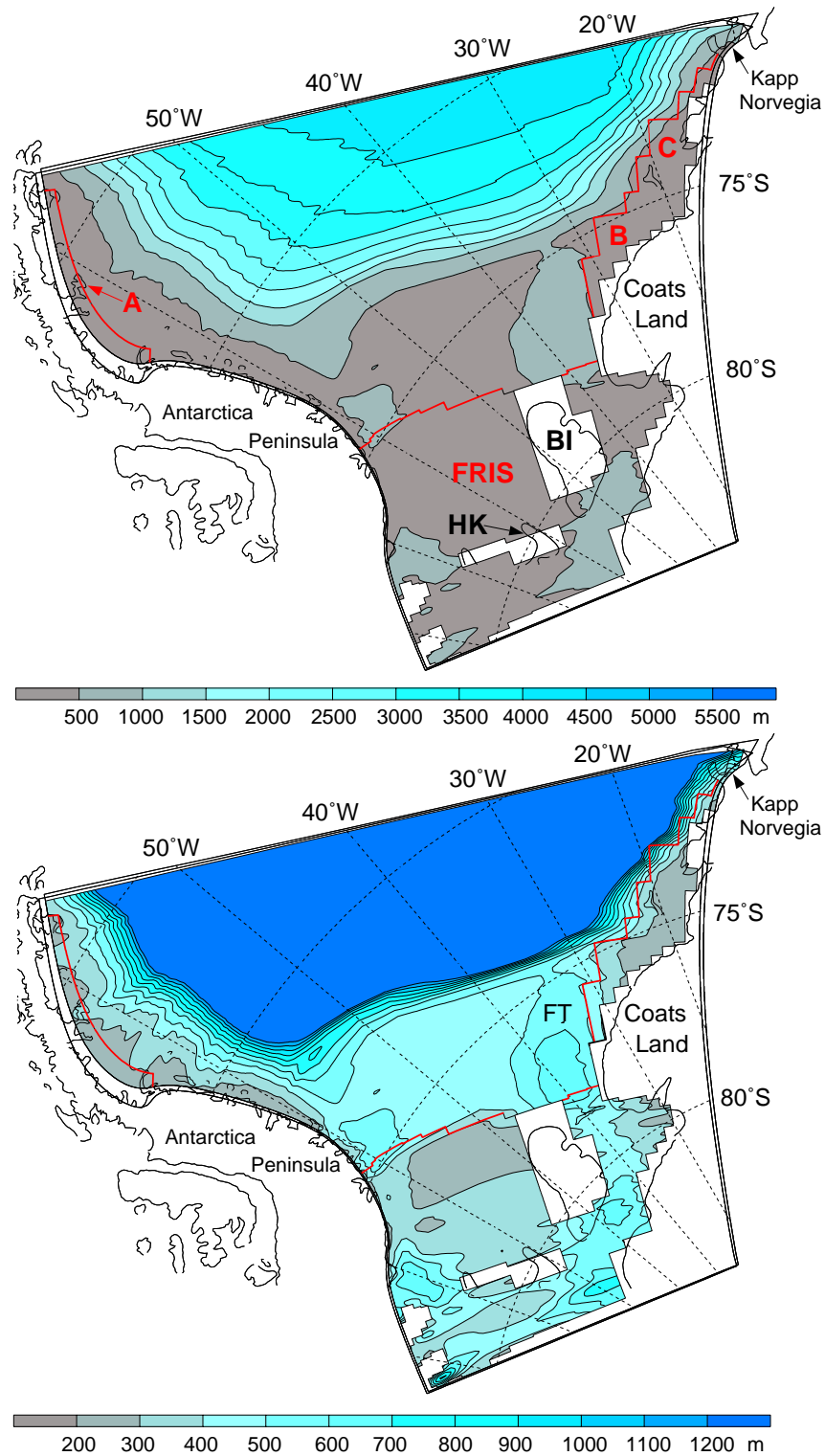


Figure 4.7: Water column thickness, ice shelves and islands of the inner Weddell Sea sector as represented by BRIOS4.4 grid. Upper: ice shelves included are: Larsen (A), Ronne and Filchner (FRIS), Brunt (B), and Riiser-Larsen (C). The islands are: Berkner (BI) and the Henry and Korff Ice Rises (HK). Below: the same as before, but with a detailed water column thickness beneath ice shelves regions. Filchner Trough (FT) is indicated.

others). Holloway and Barnes [1998] employed this parameterization when investigating the bottom boundary layer flow and the vertical structure of internal tides on the continental slope. They found generally good agreement between model results and observations.

Mellor and Yamada [1982] developed four levels of a turbulence closure scheme, which use the equations of motion and turbulent kinetic energy in progressively simplified form, from level 4 to the least complex level 1. Level 2 provides algebraic expressions for the vertical coefficients AKv and AKd , since the mixing length l is specified. For level 2.5, l is not specified, requiring necessarily the solution of the turbulent kinetic energy and the turbulence mixing length equations. Turbulent energy is produced through vertical shear (V_s) and buoyancy (B):

$$\frac{\partial TKE}{\partial t} = \underbrace{AKv \left[\left(\frac{\partial u}{\partial z} \right)^2 + \left(\frac{\partial v}{\partial z} \right)^2 \right]}_{V_s} - \underbrace{AKd N^2 + \frac{\partial}{\partial z} \left(AKq \frac{\partial TKE}{\partial z} \right)}_B \quad (4.1)$$

where AKq is the vertical diffusivity of the turbulent kinetic energy TKE and N is the Brunt-Väisälä frequency. Eq. 4.1 is a linearized one-dimensional version of the full turbulent kinetic energy equation with all lateral derivatives set to zero [Haidvogel and Beckmann, 1999].

The stability functions (or damping functions, necessary to damp or enhance turbulent exchange for stable or unstable stratification) are derived from the quasi-equilibrium model of Galperin *et al.* [1988] (see also Appendix C). The background vertical viscosity and diffusivity were set to $10^{-5} \text{ m}^2 \text{ s}^{-1}$.

The horizontal viscosity and diffusivity coefficients were chosen to be a quadratic function of the horizontal grid spacing Δ ,

$$\nu_{u,v} = \max \left(10^4 \text{ m}^2 \text{ s}^{-1} \left(\frac{\Delta}{\Delta_{max}} \right)^2, 10^2 \text{ m}^2 \text{ s}^{-1} \right)$$

This was necessary due to strongly varying grid sizes (Subsection 4.3.1). In the cross-shelf direction, ν_v is typically $1000 \text{ m}^2 \text{ s}^{-1}$. Lateral mixing occurs along geopotential surfaces for tracers while for momentum it takes place along constant s -surfaces (as in the other 3-D BRIOS models, Beckmann *et al.* [1999]; Timmermann *et al.* [2001]).

The bottom stress is taken in quadratic form as described in Subsection 3.1.2, except that velocities are the bottom values and not the vertically integrated. Beneath the ice shelves, the boundary layer stress is applied both at the ice base and the seabed to account for the additional

drag at the ice-water interface.

4.3.3 Initialization, time integration and harmonic analysis

In polar environments, water density at temperatures near freezing is strongly controlled by salinity and less influenced by temperature. For this reason, one single state variable (potential density) was used to characterize the stratification.

Climatological data sets could not be used as initial fields for the tidal model, since one aim of this study is to investigate the effect of the seasonal density variability on the structure of the three-dimensional tidal currents. Therefore, initial potential density fields were taken from the BRIOS-2.1 coupled sea ice-ocean model. This model has shown to simulate the water mass distribution in the Southern Ocean quite reliably [Timmermann *et al.*, 2001]. For initialization of the tidal model, monthly means of March and September 1987 were chosen which are typical summer and winter months. The data was interpolated trilinearly to the BRIOS4.4 grid.

The model time step is limited by the cross-shelf grid resolution; it is set to 10 seconds for the depth-dependent mode and 5 seconds for the depth mean mode. The internal mode is time stepped using a third-order Adams-Bashforth scheme [Haidvogel and Beckmann, 1999]. The model was integrated for 40 days. For longer integrations (of the order of months to years), atmospheric, sea ice and ice shelf thermohaline forcing has to be included to maintain the seasonal pycnocline. Otherwise, the main features of the density field would be destroyed due to tidally induced mixing.

The last 20 days of model results (barotropic and baroclinic velocities and free surface elevation) were harmonically analyzed using the same algorithms [Foreman, 1977; 1978] as described in the previous chapter. This length of time series was chosen, because after the first 20 days the domain-integrated energy contained in the baroclinic mode was already stable. In addition, the series is long enough to separate both semidiurnal (M_2 and S_2) tidal constituents without aliasing.

4.4 Density Field Beneath FRIS and in the Southern Weddell Sea and its Seasonal Variation

A short overview about the main characteristics of the vertical and horizontal stratification of the southern Weddell Sea and beneath FRIS will be given here. Details of the seasonal density variations and the water mass distribution will also be described. Since no observations exist with regard to the winter stratification on the southern Weddell Sea continental shelf, its description will rely on the results of the BRIOS-2.1 coupled sea ice-ocean model [Timmermann *et al.*, 2001].

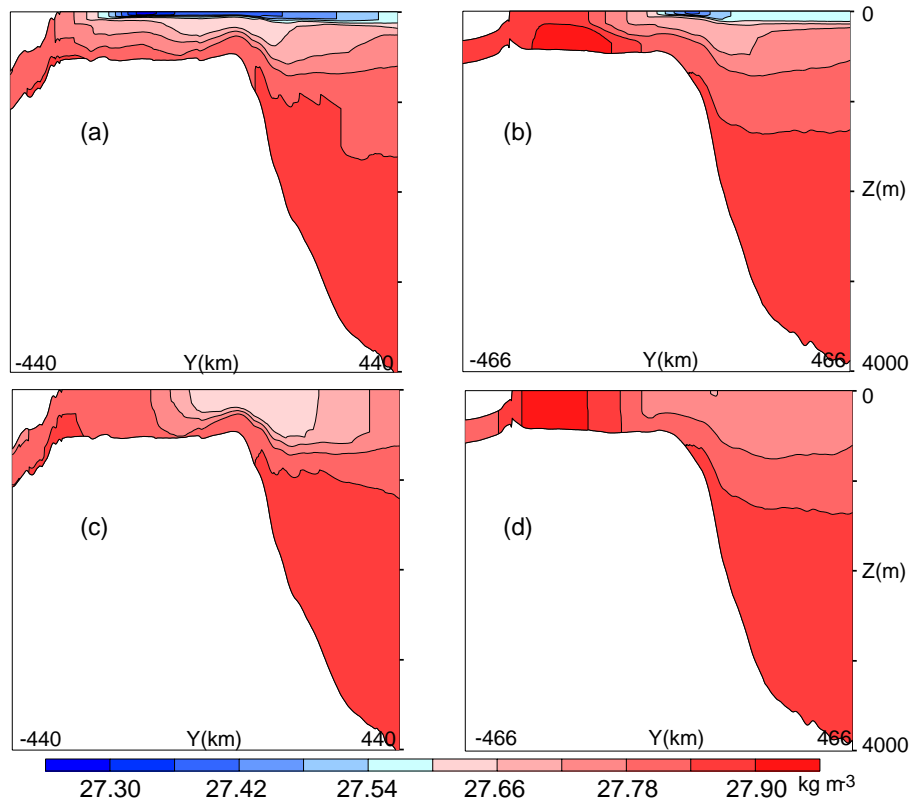


Figure 4.8: Vertical stratification (potential density, kg m^{-3}) in the eastern (left) and western (right) Weddell Sea during summer (upper) and winter (lower). Plotted are the model initial potential density fields.

On the continental shelf of the southern Weddell Sea, several water masses lie in close proximity. Low Salinity Shelf Water (LSSW) exists typically at the bottom on the narrow continental shelf east of the Filchner Trough (see Fig. 4.7 for reference). It is characterized by relatively low salinities, 34.28-34.44, and potential temperatures between -1.8°C and -1.6°C (potential density $\rho \approx 27.64 \text{ kg m}^{-3}$) [Carmack and Foster, 1975]. LSSW flows westwards with the coastal current towards the Berkner Shelf. There, it encounters High Salinity Shelf

Water (HSSW, $\rho \approx 27.95 \text{ kg m}^{-3}$) produced mainly during winter due to freezing and brine rejection [Gill, 1973; Foldvik *et al.*, 1985b]. This implies that on the western continental shelf denser water is found at the bottom than to the east (Fig. 4.8a and b).

HSSW formed on the Berkner Shelf drains into the Filchner Trough and flows underneath the Filchner Ice Shelf. Here, it is cooled to the *in situ* freezing point ($T < -2.2^\circ\text{C}$) and diluted by glacial melt water to form Ice Shelf Water (ISW, $\rho \approx 27.88 \text{ kg m}^{-3}$) [Carmack and Foster, 1975]. ISW flows out of the cavity and fills up the Filchner Trough below 300 m. It also penetrates onto the western shelf in a thin layer near the bottom close to the ice shelf edge, being forced up by the denser HSSW near the bottom [Foldvik *et al.*, 1985b].

Mixing between Warm Deep Water ($\rho \approx 27.82 \text{ kg m}^{-3}$, mean depth of 500-1000 m) and the overlying Winter Water ($\rho \approx 27.64 \text{ kg m}^{-3}$, mean depth of 100 m) produces Modified Warm Deep Water (MWDW, $\rho \approx 27.77 \text{ kg m}^{-3}$, mean depth of 350 m). This mixing is especially effective at the shelf break, where MWDW invades the continental shelf [Foster and Carmack, 1976].

Due to its high compressibility at low temperatures, ISW sinks towards the deep Weddell Sea basin continuously mixing with surrounding waters to form Weddell Sea Bottom Water ($\rho \approx 27.87 \text{ kg m}^{-3}$, mean depth of 4000 m) [Foldvik *et al.*, 1985c]. A schematic representation of the distribution of the above described water masses is shown in Fig. 4.9. Some of them can be easily identified in Fig. 4.8 using the approximate potential density cited for each water

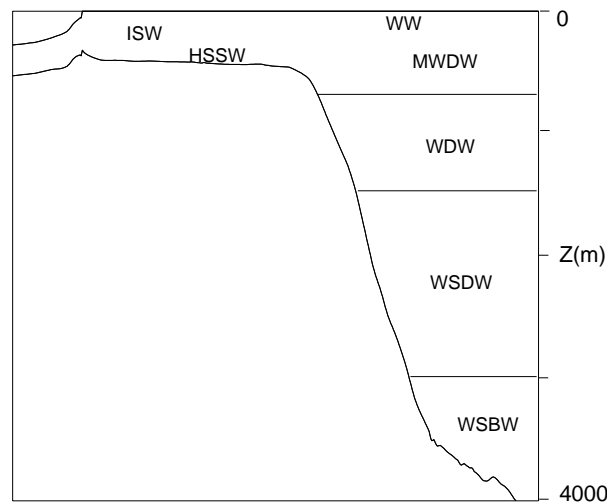


Figure 4.9: Schematic representation of the water masses of the southern Weddell Sea with Ice Shelf Water (ISW), High Salinity Shelf Water (HSSW), Winter Water (WW), Modified Warm Deep Water (MWDW), Warm Deep Water (WDW), Weddell Sea Deep Water (WSDW), and Weddell Sea Bottom Water (WSBW). On the eastern continental shelf of the Weddell Sea, HSSW is substituted by Low Salinity Shelf Water (LSSW).

mass.

In the southern Weddell Sea, the significant difference between summer and winter stratification is restricted to the near surface [Carmack, 1974]. During summer, radiation warms and sea ice melting freshens the surface layer increasing the strength of the pycnocline (Fig. 4.10a). In winter, this lighter water is replaced by denser water (Fig. 4.10b) due to sea ice formation and related brine rejection which decreases the strength of the pycnocline. Typically, the stratification below the pycnocline in the southern Weddell Sea is weak, leading values of N^2 of the order of 10^{-6} s^{-2} (Fig. 4.10).

In the FRIS cavity, the stratification of the water column is also subject to seasonal variation [Nicholls, 1996]. Because sea ice is not formed in the coastal polynya during summer, the HSSW reservoir and consequently, the inflow of HSSW into the cavity decreases. This changes the HSSW volume in the cavity causing a reduction by 50-60 m in the thickness of the HSSW layer in the western cavity [Nicholls, 1996].

A frontal system located near the shelf-break separates the shelf regime from the open ocean (Fig. 4.8a and b). During winter, the front is narrower leading to a stronger horizontal density gradient (Fig. 4.8c and d).

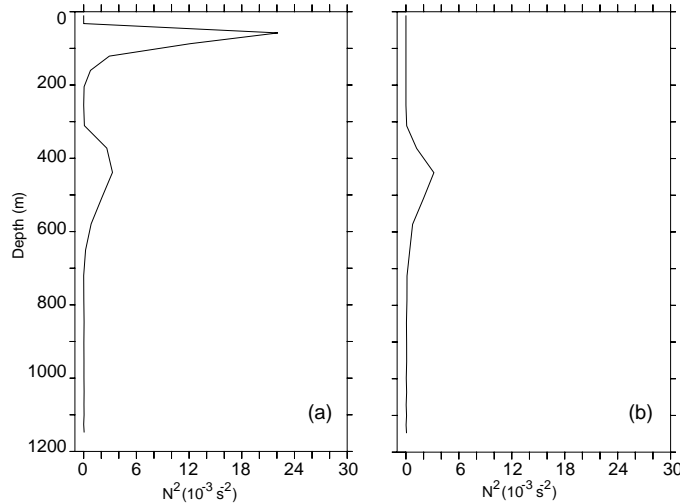


Figure 4.10: Vertical profiles of Brunt-Väisälä frequency (s^{-2}) for summer (a) and winter (b) from the slope of the southern Weddell Sea.

4.5 Generation and Propagation of Internal Tides in the Southern Weddell Sea

Before analyzing the results obtained with the 3D-model, it is interesting to make use of some analytical equations and the linear internal wave theory (LIWT, Section 4.1) to understand the possible spatial distribution and characteristics of an internal tide in the southern Weddell Sea.

In addition to the strength of the impinging barotropic currents, the two other fundamental factors influencing the internal tide generation are the vertical and horizontal variations of the stratification and the bottom topography. According to Baines [1982], the amplitude of the forcing function (F) for the internal tide in an along-slope (x - z) section (F_x) and cross-slope (y - z) section (F_y) are given by

$$F_x = \frac{\rho_0 Q_x N^2 z}{\omega_t h^2} \frac{dh}{dx} \quad \text{and} \quad F_y = \frac{\rho_0 Q_y N^2 z}{\omega_t h^2} \frac{dh}{dy} \quad (4.2)$$

where Q_x is the along-slope and Q_y the cross-slope volume flux due to the barotropic tide, N the buoyancy frequency, h water depth, ω_t the tidal frequency, ρ_0 a reference density, and dh/dx and dh/dy are the along- and cross-shelf topography slopes, respectively.

The distribution of F_x and F_y is shown in Fig. 4.11 at a depth of ≈ 400 m (depth at which N^2 has a maximum in winter and summer, see Fig. 4.10). Only results considering summer stratification on the southern Weddell Sea continental shelf are presented. Using winter stratification, slightly reduced values of both components of F were obtained, but the spatial

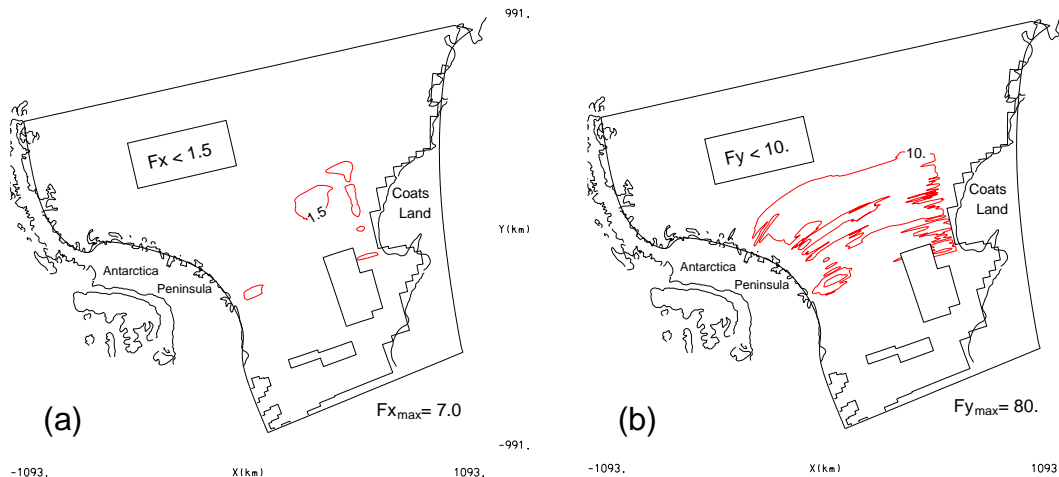


Figure 4.11: Contour of the along- (a) and cross-slope (b) internal tide forcing function F_x and F_y (10^5 Nm^2) for summer stratification on the southern Weddell Sea continental shelf.

distribution and the ratio between F_x and F_y were approximately the same as for summer. Since the semidiurnal barotropic tidal ellipses (Fig. 3.13) are almost perpendicular to the shelf-break, the along- and cross-slope volume fluxes were computed based on the semi-minor and semi-major axes of the barotropic M_2 tidal ellipse, respectively. Thus, F_x and F_y reflect only the contribution of the M_2 barotropic tidal current. A very similar spatial distribution and magnitude was obtained for S_2 .

The along-slope component of the forcing function (Fig. 4.11a) has its maximum only at places where the steepest gradient in the along-slope direction is found, like in the Filchner Trough (see Fig. 4.7 for reference). Compared to the cross-slope component (Fig. 4.11b), its magnitude is approximately 8 times smaller. In the case of F_y , high values are found on the whole southern continental shelf and at the shelf break. From this analysis it is clear that along-slope variations in topography and stratification are expected to contribute much less than the cross-slope variations to the generation of internal tides.

In a stratified medium, the interaction of a barotropic Kelvin wave with bottom topography may convert part of the barotropic energy to baroclinic Kelvin waves, baroclinic Poincaré waves, or higher frequency internal gravity waves [LeBlond and Mysak, 1978]. Most of the semidiurnal tidal energy propagates as a barotropic Kelvin wave in the Weddell Sea, but in some areas near the continental shelf break tidal energy propagates as a Poincaré wave, as was shown in Subsection 3.4.3. Therefore, the linear internal wave theory can be used to investigate possible probable sites where internal tides can be expected in the southern Weddell Sea.

The linear internal wave theory was applied to six slices indicated by numbers (from 1 to 6) in Fig. 4.12. These are the slices located in the region where barotropic tidal energy fluxes cross the continental shelf break almost perpendicularly (Subsection 3.4.3). N corresponding to summer stratification at the bottom was used to calculate the ratio γ . Since the density profile near the bottom is not significantly different between summer and winter, this analysis and the following discussion are applicable to both seasons.

In Figs. 4.13 and 4.14, γ is plotted against the topography profile for each of the cross-sections, considering M_2 and S_2 , respectively. For values $\gamma > 1$ ($\gamma < 1$) (dashed line, Fig. 4.13 and Fig. 4.14), the slope is supercritical (subcritical). γ is not plotted south of the M_2 critical latitude ($\omega < f$) (Fig. 4.12), and in other regions like the deep ocean where no significant stratification exist ($N \approx 0$) to generate internal tides.

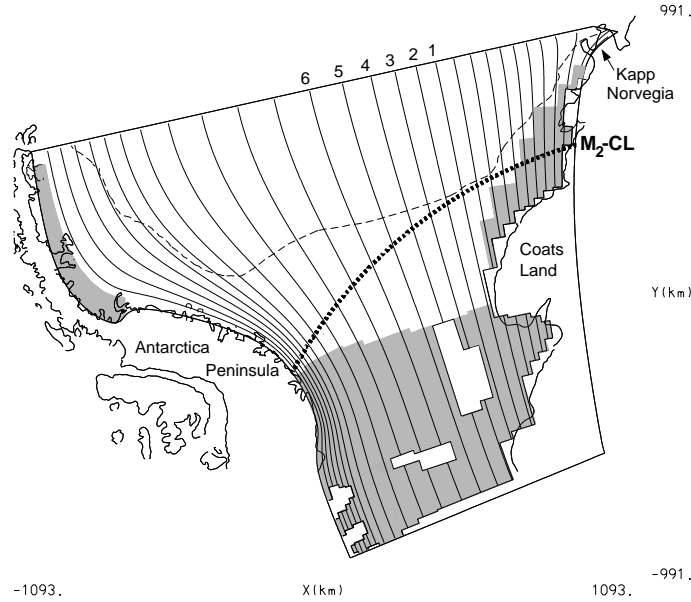


Figure 4.12: Distribution of meridional gridlines in the model domain. The numbers indicate those slices for which the internal tide results are presented in following figures and sections. The thin dashed line indicates the 1000 m isobath, and dots indicate the M_2 critical latitude. Ice shelf areas are shaded in gray.

For ω corresponding to the M_2 frequency ($1.40518 \times 10^{-4} \text{ rad s}^{-1}$), the lower continental slope is, in general, subcritical while the upper slope is supercritical (Fig. 4.13). Only for few segments of the lower-middle slope a critical value ($\gamma \approx 1$) is found, which may generate M_2 internal tides propagating along-slope. Although for slices 5 and 6 a broader area lies in the range of $\gamma \approx 1$, these slices are located at the middle of the southern Weddell Sea shelf break (Fig. 4.12) where the barotropic tidal energy vectors are parallel to the slope (Fig. 3.15). Hence, the forcing mechanism does not have its maximum for internal tide generation, and internal tides are not expected.

In the case of the S_2 frequency ($1.454441 \times 10^{-4} \text{ rad s}^{-1}$), most of the continental shelf and slope are subcritical (Fig. 4.14). Only short segments near the shelf break are supercritical. The analysis of γ indicates that internal tides will not be generated and tidal currents at this frequency would be mainly barotropic.

4.6 Representation of the Barotropic Surface Tides in the 3D-Model

The barotropic results (tidal amplitude and currents) obtained with the grid 4.4 are similar to those obtained with the grid 4.3 (Chapter 2); they will only be briefly presented here to show that the forcing term driving the baroclinic tide is modeled with sufficient accuracy.

Semidiurnal tidal amplitudes and Greenwich phases (Fig. 4.15a and b) are basically the

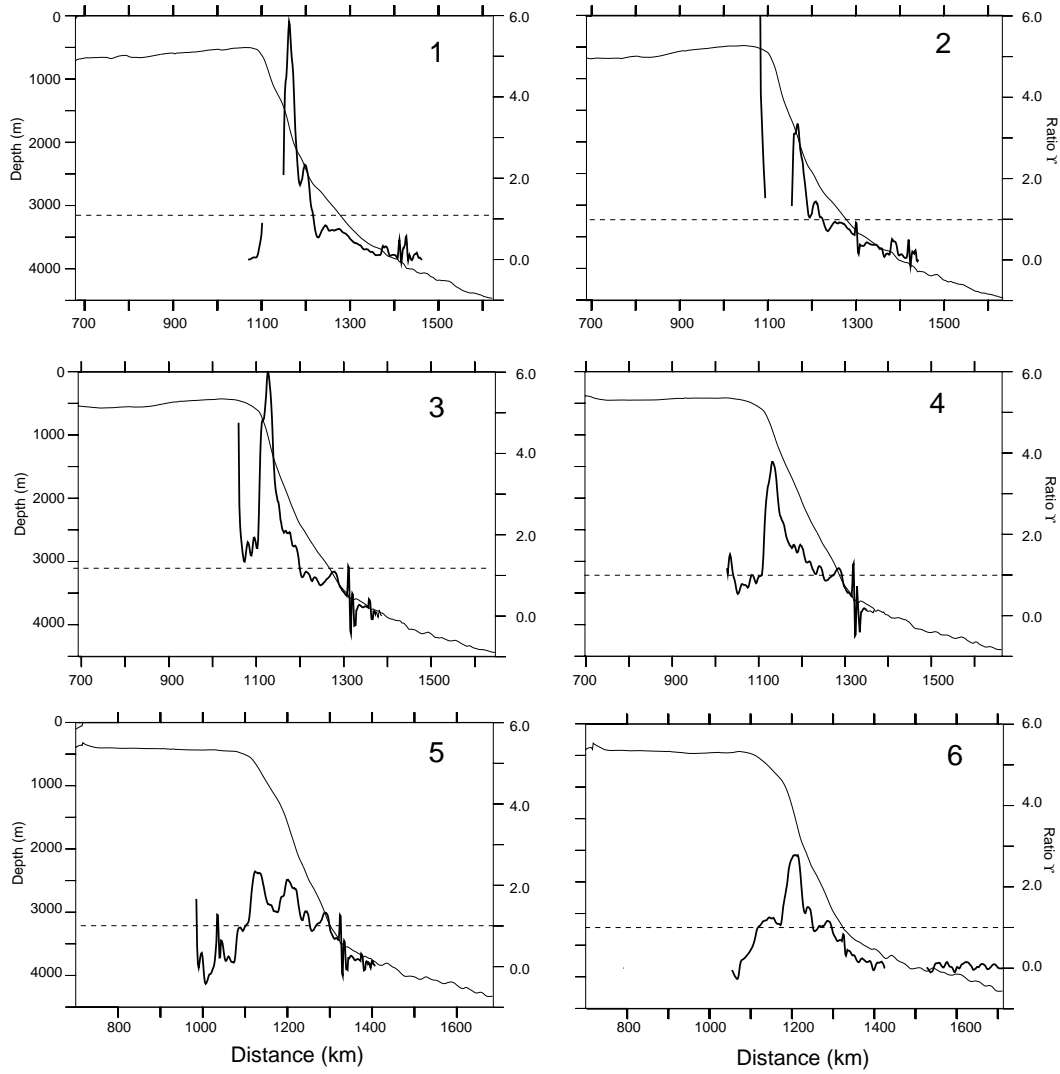


Figure 4.13: Ratio γ related to the M_2 frequency plotted together with bottom topography for the cross-slices shown in Fig. 4.12. The dashed line marks $\gamma=1$.

same as shown in Fig. 3.10. In Fig. 4.15c, the amplitudes of the surface tides for M_2 and S_2 are plotted against tide gauge observations from the Filchner-Ronne Ice Shelf edge [Doake, 1992] as was done for results using the grid 4.3 (Fig. 3.11). Compared to the previous results, less agreement was obtained with the three-dimensional grid due to the coarser resolution employed in the along-slope direction. However, this difference will not affect significantly the generation of the internal tide and the baroclinic tidal currents.

4.7 Baroclinic Tides at the M_2 Frequency

In the next subsections, baroclinic tidal currents will be analyzed based on the theories presented in the previous sections of this chapter. The presentation is divided in two parts: the

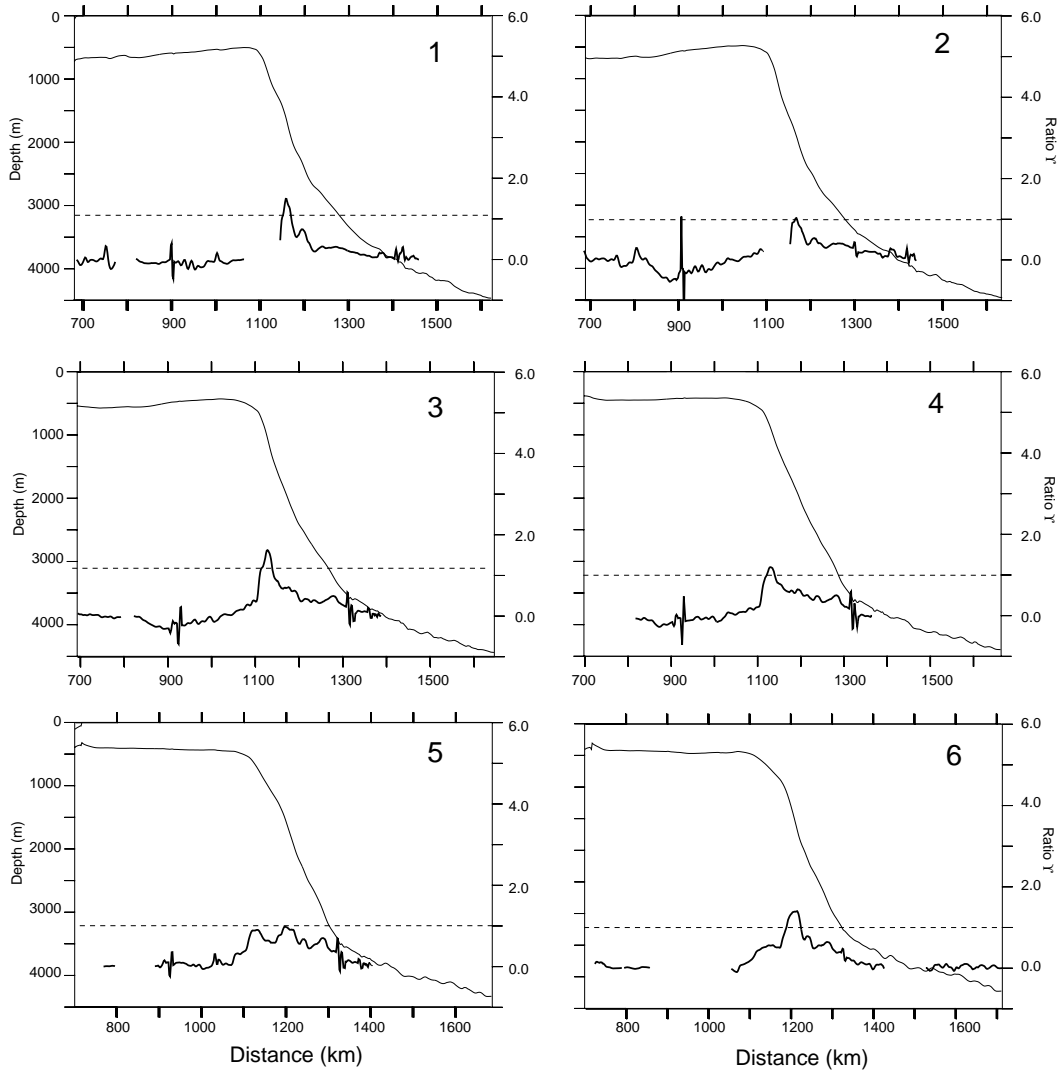


Figure 4.14: Ratio γ related to the S_2 frequency plotted together with bottom topography for the cross-slices shown in Fig. 4.12. The dashed line marks $\gamma=1$.

shelf and shelf break areas and the Filchner-Ronne Ice Shelf cavity. These environments are fundamentally different due to the permanent, thick ice lid of FRIS.

4.7.1 M_2 tidal currents on the continental shelf and at the shelf break

In Fig. 4.16, M_2 major axes of the tidal ellipse for summer stratification are presented. The number inside each figure indicates the slice position in the Weddell Sea (see Fig. 4.12).

Differences in topography and density structure between the six cross-slope sections cause the differences of the baroclinic tidal currents and internal tidal structure for each cross-section. In general, summer and winter stratifications produce similar pattern and magnitude of the horizontal tidal currents. Since the density profiles are only different near the surface, small

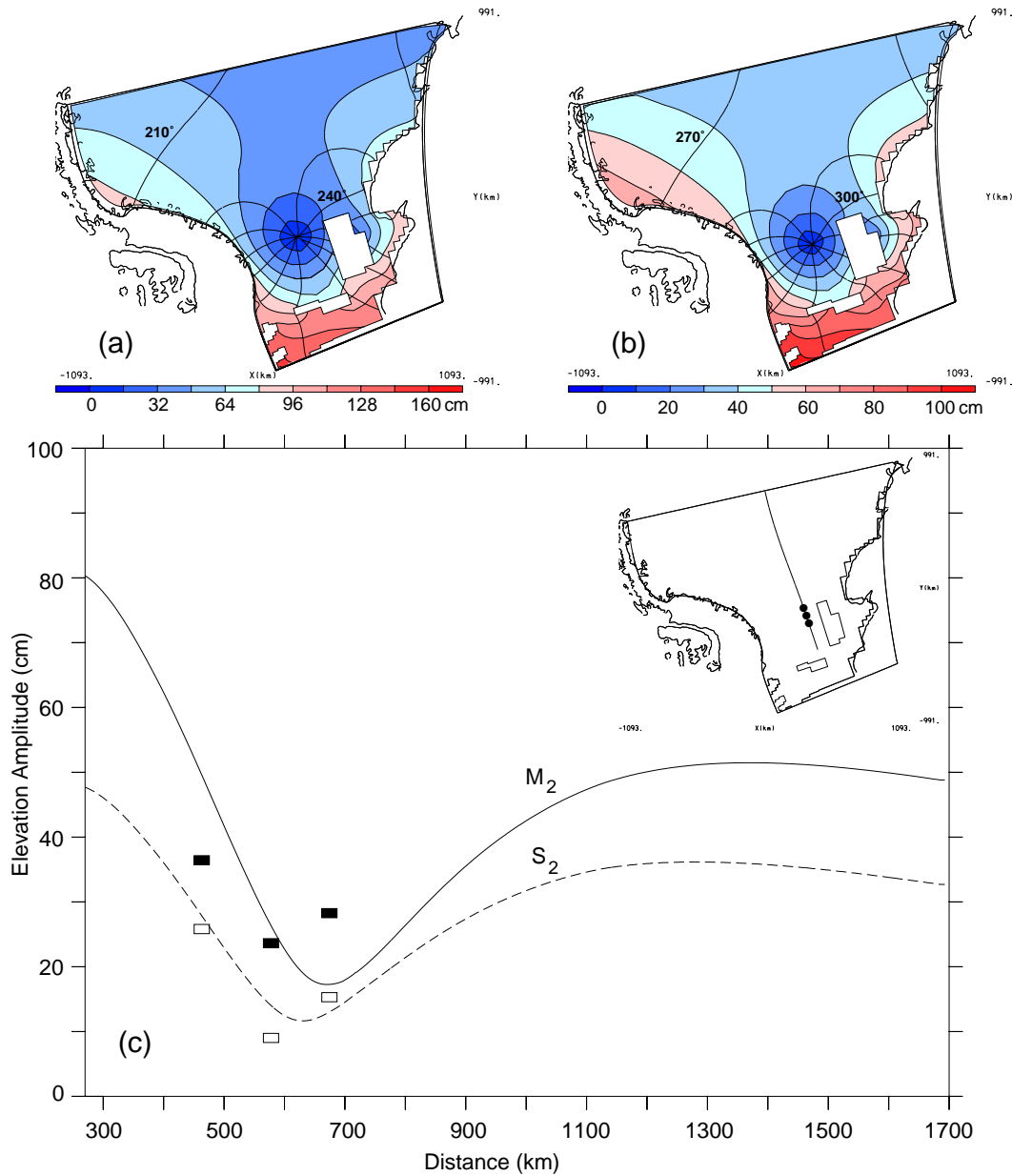


Figure 4.15: Tidal amplitudes (cm) and Greenwich phases (degrees) for tidal frequencies M₂ (a) and S₂ (b) obtained with the grid 4.4. Note that a and b have different color scales. (c) Comparison between modeled M₂ (solid line) and S₂ (dashed line) amplitudes and observations (M₂, black rectangles and S₂, white rectangles). Slice and tide gauge positions used for this comparison are indicated in the inset.

differences between the major axis are found close to the pycnocline: summer major axes are about 0.5 to 1 cm s^{-1} stronger than in winter (not shown). For both seasons, the amplitude of the major axis is bigger on the continental shelf and shelf break ($\approx 7 \text{ cm s}^{-1}$) than in deep ocean, increasing towards the ice shelf edge to ≈ 10 to 14 cm s^{-1} in the mid water column. Due to this, the following results and their discussion can be applied to both seasons.

Although tidal ellipse parameters of six moorings located at the FRIS edge were available

for model comparison, only four [Woodgate *et al.*, 1998; Foldvik *et al.*, 2001] were used which resulted from time series longer than 435 days. The other 2 moorings [Makinson and Nicholls, 1996] were deployed for a short period (less than 11 days) and their semidiurnal tidal ellipses are twice the magnitude of that obtained with longer time series.

Comparison of modeled and observed tidal ellipses near the FRIS edge (Fig. 4.17) shows a difference of approximately 10° between their orientations to the north. This may be related to a small discrepancy between exact position and orientation of the ice front and their representation in the model. In both cases, major axes of the semidiurnal tidal ellipses are aligned perpendicularly to the ice shelf edge. M_2 major axes at the FRIS front have a maximum of approximately 8 to 12 cm s^{-1} , decreasing near the bottom. In general, modeled M_2 tidal ellipses are underestimated (maximum of 37% at R2), but their sense of rotation and the eccentricity (major-axis/minor-axis) are in good agreement with the observations. Close to the coast (FR6) and to Berkner Island (FR3), ellipses become greatly flattened as already found for the barotropic tidal ellipses (Section 3.4.2) and explained as being characteristic for a Kelvin wave.

At site R2, the M_2 tidal ellipse changes from counterclockwise at 235 m to clockwise at 400 m (Fig. 4.17). Foldvik *et al.* [2001] explained this behavior based on the proximity of the M_2 critical latitude. At 400 m, the amplitude of the clockwise component of the tidal current (see Appendix A) is greater than the amplitude of the counterclockwise, thus the ellipse rotates clockwise. Because the counterclockwise component is depth-dependent near the critical latitude, it increases from the bottom upward. For this reason, at upper levels of the water column, M_2 tidal ellipses rotate counterclockwise.

The modeled tidal currents are strongly influenced by bathymetry and stratification. In this case, the location of the sites is not ideal for validating modeled currents because near the ice front, water column thickness changes instantly by hundreds of meters. Also, the coarse along-front grid resolution may influence the results. Despite these problems, the model achieved a reasonable fit to the data available from the FRIS edge.

At the slope, a first mode internal tide was generated at approximately the same location for each of the cross-slices in both seasons, being characterized by weak velocities (less than 1 cm s^{-1}) (Fig. 4.16). In order to interpret the generation and propagation of the internal tide, the results can be analyzed based on the linear theory of internal tide generation (Section 4.1).

Comparison between the cross-sections 1 to 4 in Figs. 4.16 and 4.13 shows that the internal

tide was generated at the slope near the critical value ($\gamma=1$). Since topography and vertical density profile vary along the cross-section and along the slope, \tilde{f} -terms (see Appendix C) and non-linearity are included, and the theory is highly idealized (friction and non-linear terms are neglected, and the topographic slope gradient and N are assumed to be constant), the generation and propagation of the internal tide is more complex than explained by the theory.

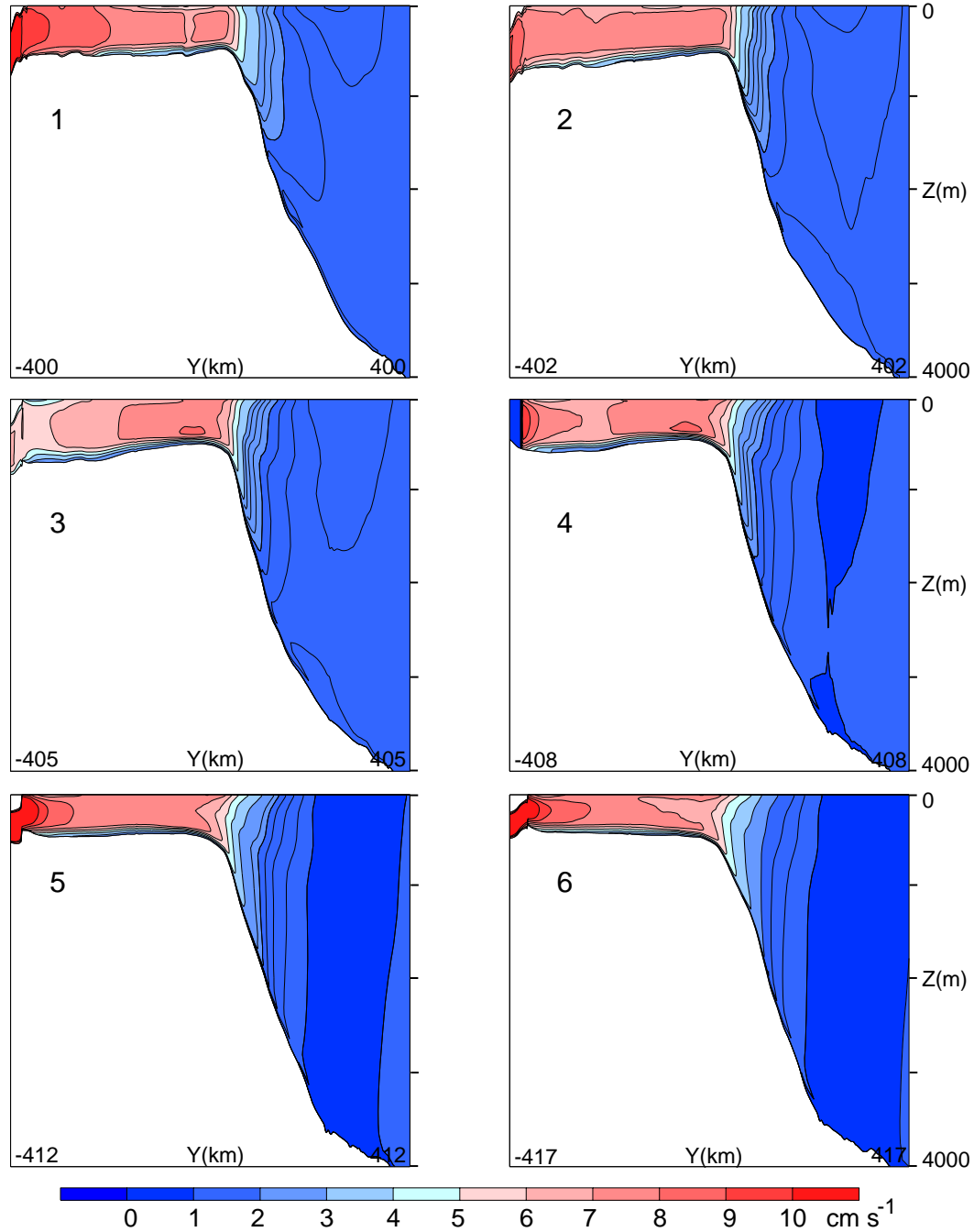


Figure 4.16: Major axis of the M_2 tidal ellipse (cm s^{-1}) considering summer stratification across vertical slices (y - z , Fig. 4.12) in the southern Weddell Sea.

Sensitivity experiments made with the tidal model to assess which of the above cited differences is most likely to be responsible for disagreements between theory and model have shown that especially topographic variations in the cross-slope direction have a strong effect on the generation site of the internal tide.

The phase of the internal tide increases westward from the location of its generation, in-

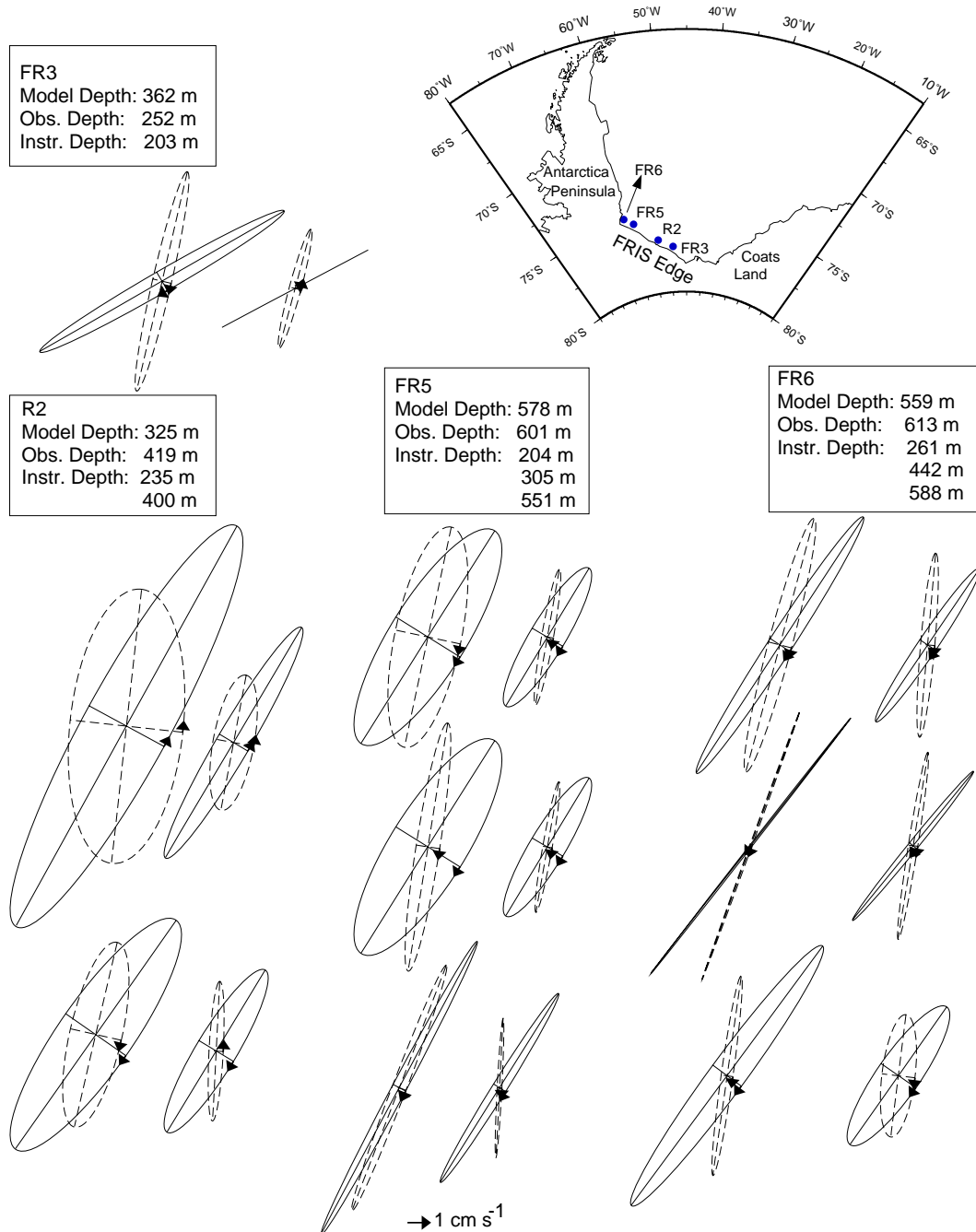


Figure 4.17: Comparison between modeled (dashed line) and observed (solid line) M_2 (left column each position) and S_2 (right) tidal ellipses at the FRIS edge. The map indicates positions and station.

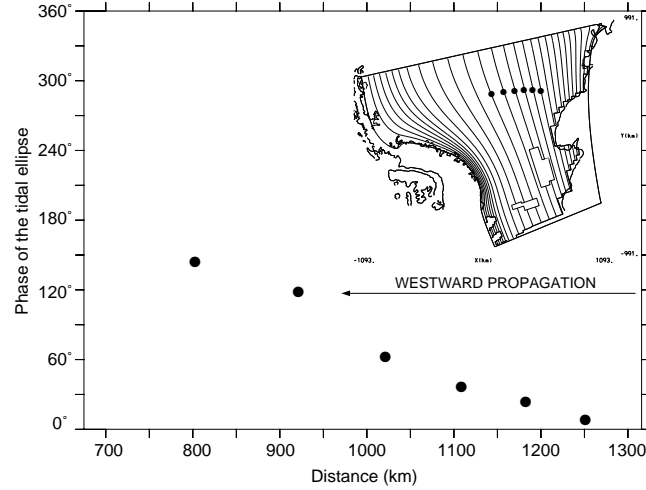


Figure 4.18: Phase of the M_2 tidal ellipse for the slices indicated in the inset showing the westward propagation of the internal tide.

dicating the along-slope propagation (Fig. 4.18). These results are largely consistent with the linear theory. The baroclinic tide dissipates rapidly while propagating westward for about 350 km, the approximate distance between its origin at slice 1 and slice 4¹. LeBlond [1966] studied the damping of internal gravity waves in a continuously stratified ocean, where the damping in the interior of his model was due to turbulence extracted from the mean flow and boundary layer dissipation. His results show that the dissipation of long internal waves in shallow basins is very high. This means that, besides damping by bottom friction, the energy source for internal tides (the barotropic tide) generates also their sink, which can be so strong that the e -folding distance can be just a few times the internal wave length [Maas and Zimmerman, 1989a].

Besides the baroclinic currents, the baroclinic response of the model is characterized also by internal vertical displacements at the tidal frequencies of the barotropic tide. The vertical velocity is harmonically analyzed and the corresponding values of the vertical displacement amplitude are calculated. If the vertical velocity amplitude for a tidal constituent is w_{tc} , then the vertical displacement amplitude (ζ) is

$$\zeta = \frac{w_{tc}}{\omega_{tc}} \quad (4.3)$$

where ω_{tc} is the frequency for a particular tidal constituent. In this case, the subscript tc refers to M_2 . As already commented by Xing and Davies [1998], (4.3) is only a linear approximation

¹Note that it is not a numerical artifact; an estimate of the numerical damping time scale for a perturbation with 100 km wavelength yields about two weeks, which is long compared to its semidiurnal period.

to the internal displacement and is, in essence, a scaled vertical velocity with the scaling factor ω_{tc} .

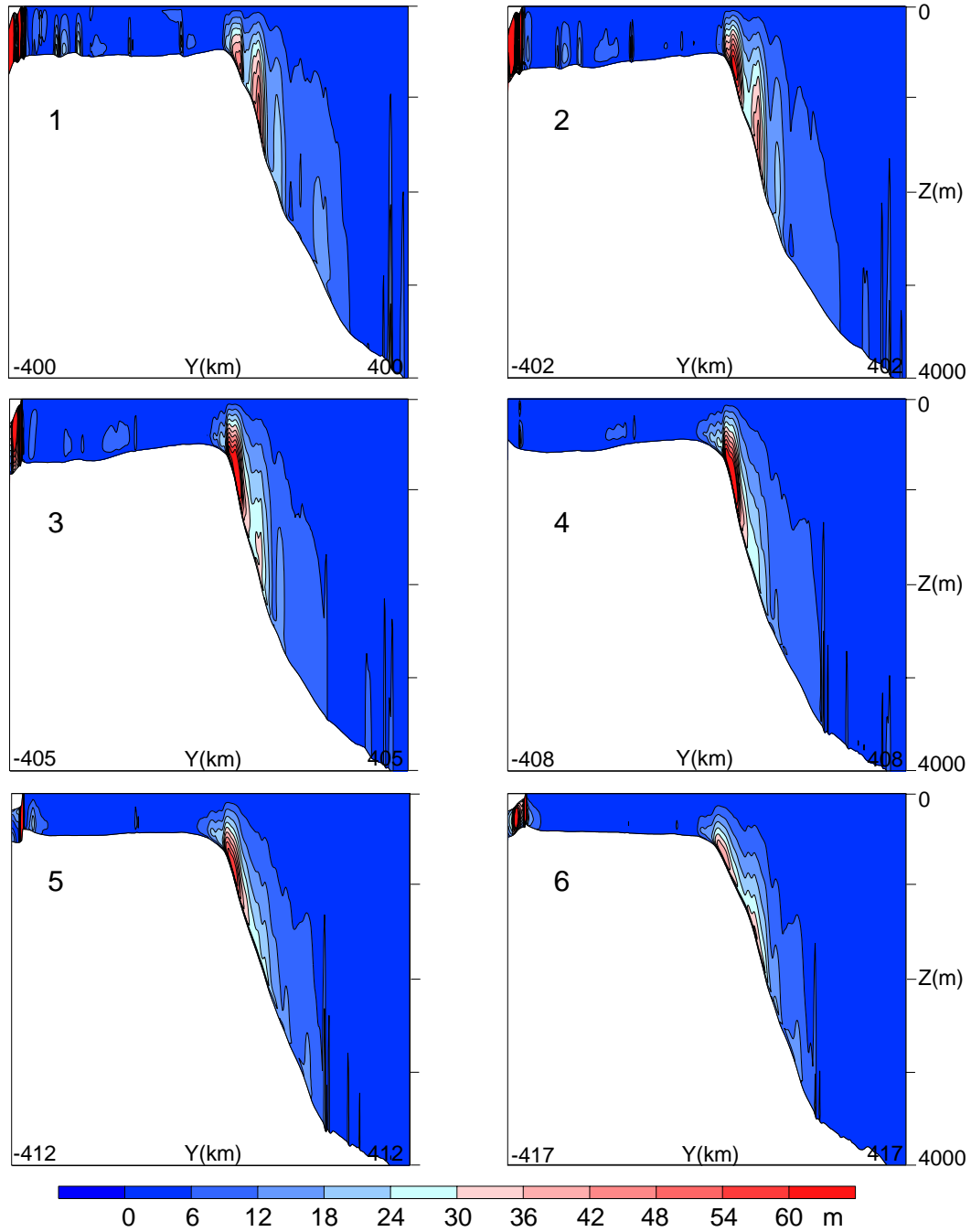


Figure 4.19: Amplitude of the M_2 vertical displacement (m) considering summer stratification across the vertical slices (y-z, Fig. 4.12) in the southern Weddell Sea.

Internal displacements have largest values near the seabed on the upper continental slope (Fig. 4.19), reaching 85 m. The area of high vertical displacements is limited to the near slope region, confirming again that the generated internal tide propagates along-slope. If any internal

tide would propagate offshore, then ζ would be as high in the deep ocean as at the slope. The major part of the internal displacement is caused by the reflection of the barotropic tide at the slope which behaves as a vertical wall; the internal tide produces a maximum displacement of 20 m. The strongest displacements occur in the eastern Weddell Sea, decreasing westward. On the shelf, vertical displacements are quite small, related to small bathymetric irregularities, but increase again at the FRIS edge due to the abrupt change in water column thickness which leads to strong vertical velocities.

Fig. 4.16 shows that a relatively thick bottom boundary layer develops on the shelf and near the shelf break region. In order to investigate the benthic layer, the M_2 tidal ellipses were decomposed into two counterrotating circular velocity components according to the method described in Appendix A and compared to observations (Fig. 4.20). All available current meter data [Middleton *et al.*, 1987; Foldvik *et al.*, 1990; Woodgate *et al.*, 1998] are from the eastern Weddell Sea shelf break, predominantly from the near bottom. Because mooring sites are located in a region where bathymetry changes rapidly, it was not always possible to match the grid points with the mooring position. Therefore, an agreement in depth was preferred since this is normally the most important factor influencing tidal currents.

Generally, modeled counter- and clockwise amplitudes agree well with the observations. Greater discrepancies (about 100°) are found for the phases, especially in Fig. 4.20a,e possibly related to small scale topography variations (along- and cross-slope) not represented in the model. Also, because the position of the amphidromic point is not accurately represented in the model (Section 4.6), it will produce some lag between the phase of the modeled and the observed surface wave which will be reflected in the phase of the currents. But such discrepancies will not affect other tidal processes (e.g., tidal mixing) and for this reason, can be considered less important. At all other points, modeled counter- and clockwise phases are relatively similar to observations.

As already observed by Foldvik *et al.* [1990] and expected from the theory (Section 4.1), the M_2 counterclockwise component (dashed line in Fig. 4.20) is depth-dependent due to the proximity of the critical latitude, leading to a bottom boundary layer up to 100 m thick. Stations located south and north of the M_2 critical latitude show similar increased layer thicknesses. In the middle of the water column, modeled tidal currents slightly increase upwards. Unfortunately, only the observations of Fig. 4.20e cover a major part of the water column. At this site,

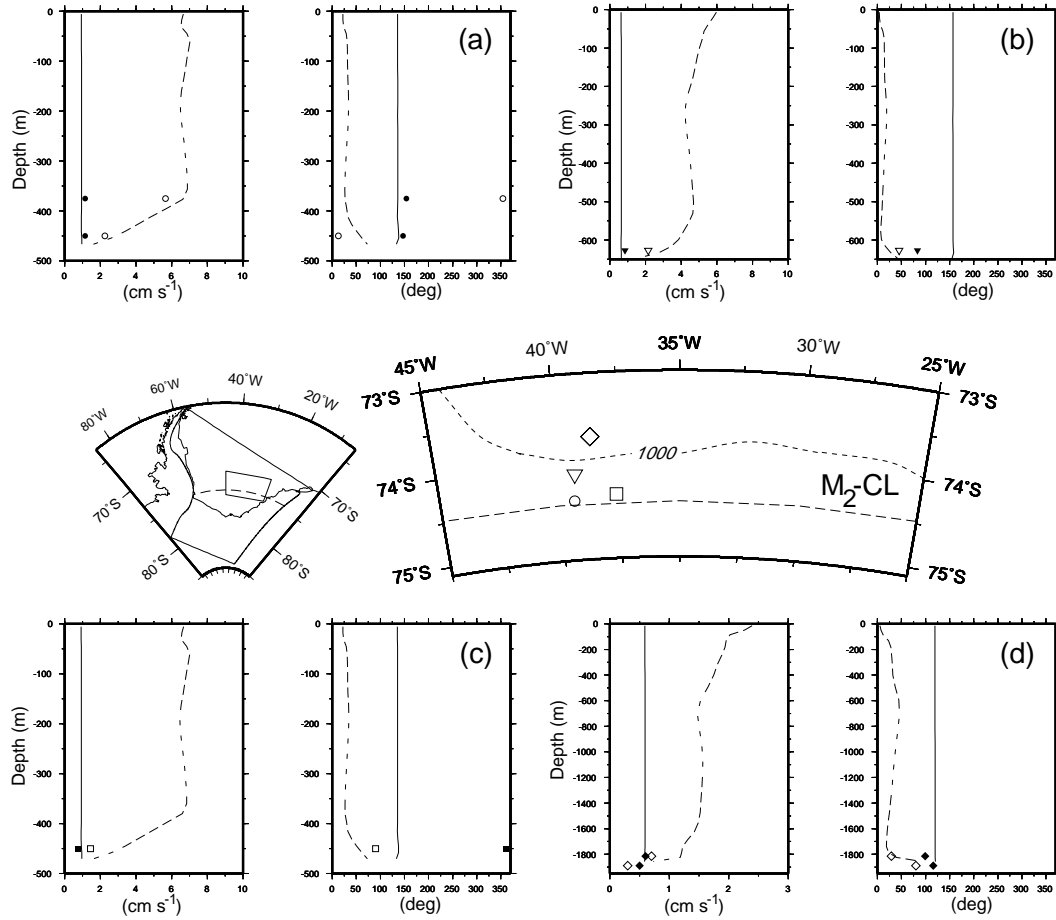
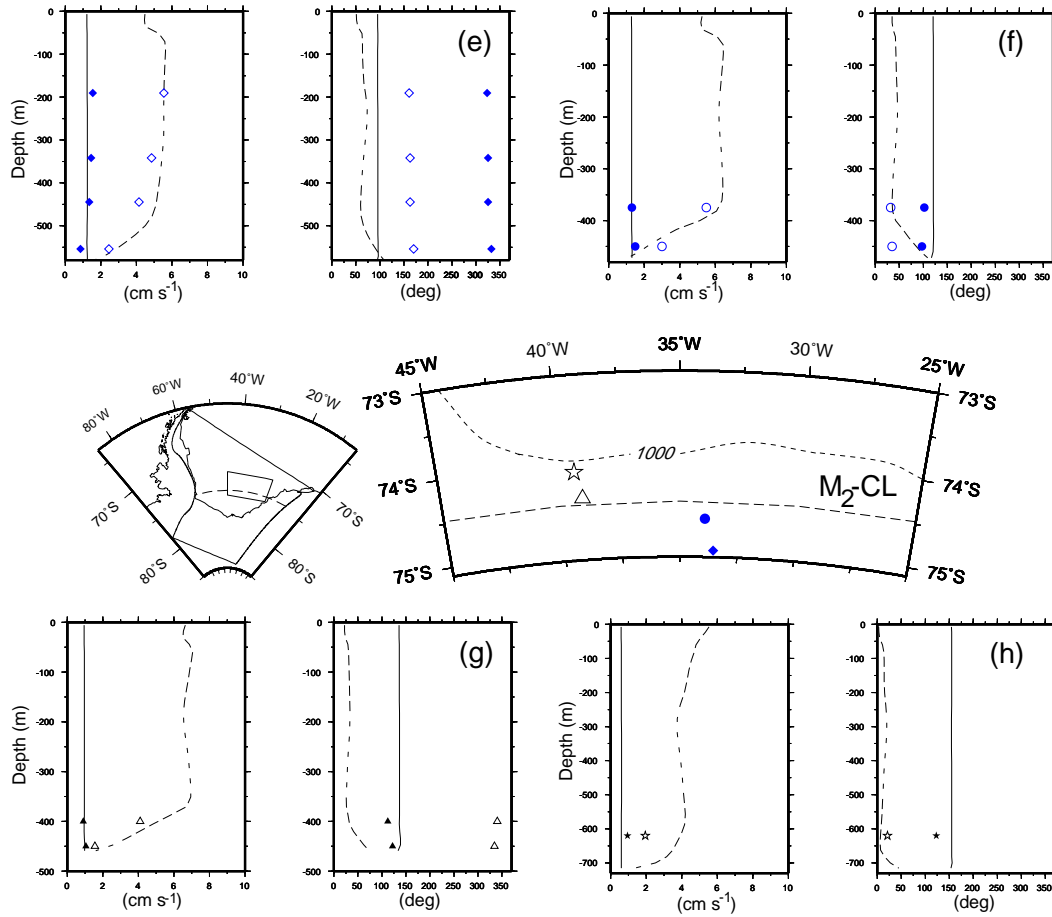


Figure 4.20: Comparison between modeled (solid and dashed lines) and observed (symbols) M_2 decomposed tidal ellipses in the shelf break region. Dashed line and not-filled symbols indicate counterclockwise, and solid line and filled symbols clockwise rotation. Each symbol corresponds to a different observation site that is indicated in the map. For each comparison, amplitude (left, cm s^{-1}) and phase (right, degrees) of the counter- and clockwise components are plotted. Dashed and dot lines in the map refer to the M_2 critical latitude and to the 1000 m isobath, respectively.

the observed tidal current profile appears to be slightly more depth-dependent than represented by the model with differences of the order of a few mm s^{-1}). The clockwise component is depth-independent with a small decrease in magnitude near the seabed due to bottom stress. The thickness and shape of the bottom boundary layer was successfully represented by the results.

The increased bottom boundary layer thickness near the critical latitude leads to reduced velocity shear near the bottom. This indicate less turbulent mixing in the boundary layer, but the mixing extends over a larger part of the water column. Similar vertical structure of tidal currents were obtained for the Barents Sea [Nøst, 1994; Furevik and Foldvik, 1996] which is located at the northern critical latitude of M_2 .

Associated with the pycnocline is a trapped wave which is responsible for the baroclinicity



Cont. Fig 4.20.

observed on the shelf (Fig. 4.16). For both seasons, this wave is present, but it has maximum currents during summer when the pycnocline is stronger. A time series of near surface potential density at a point located at the shelf (slice 1, Fig. 4.12) clearly shows the semidiurnal trapped wave signal and its symmetry over the tidal cycle (Fig. 4.21). It creates strong velocity shear near the surface (see Fig. 4.20), centered at about 20 m depth. The horizontal position of the trapped wave moves from the shelf (slice 1, Fig. 4.16) to the shelf break (slice 6, Fig. 4.16) in accordance with the density structure. The wave must propagate as an internal Kelvin wave, because its signal can be found in both sides of the critical latitude.

The high degree of spatial variability shown suggests that small changes in density field, details of topography, and geographical location produce a significant change in the tidal currents which makes it difficult to compare model results with observations.

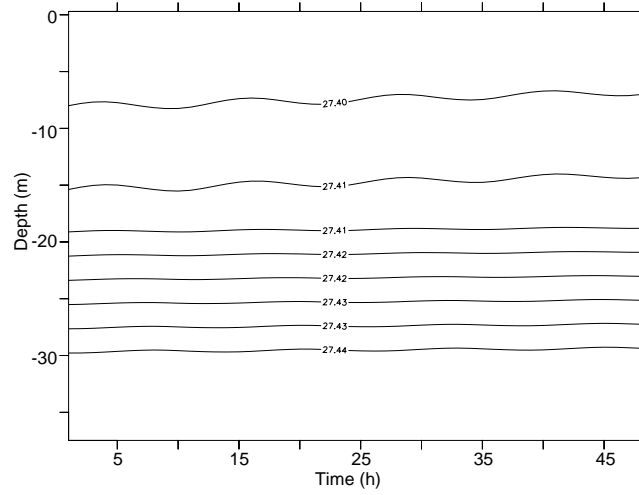


Figure 4.21: Contour of potential density (kg m^{-3}) near the surface over approximately two M_2 tidal cycles at a point located at the shelf break from slice 1 (Fig. 4.12).

4.7.2 M_2 tidal currents beneath Filchner-Ronne Ice Shelf

In this subsection, model results beneath Filchner-Ronne Ice Shelf are presented for the y - z slices shown in Fig. 4.22. These slices are considered to be representative for large parts of the cavity. As described in Section 4.4, beneath FRIS stratification does not show a strong seasonal variation as the near surface layer of the water column on the shelf and shelf break regions. Furthermore, semidiurnal tidal currents in open water were not significantly different for typical summer and winter stratification to modify the tidal response in the cavity. For

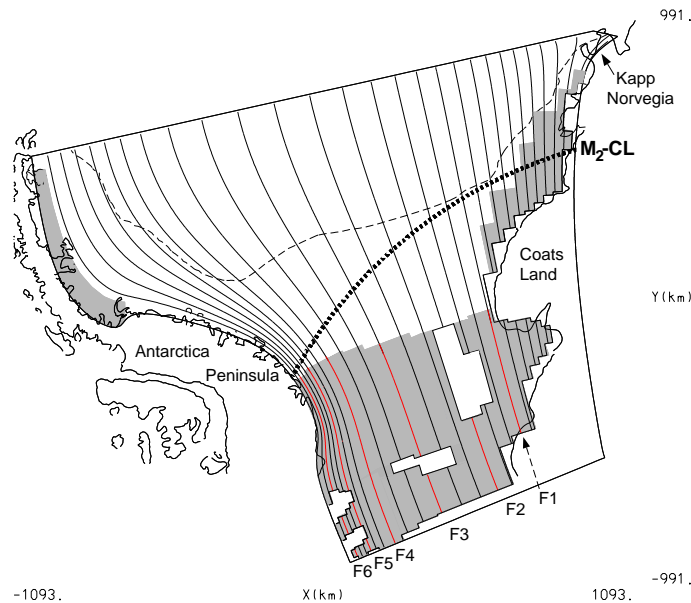


Figure 4.22: Position of y - z slices (red lines, labeled by letter/number) for which model results beneath FRIS are presented in the following figures and related subsections. The thin dashed line indicates the 1000 m isobath and, dots indicate the M_2 critical latitude (M_2 -CL). Ice shelf areas are gray shaded.

this reason, the following results presented for summer stratification are representative for both seasons.

In the FRIS cavity, the main factor controlling the magnitude of the major axis of the tidal ellipse is the water column thickness (Fig. 4.7): M_2 tidal currents tend to be strongest in regions where the water column is thin. This is the case in the northern and western parts of the cavity where the M_2 major axis reaches up to 20 cm s^{-1} (Fig. 4.23), decreasing to $4\text{--}6 \text{ cm s}^{-1}$ in deeper regions (e.g., south of Berkner Island, Fig. 4.23 slice F2). Due to frictional effects at the ice shelf base and seabed, the strongest velocities are found in the middle of the water column.

Modeled and observed M_2 tidal ellipses are compared for two drill sites (S2 and S3; Fig. 4.24) located at the Ronne Ice Shelf [Makinson and Nicholls, 1996]. At site S2, only the major axis of the tidal ellipse is available and, for this reason, the tidal ellipse is not plotted. Although the position of both sites is not ideal for model comparison (they lie close to small scale topographic features which may influence the axes magnitude and inclination of the tidal ellipse), they are the only available tidal measurements under FRIS.

At S3, despite the discrepancy between modeled and observed ice and water column thicknesses (Fig. 4.24), modeled tidal currents agree well with observations. The model can reproduce the shape of the M_2 tidal ellipse (eccentricity) and its sense of rotation. As for the modeled and observed ellipses from the FRIS edge (Fig. 4.17), the same lag in the ellipse inclinations is found for the ellipses under FRIS. This was expected since the lag may be related to the orientation of the ice shelf front.

At site S2, the observed mean M_2 major axis is 29.9 cm s^{-1} [Makinson and Nicholls, 1996] compared to the modeled value of $\approx 18 \text{ cm s}^{-1}$ in the middle of the water column. Tidal currents at this site were estimated from a thermistor cable suspended beneath the ice shelf [Robinson *et al.*, 1994]. The method applied for this estimation [Makinson and Nicholls, 1999] provides information only about the major axis of the tidal ellipse and makes several inappropriate assumptions; one of them is that tidal currents throughout the water column are assumed to be constant. Although the discrepancy between modeled and observed major axes at S2 can be related to the crude representation of the water column thickness in the east-west direction in the model, some error may also be attributed to the indirect method.

The modeled M_2 tidal ellipses for three points located in places with different water depths under FRIS were decomposed into the two counterrotating circular velocity components (Fig. 4.25).

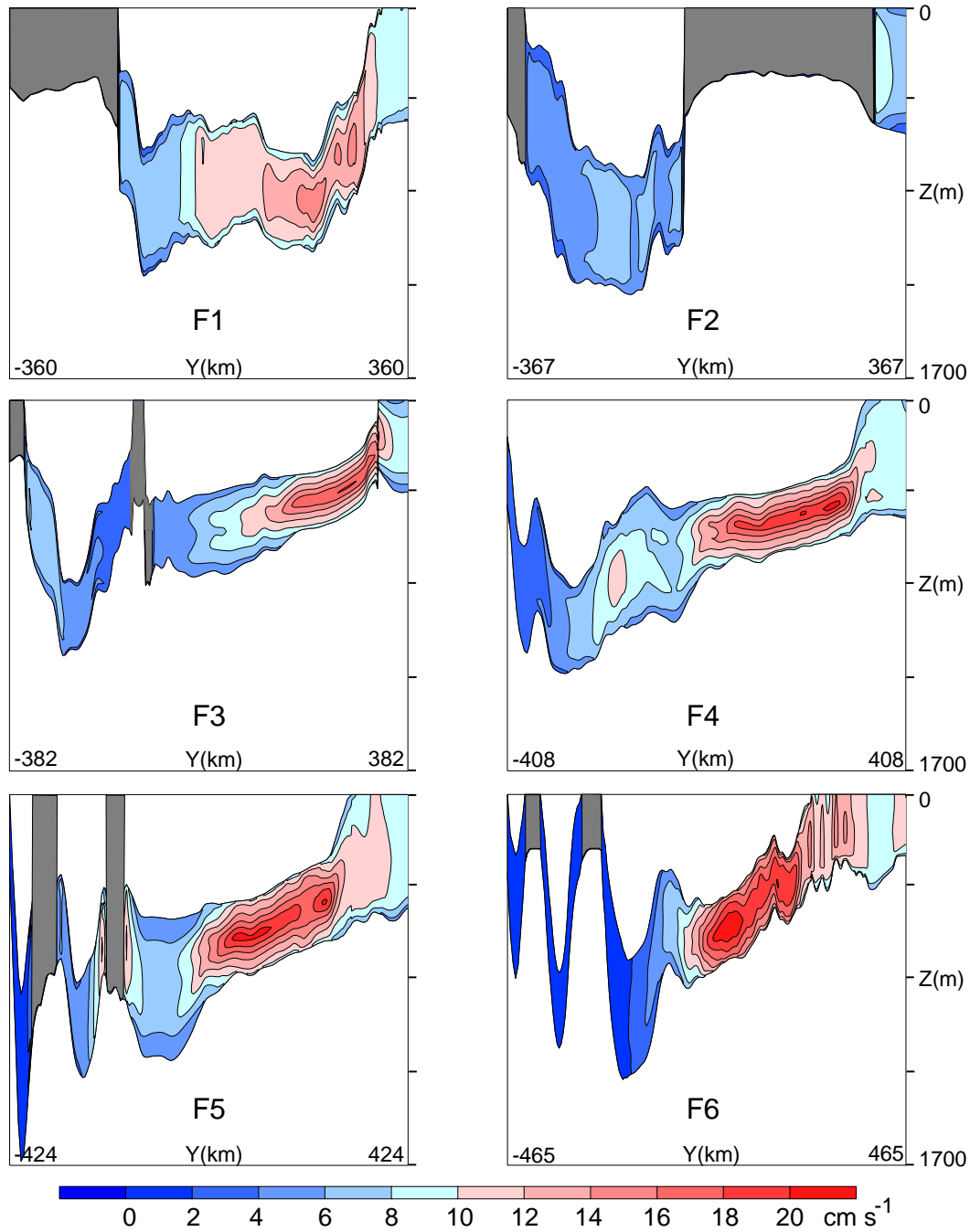


Figure 4.23: Major axis of the M_2 tidal ellipse (cm s^{-1}) considering summer stratification across vertical slices (y - z , Fig. 4.12) beneath Filchner-Ronne Ice Shelf.

In Fig. 4.25b, the modeled and observed circular components correspond to tidal currents observed at site S3. To avoid misleading comparison due to discrepancies between water column thickness in the model and at the observational site (see Fig. 4.24), the instrument depth was shifted 59 m upward in the water column. In this way, the comparison is made for currents 85 m above the bottom, keeping, then, the observational depth. Agreement between

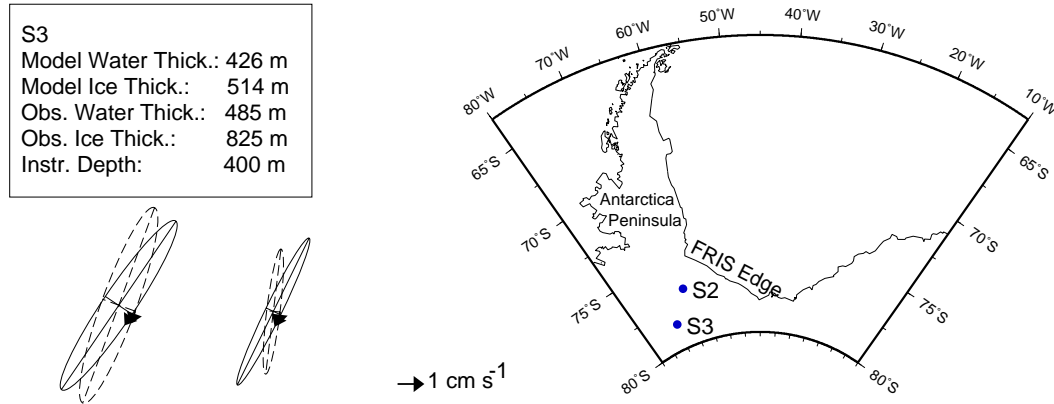


Figure 4.24: Comparison between modeled (dashed line) and observed (solid line) M_2 (left) and S_2 (right) tidal ellipses at site S3 beneath Filchner-Ronne Ice Shelf. In the map, positions and station names are indicated.

modeled and observed circular components is found. Due to the proximity of the M_2 critical latitude ($\approx 4^\circ$ northward), the thickness of the boundary layers of the counterclockwise circular component (Fig. 4.25b, dashed line) is larger than of the clockwise component (Fig. 4.25b, solid line).

Frictional stress at the seabed and at the ice shelf base influences the vertical structure of tidal currents, creating two boundary layers. Outside these boundary layers a free stream region exists with no shear and velocities almost independent of depth [Furevik and Foldvik, 1996; Makinson, 2001]. For thick water columns, tidal currents are weak and the frictional boundary layers occupy a small fraction of the water column (Fig. 4.25a). However, in shallow water with strong tidal currents, these layers can occupy the entire water column dominating the tidal current structure (Fig. 4.25c) [Prinsenbergh and Bennett, 1989]. In the results presented here, the effect of the critical latitude is included which magnifies the effect of the water column thickness.

Tidally induced melting at the ice shelf base can be estimated from the polarization of the tidal flow. Scheduikat and Olbers [1991] developed two one-dimensional mixed layer models without rotation, thermodynamically coupled to an ice shelf, one with two layers and one with three layers. They found that basal melting or freezing was less dependent on the intensity of the tidal current than on the ratio of the minor and major axes of the tidal current ellipse (polarization):

$$P = \pm \frac{V}{U}$$

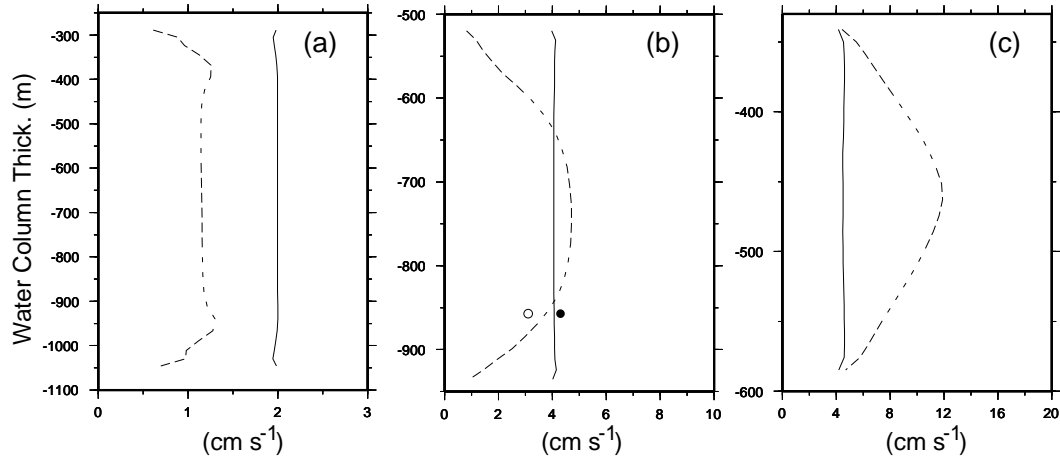


Figure 4.25: Vertical profiles of the magnitude of the two circular components of the decomposed M_2 tidal currents at three different points beneath FRIS, demonstrating the decrease of the free stream region from deep (a) to shallow (c) areas. The vertical profiles plotted in (b) are close to site S3 (Fig. 4.24). Dashed lines and not-filled symbols indicate counterclockwise and solid lines and filled symbols clockwise rotation.

where V and U are the semi-minor and the semi-major axes of the tidal current ellipse, respectively. The polarization ranges from a purely circular clockwise current ($P = -1$), through a flat or degenerated ellipse ($P = 0$), to a purely circular anticlockwise current ($P = +1$). For isotropic tidal currents ($P = \pm 1$), small amount of freezing occurs because the bottom boundary is decoupled from the upper layers of the water column, i.e., the behavior of the upper boundary layer is independent of the structure of the ocean below. However, if tidal currents are anisotropic ($P \neq \pm 1$), alternating entrainment and detrainment situations occur near the ice shelf base, producing high melt rates. In this case, the upper water column is connected to the lower boundary during a tidal cycle.

As already shown in Chapter 3, barotropic tidal ellipses are mainly anisotropic beneath FRIS with the polarization of the M_2 tidal ellipse at the base of the ice shelf being mainly

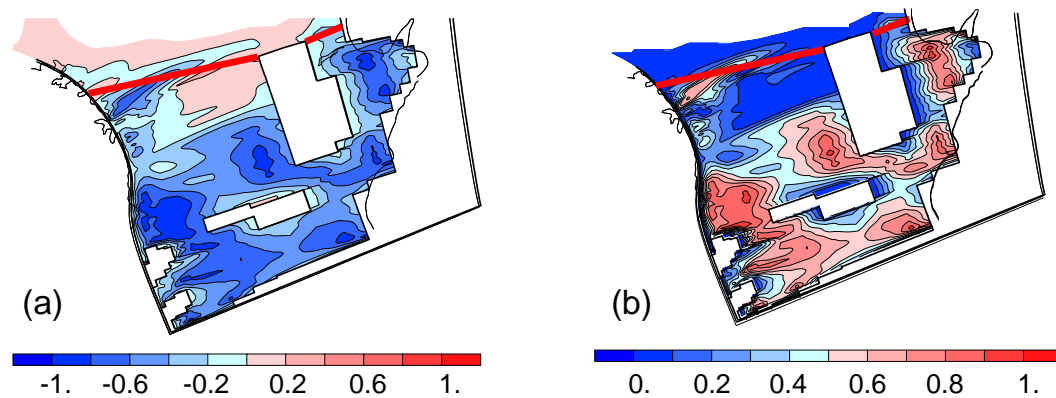


Figure 4.26: Polarization of M_2 tidal ellipses (a) and its absolute value (b) at the base of the Filchner-Ronne Ice Shelf. The red line indicates the approximate ice shelf edge.

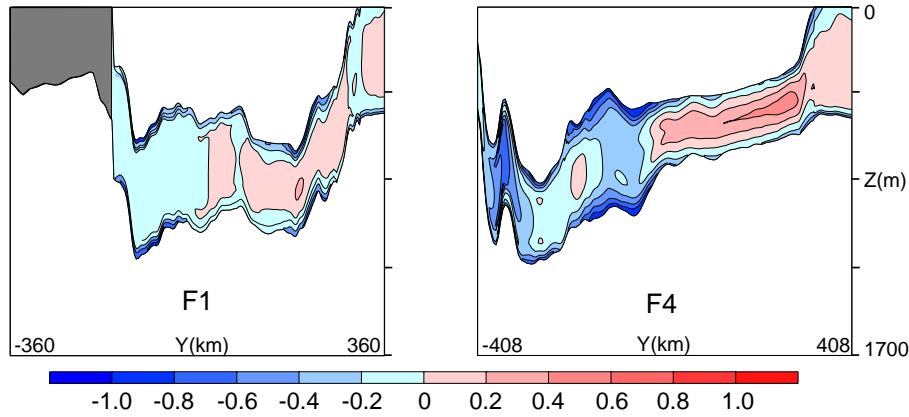


Figure 4.27: Polarization of M_2 tidal ellipses along two y-z slices (see Fig. 4.22) beneath Filchner-Ronne Ice Shelf.

negative (Fig. 4.26). A similar horizontal distribution of polarization was obtained with a two-dimensional barotropic tidal model applied to this region [Makinson, 2001]. Especially at the ice shelf front and near Henry Ice Rise, the polarization tends to zero (Fig. 4.26b), indicating, according to the theory, regions of high melting. Observations [Jenkins and Doake, 1991; Grosfeld *et al.*, 1992] and previous modeling studies [Makinson and Nicholls, 1999; Gerdes *et al.*, 1999] agree with these results.

Although most of the ice shelf base presents $P \rightarrow -1$ (Fig. 4.26a), it is clear from Fig. 4.27 that the polarization varies significantly within the water column and for different cavity locations. Along F1, for example, $P \rightarrow -1$ only near the upper and lower boundaries, with $P \rightarrow 0$ for almost the whole water column (Fig. 4.27). These results indicate large horizontal and vertical variations of the tidal ellipses polarization beneath FRIS.

Similar to the interaction between the upper boundary layer and the ocean below, if tidal currents are constant in time ($P = \pm 1$), there is no connection between the bottom boundary layer and the intermediate layer above which, thus, serves as a heat and salt-reservoir for the upper boundary layer [Scheduikat and Olbers, 1991]. If tidal currents are highly variable in time, the bottom boundary layer is connected with the upper levels of the water column. These results hold for thick water columns in the cavity but might be different for shallow areas where turbulent layers (at the ice shelf base and at the bottom) are directly connected (Fig. 4.25c).

4.8 Baroclinic Tides at the S_2 Frequency

In comparison to the M_2 results presented in the previous section, the results for S_2 are interesting because its critical latitude is at $85^\circ 45' 54''$ S, i.e., the critical latitude is south of the model domain (see Fig. 4.7). Therefore, the related resonance process on the shelf and at the shelf break, causing a thick bottom boundary layer and a depth-dependent vertical velocity profile, like for M_2 , and the critical latitude singularity for the propagation of Poincaré internal tides does not occur.

4.8.1 S_2 tidal currents on the continental shelf and at the shelf break

The major axes of the S_2 tidal ellipses are plotted in Fig. 4.28 for summer stratification, but very similar results are found also for winter stratification. On the shelf, typical major axis values are of the order of 3 cm s^{-1} . The major axis magnitude increases from 4 cm s^{-1} at the shelf break to 7 to 8 cm s^{-1} at the ice shelf edge.

The comparison between modeled and observed S_2 tidal ellipses at the FRIS edge (Fig. 4.17) shows good agreement, although a difference of approximately 10° exists between their orientations to the north. However, as already discussed for M_2 , such difference may not affect significantly the results and are considered to be small.

In general, S_2 major axes are more barotropic at the shelf break and slope than those for M_2 . The vertical profile of the major-axis is almost constant for the whole water column, except for the near bottom region due to bottom frictional effects. As discussed in Section 4.5, the slope is subcritical for S_2 . Therefore, internal tides are not expected which explains the barotropic character of the tidal currents at the shelf break and slope.

Near the ice shelf edge, a first mode internal tide is generated with velocities of 3 cm s^{-1} (slice 3, Fig. 4.28) which cannot be explained by the linear theory. The S_2 internal tide was not generated in simulations where the ice shelf was excluded from the model domain (not shown). Therefore, it must be caused by the steep topographic change produced by the ice shelf. The generated internal tide propagates along the ice shelf edge.

The spatial distribution of the internal vertical displacements due to S_2 (not shown) is quite similar to that for the M_2 frequency, but magnitudes are reduced by a factor of 3 due to weaker vertical velocities.

The modeled and observed magnitude values of the two counterrotating circular compo-

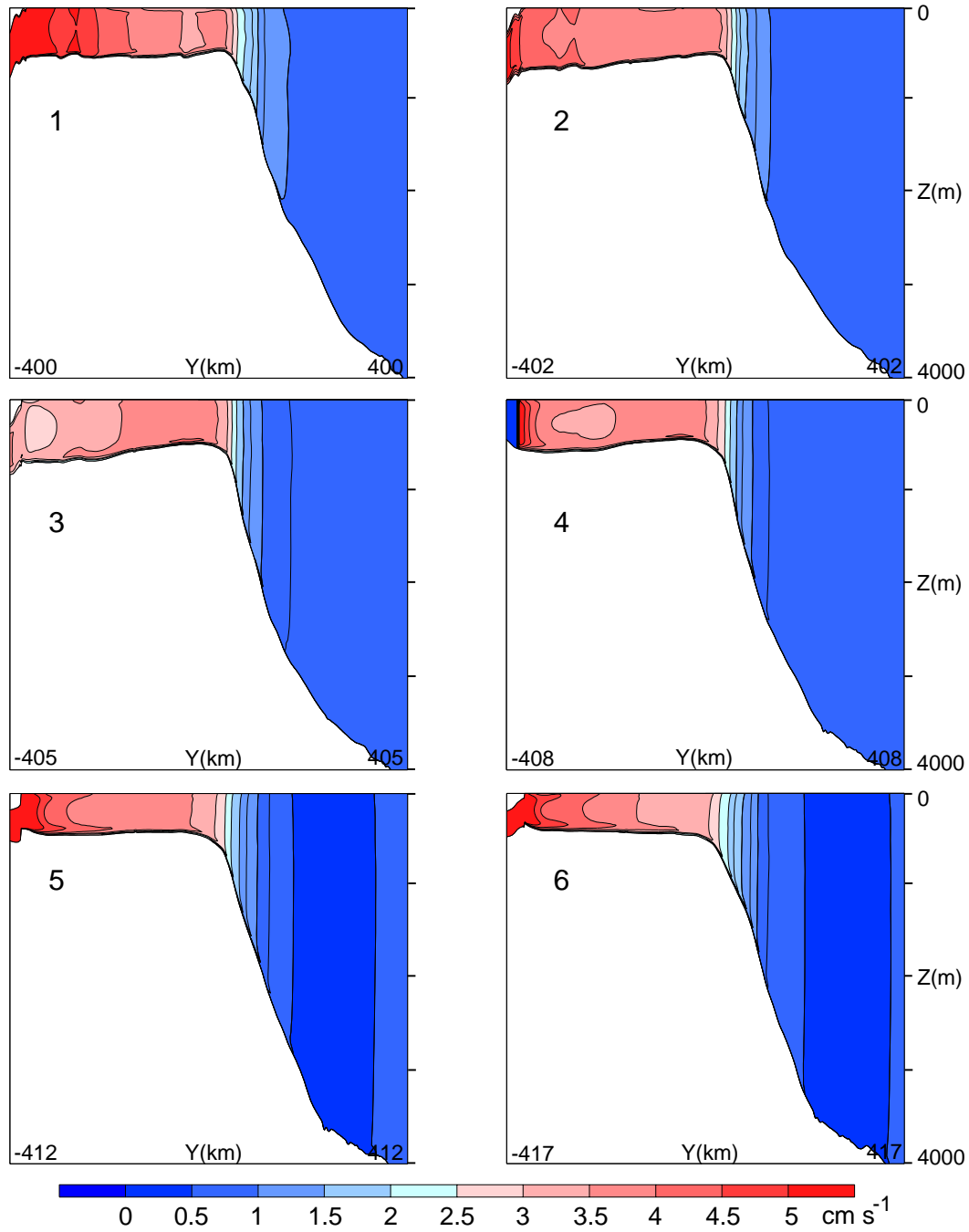


Figure 4.28: Major axis of the S_2 tidal ellipse (cm s^{-1}) considering summer stratification across vertical slices (y-z, Fig. 4.12) in the southern Weddell Sea.

nents of the S_2 tidal current agree relatively well (Fig. 4.29). Only in Fig. 4.29c, the modeled amplitude of the counterclockwise component does not match the observed value. Since the difference is approximately 1 cm s^{-1} , it is considered as insignificant. The comparison between Fig. 4.20 and 4.29 shows that the thickness of the bottom boundary layer at the shelf break (e.g., (f)) is thinner for S_2 (reaching a maximum of 50 m above the bottom) than for M_2 ,

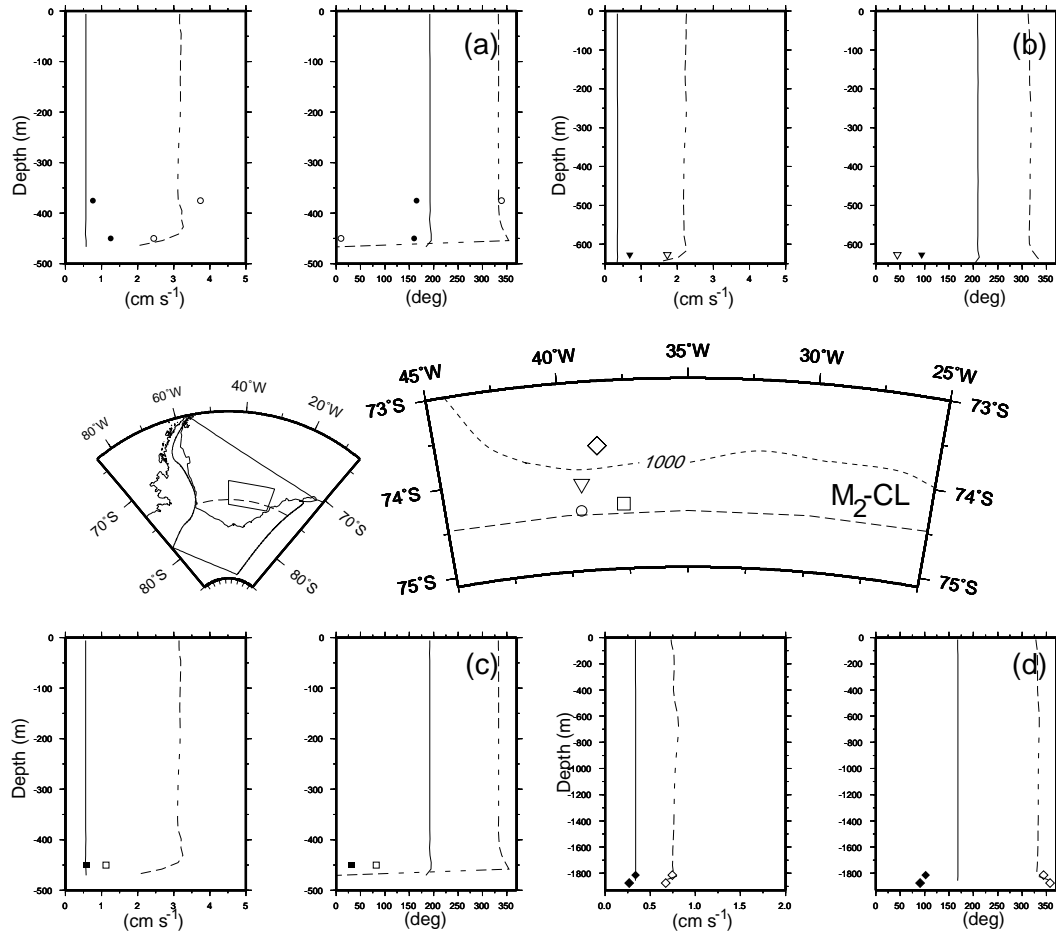


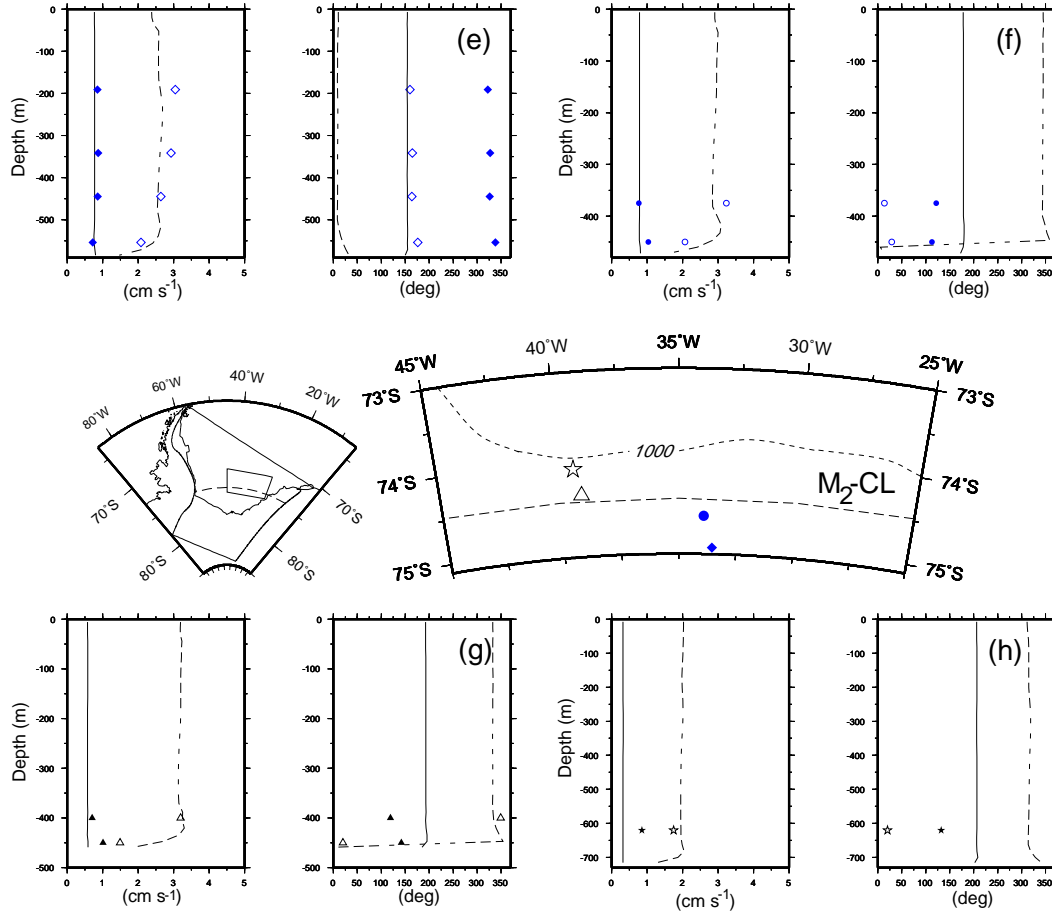
Figure 4.29: Comparison between modeled (solid and dashed lines) and observed (symbols) S_2 decomposed tidal ellipses in the shelf break region. Dashed line and not-filled symbols indicate counterclockwise and solid line and filled symbols clockwise rotation. Each symbol corresponds to a different observation site that is indicated in the map. For each comparison, amplitude (left, cm s^{-1}) and phase (right, degrees) of the counter- and clockwise components are plotted. Dashed and dot lines in the map refer to the M_2 critical latitude and to the 1000 m isobath, respectively.

as it was expected. Greater discrepancies (about 100°) are found for the phases and the same explanations given for phases differences at M_2 frequency (Subsection 4.7.1) are valid for here.

Like for M_2 , but not as intensified, a wave trapped to the pycnocline develops (see slice 1, Fig. 4.28 and Fig. 4.29e) increasing the shear near the surface.

4.8.2 S_2 tidal currents beneath Filchner-Ronne Ice Shelf

Under FRIS, the magnitude of the S_2 major axes (Fig. 4.30) are $\approx 48\%$ less than for M_2 . Similar characteristics between M_2 and S_2 are found for regions of stronger (northern and western portions of the cavity) and weaker (southern part) currents. The maximum S_2 major axis of the tidal ellipse is approximately 14 cm s^{-1} at the northwestern corner close to the Antarctica Peninsula (Fig. 4.30, slice F6).



Cont. Fig 4.29.

Comparison between modeled and observed tidal ellipses at site S3 (Fig. 4.24, right column) shows that, despite an underestimation of modeled S_2 major axis ($23\% = 1.4 \text{ cm s}^{-1}$) and the difference between modeled and observed inclination angles, the eccentricity and the sense of rotation both are well represented by the model. At site S2 (Fig. 4.24), the major axis estimated from the thermistor cable displacement [Makinson and Nicholls, 1996] is 13.3 cm s^{-1} while the modeled is 10.5 cm s^{-1} in the middle of the water column. The same considerations about the reasons for such discrepancy as discussed in Subsection 4.7.2, are applied here.

S_2 tidal ellipses were decomposed into the two counterrotating circular velocity components for the same three points shown in Fig. 4.25 (Fig. 4.31). The difference between modeled and observed S_2 major axes at site S3, already presented in Fig. 4.24 exists in the vertical profile of the magnitude of both circular components (Fig. 4.31b). Compared to Fig. 4.25b, the free stream region for S_2 's counterclockwise component (dashed line) is clearly increased, leading to thinner boundary layers. This site is located around 4° south of the M_2 -CL and around 8° north of the S_2 -CL. Since the site is closer to the M_2 -CL, its effect upon M_2 tidal

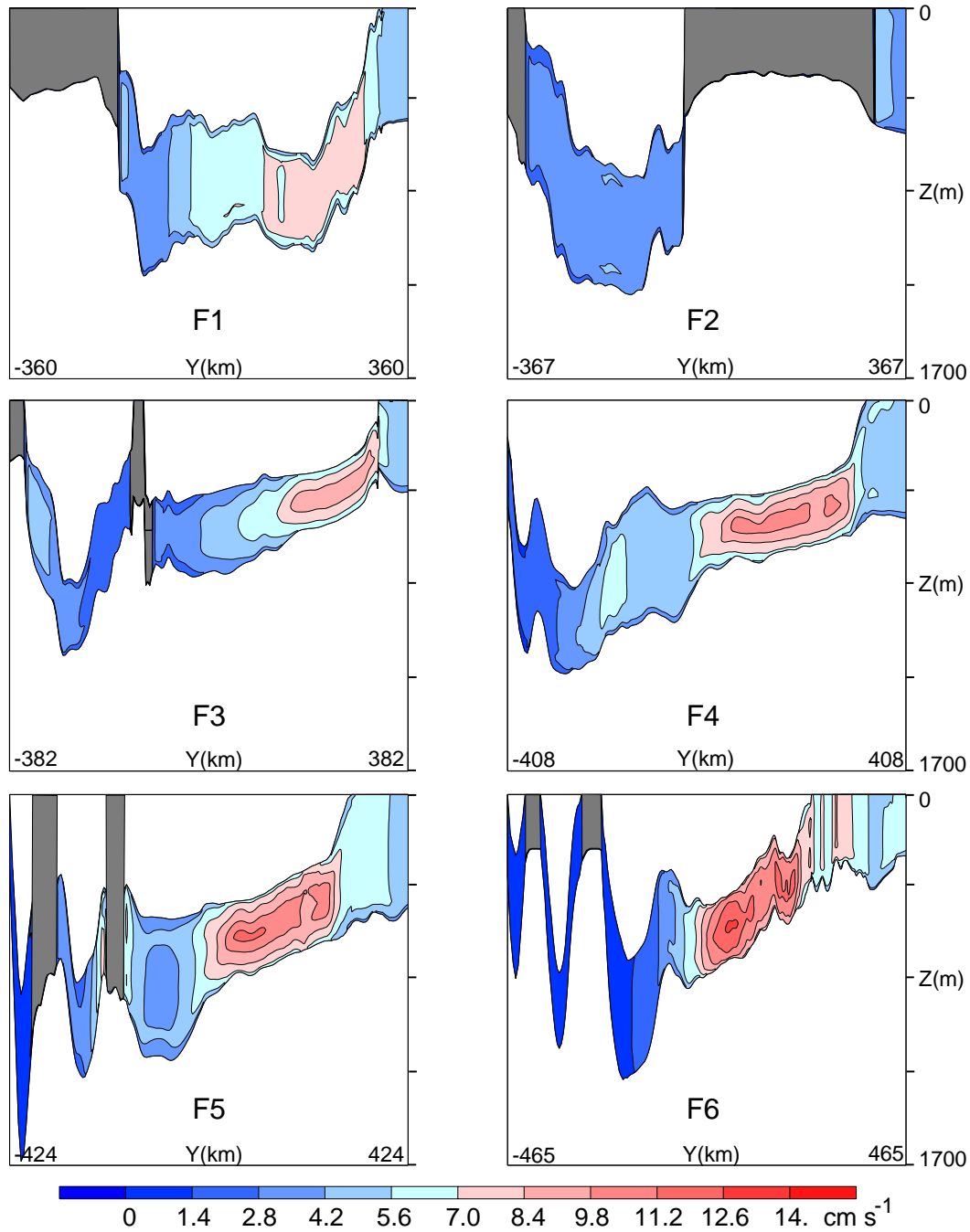


Figure 4.30: Major axis of the S_2 tidal ellipse (cm s^{-1}) considering summer stratification across vertical slices (y-z, Fig. 4.12) beneath Filchner-Ronne Ice Shelf.

currents is more evident than the effect of the S_2 -CL on S_2 tidal currents.

The other two vertical profiles (Fig. 4.31a, c) show the effect of the water column thickness on the vertical extent of the boundary layers. For regions with a thick water column, the free stream area occupies almost the whole column (c) while for thinner columns, it almost does not exist due to frictional effects of the boundary layers (a).

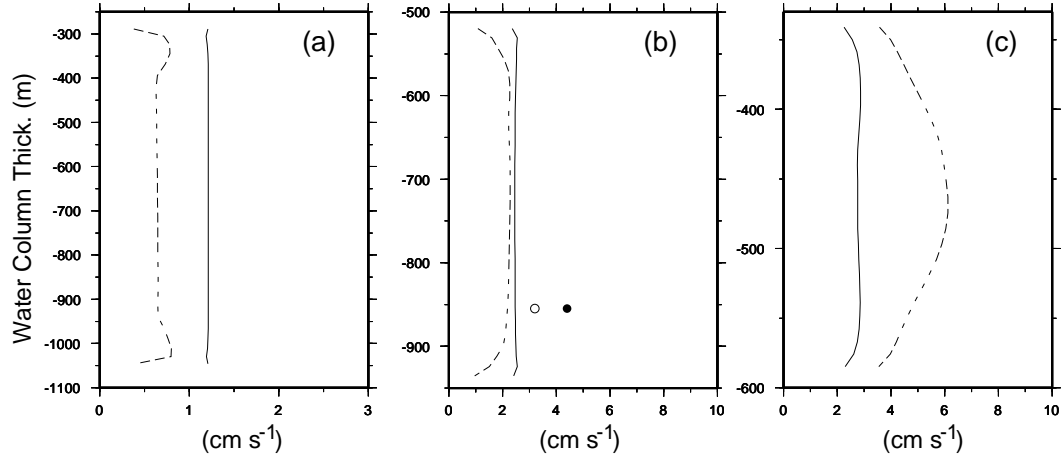


Figure 4.31: Vertical profiles of the magnitude of the two components of the decomposed S_2 tidal currents at three different points beneath FRIS, demonstrating the decrease of the free stream region from deep (a) to shallow (c) areas. The vertical profiles plotted in (b) are close to site S3 (Fig. 4.24). Dashed lines and not-filled symbols indicate counterclockwise and solid lines and filled symbols clockwise rotation.

The polarization of the S_2 tidal ellipses at the base of FRIS (Fig. 4.32a) is very similar to the M_2 results (Fig. 4.26a). Near the ice shelf edge and north of Henry Ice Rise $P \rightarrow 0$ (Fig. 4.32b), indicating a region of high melt rates, while far away from these regions $P \rightarrow -1$, indicative for freezing. The vertical variation of the polarization of the S_2 tidal ellipse is also high (Fig. 4.33).

4.9 Baroclinic Residual Currents

The representation of baroclinic residual currents in this model configuration is not expected to be very realistic. According to equation 3.4, tidal currents with diurnal period will produce stronger residual flow than with semidiurnal period ($E = V_{tidal} * \omega_{tidal}$). Since diurnal periods

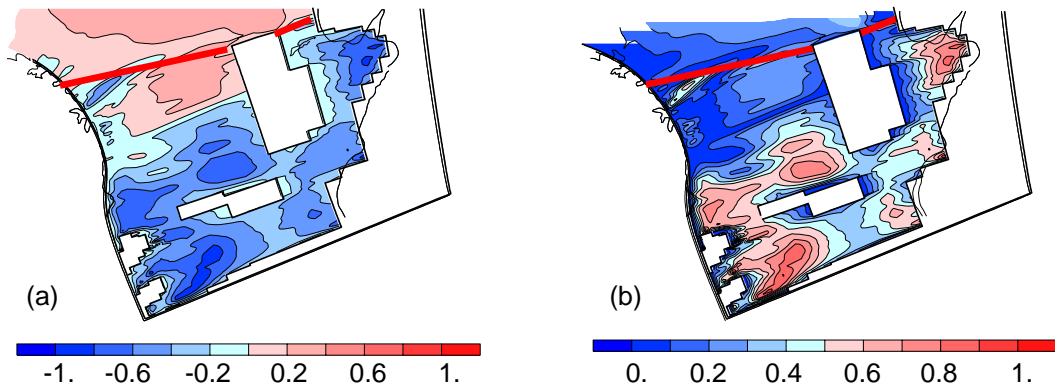


Figure 4.32: Polarization of S_2 tidal ellipses (a) and its absolute value (b) at the base of the Filchner-Ronne Ice Shelf. The Red lines indicates the approximate ice shelf edge.

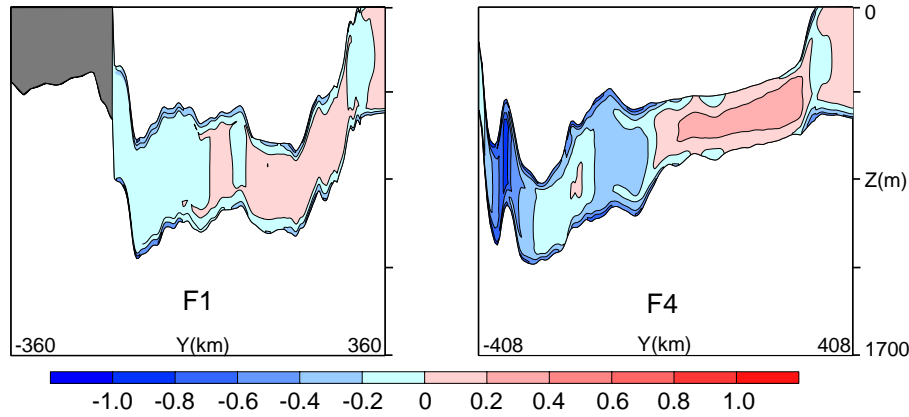


Figure 4.33: Polarization of S_2 tidal ellipses along two y-z slices beneath Filchner-Ronne Ice Shelf

are not considered in the 3D-model simulations, their contribution to the baroclinic residual flow is not included and, therefore, will cause an underestimation of the flow. The coarser zonal grid resolution will also contribute to lower values for the time-independent currents as it was discussed in Section 3.5. On the other hand, because stratification is included, it is interesting to compare these results with the theory of baroclinic residual flows [Maas and Zimmerman, 1989b; Pérenne *et al.*, 2000]. The baroclinic residual currents are similar for summer and winter stratifications.

Because the baroclinic residual flow in the deeper Weddell Sea was not strong due to the weak barotropic tidal currents (Subsection 3.4.2), Fig. 4.34 focuses in the FRIS cavity. Small differences were found between the residual flow at the bottom (Fig. 4.34a) and at 400 m (Fig. 4.34b). In general, the bottom baroclinic residual currents are only a few millimeters per second stronger than the currents at mid-depth due to the interaction with bottom topography; there is no evident change in the direction of the currents from 400 m to the bottom. All small scale details of the barotropic residual flow computed with BRIOS4.3 (Section 3.5) are lost here, due to the coarser east-west resolution, leading to a smoother topography in this direction. At the FRIS edge, maxima residual currents were about $2\text{--}3\text{ cm s}^{-1}$ to the west. Near Filchner ice front, a strong baroclinic residual flow ($\approx 4\text{ cm s}^{-1}$) develops. Because of the Filchner Trough and the coarser zonal resolution, a steep gradient in bottom topography exists in that area of the model domain. Its interaction with the barotropic flow may result in the modeled high values of baroclinic residual currents.

It was demonstrated analytically by Maas and Zimmerman [1989b] and numerically by Pérenne *et al.* [2000] that the main effect of the density stratification is an intensification of

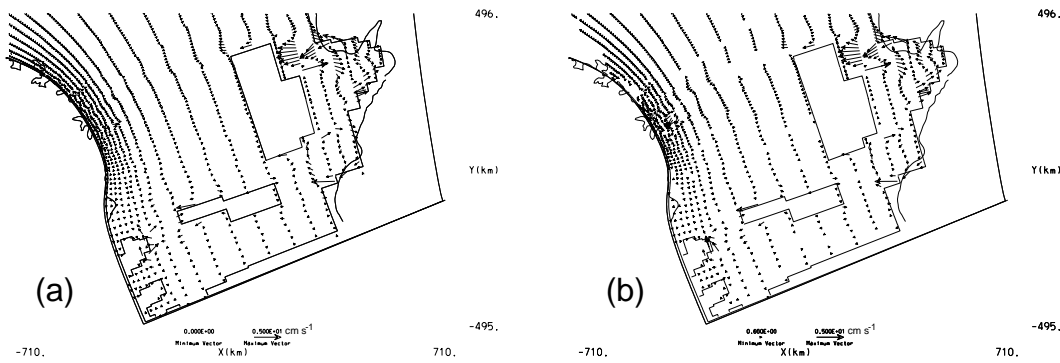


Figure 4.34: Baroclinic residual flows (cm s^{-1}) beneath FRIS (a) near the seabed and (b) at 400 m.

the residual flow in the lower water column, thereby diminishing the surface residual flow but without changing the vertical mean.

Fig. 4.35a shows the baroclinic residual flow in a vertical plane across the shelf break and the difference between summer and winter residual flow is plotted in Fig. 4.35b. Since the pycnocline isolates the upper layer from topographic effects, no strong residual flow is generated (Fig. 4.35a) [Pérenne *et al.*, 2000]. During winter, because the strong pycnocline disappears, a slight maximum of the near surface baroclinic residual flow exists (continental shelf and shelf break regions of Fig. 4.35b). In the lower water column, there is basically no difference between summer and winter residual flows. The wave trapped at the pycnocline does not produce a strong residual flow, as expected from its symmetric tidal cycle (Fig. 4.21). Although stratification beneath FRIS is less influenced by seasons than on the continental shelf,

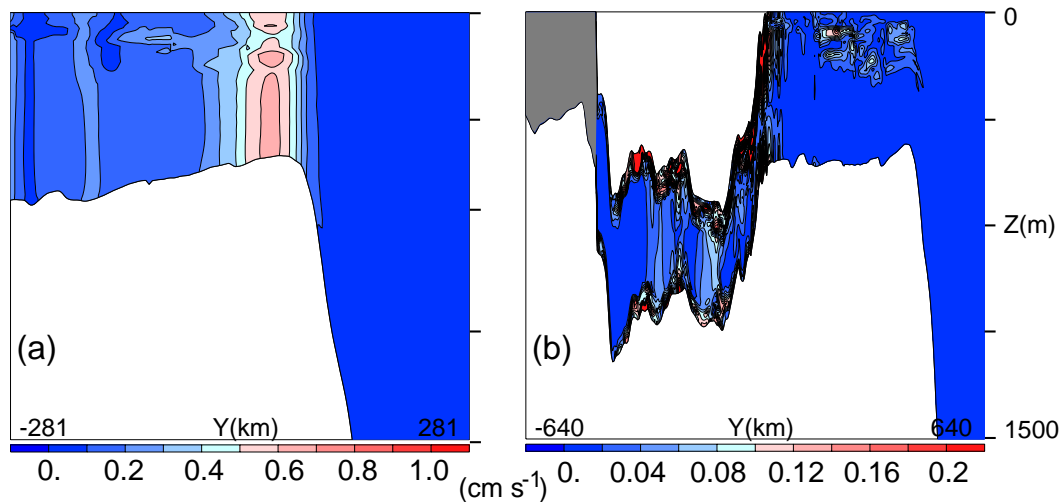


Figure 4.35: (a) Baroclinic residual flow (cm s^{-1}) and (b) the difference (cm s^{-1}) between residual flows computed using winter and summer stratification in a y - z slice across the southern Weddell Sea. If residual flows computed with winter stratification are greater than that computed with summer, this difference is positive.

winter and summer residual flows shows some difference. Probably small changes in the mean flow outside the cavity will influence the residual flow beneath FRIS.

4.10 Summary

With a grid spacing of approximately 2 km in the cross-slope direction, internal tides are successfully represented by the numerical model (Section 4.2). Due to limitations in computational resources, it was not possible to use a grid as fine in the along-slope direction. For this reason, the focus of this chapter was on the southern Weddell Sea which is the most probable region for internal wave generation. Although along-shore topographic variations may generate internal tides as well, these would contribute an order of magnitude less than the cross-slope variations (Section 4.5).

In the southern Weddell Sea, the significant difference between summer and winter stratification is only in the upper water column (Section 4.4). For this reason, the stratifications produce similar patterns and magnitudes of the vertical and horizontal tidal currents. Their differences related to the density field are limited to the near surface. Although observations of semidiurnal tidal currents 100 m above the bottom at the southern Weddell Sea shelf break [Foldvik *et al.*, 1990] show a general trend to have minima in austral summer and maxima in austral winter, the difference between them is less than 2 cm s^{-1} with only some variability.

In the case of the M_2 frequency, an internal tide was generated in the middle of the slope in the eastern Weddell Sea (Section 4.7.1). It was characterized by weak velocities ($\approx 1 \text{ cm s}^{-1}$) and propagated along the slope. The linear theory of generation and propagation of internal tides (Section 4.1) was used to interpret the model results which were largely consistent with the theory. M_2 major axes are small in the deep ocean increasing towards the continental shelf and shelf break ($\approx 7 \text{ cm s}^{-1}$) and further towards the ice shelf edge with ≈ 10 to 14 cm s^{-1} in the mid-water column. Due to the proximity of the M_2 critical latitude, the current profile is depth-dependent, leading to a bottom boundary up to 100 m thick.

Beneath the Filchner-Ronne Ice Shelf, the M_2 major axis reaches up to 20 cm s^{-1} in shallow areas (northern cavity), decreasing to $4\text{--}6 \text{ cm s}^{-1}$ in deeper regions (southern cavity). Due to frictional effects at the ice shelf base and seabed, the strongest velocities were found in the middle of the water column. The polarization of the tidal ellipses, important to characterize melting and freezing regimes, showed large spatial variability. S_2 tidal currents had basically

the same characteristics as the M_2 , but were reduced by a factor of approximately 2.5-3.

Near the ice shelf edge, an S_2 internal tide was generated with velocities of 3 cm s^{-1} . In this case, the linear theory was not able to explain it. Model simulations suggest that the steep topographic change at the ice shelf edge is the main reason for the disagreement between theory and model results.

Although the baroclinic residual flow generated by the main semidiurnal tidal constituents was underestimated, because the diurnal constituents were not considered, the model results showed good agreement with the theory of residual flows when density stratification is included, showing good agreement. The effect of the strong summer pycnocline is to reduce the surface residual flow and to increase it in the lower water column.

The good agreement between the model results and observations show that the BRIOS tidal model is a valuable tool to investigate tides and tidal currents.

Chapter 5

Tidally Induced Mixing in the Southern Weddell Sea

Based on the results presented in the previous chapter, the tidally induced vertical mixing in the inner Weddell Sea will be quantified. Seasonal variations in the mixing rates, as well as the effect of the inclusion of 8 tidal constituents in the open boundary forcing, and the impact of the use of a cross-slice (y-z) grid domain to compute mixing quantities will be investigated. Since both vertical coefficients (viscosity and diffusivity) are similar in magnitude and spatial distribution (see Appendix C), only results for the vertical eddy viscosity coefficient (AK_v) will be presented. The mean AK_v is presented as the time-mean of a 20-day time-series; thus, the mean-value contains the contribution of the residual flow and of all tidal constituents which were used to force the model.

5.1 Computation with M_2 and S_2 Tidal Constituents

Fig. 5.1 and 5.2 show the vertical eddy viscosity coefficients obtained for summer and winter stratification. For both seasons, maximum values of AK_v at the internal tide generation sites are $6 \times 10^{-4} \text{ m}^2 \text{ s}^{-1}$, a significant increase compared to the canonical values, which range between 1×10^{-5} [Polzin *et al.*, 1997; Webb and Sugimotohara, 2001] and $1 \times 10^{-4} \text{ m}^2 \text{ s}^{-1}$ for abyssal plains [Munk and Wunsch, 1998]. Because the turbulence maxima occur near the shelf break and on the continental shelf, the focus will be on the upper slope and shelf regions (depth range 400-2500 m) (Fig. 5.1 and 5.2).

Although the M_2 and S_2 major axes of the tidal ellipse for summer and winter (Section 4.7

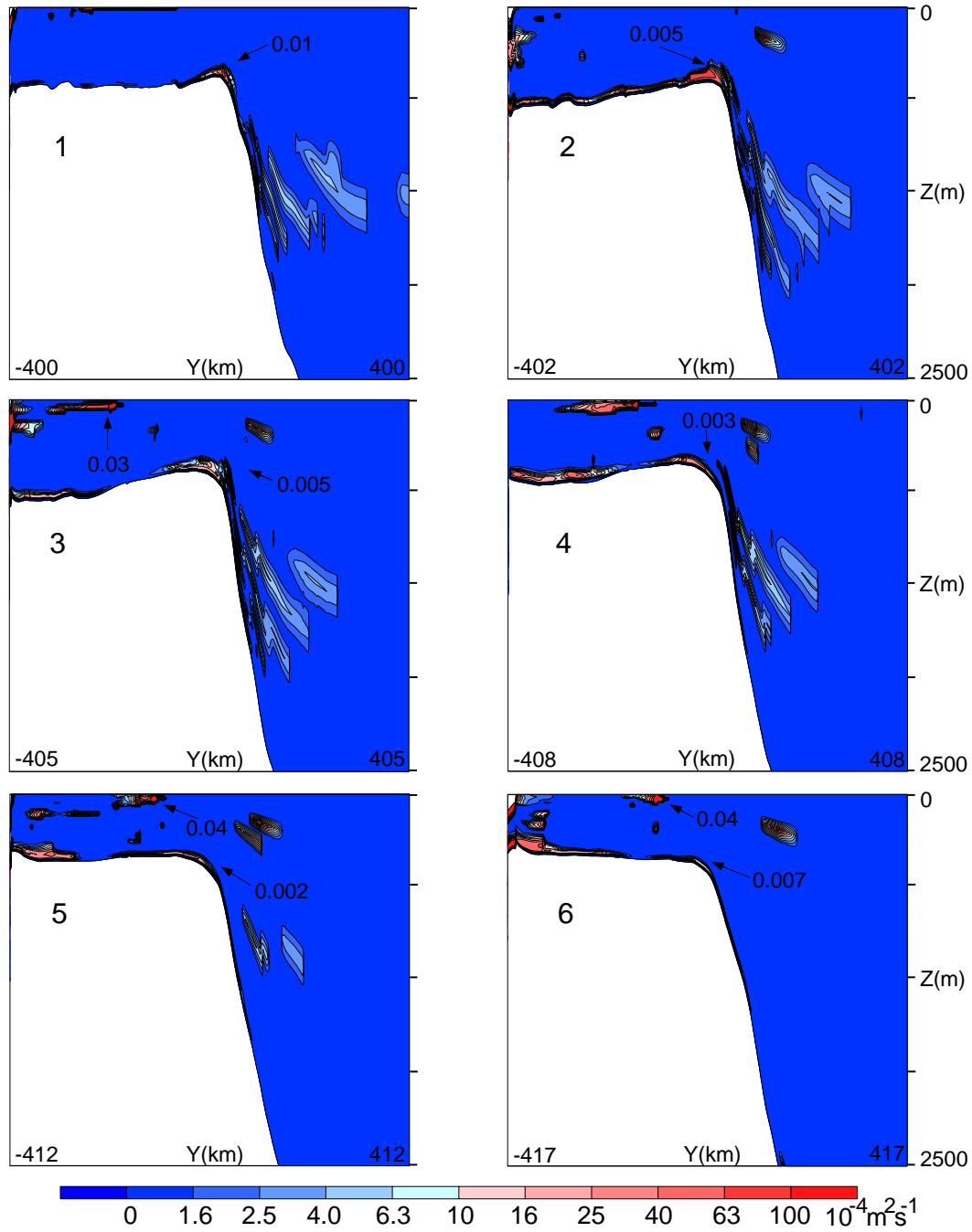


Figure 5.1: Summer mean (20 days) eddy viscosity coefficients ($\text{m}^2 \text{s}^{-1}$) at the shelf break region of the southern Weddell Sea, considering M_2 and S_2 forcing at the northern boundary for the slices (1-6) indicated in Fig. 4.12. Abrupt changes in the contour interval are due to the fine resolution employed.

and 4.8) are similar, the eddy viscosity values and the spatial distributions for both seasons are different. During summer (Fig. 5.1), high values of AK_v are found at the shelf break ($1 \times 10^{-2} \text{ m}^2 \text{s}^{-1}$, slice 1) and near the surface ($3 \times 10^{-2} \text{ m}^2 \text{s}^{-1}$, slice 3 and 4). In the pycnocline, turbulence is enhanced due to the trapped wave which produces shear in the water column. At the shelf break, the increased thickness of the bottom boundary layer spreads turbulent mixing

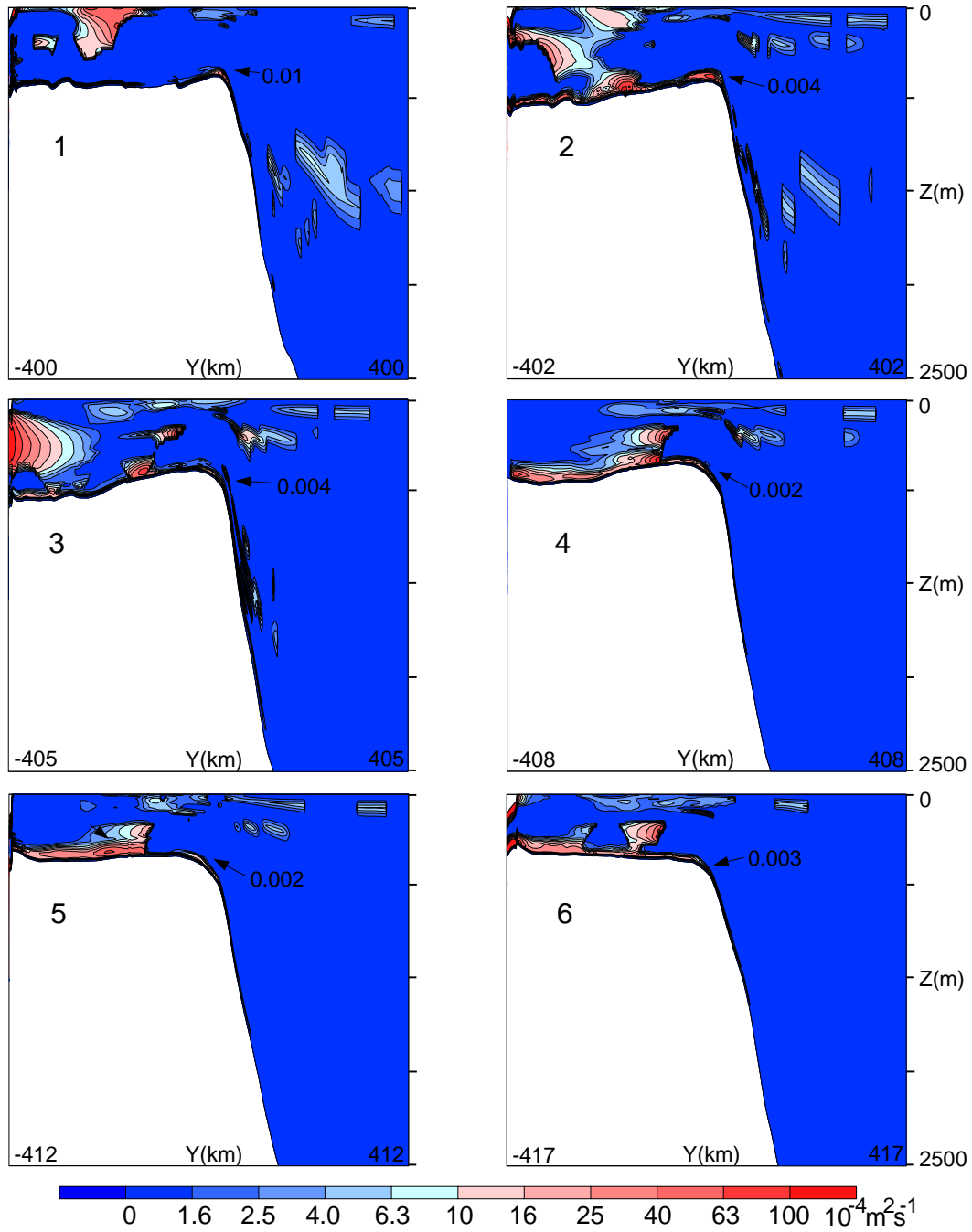


Figure 5.2: Winter mean (20 days) eddy viscosity coefficients ($\text{m}^2 \text{s}^{-1}$) at the shelf break region of the southern Weddell Sea, considering M_2 and S_2 forcing at the northern boundary for the slices (1-6) indicated in Fig. 4.12. Abrupt changes in the contour interval are due to the fine resolution employed.

to a larger part of the water column. High values of AK_v are also observed at the ice shelf edge.

During winter, the upper ocean turbulence is not so strong (Fig. 5.2, slices 3 to 6) and turbulent mixing exists throughout the water column on the shelf and near the shelf break (Fig. 5.2, slice 4) due to the low winter static stability in this region (see Fig. 4.8). The more

stable summer stratification suppresses turbulence in the main body of the water column which decreases very rapidly with height above the sea floor.

Low static stability is also responsible for the relatively high values of AK_v near the upper slope, found for both seasons. Comparing Fig. 5.1 and 5.2, slice 6 with Fig. 4.8b, d, it is evident that the moderate AK_v values are located where potential density lines are almost vertical (at the offshore boundary of the frontal system) or inclined in the shelf break direction.

For both seasons, tidally induced mixing has maxima values at the eastern Weddell Sea continental shelf break (e.g., Fig. 5.1, slice 1), decreasing westward, due to the position of the M_2 critical latitude. Enhanced mixing is also found near the bottom on the western Weddell Sea continental shelf (e.g., Fig. 5.1, slice 4). At that location, the critical latitude is exactly in the middle of the continental shelf (Figs. 4.12), increasing shear in the water column and, consequently, AK_v values. These results indicate a significant seasonal and spatial variability in the mixing quantities over the shelf, shelf break and upper continental slope.

Tidal currents are likely to be the principal source of energy for mixing beneath ice shelves [MacAyeal, 1984a]. The thick ice sheet prevents air-sea contact, isolating the sea beneath from direct atmospheric forcing. Frictional drag at the sea floor and ice shelf base produce vertical shear; the resultant turbulence causes vertical mixing throughout the water column.

Beneath FRIS during summer, the highest AK_v values ($\approx 1 \times 10^{-2} \text{ m}^2 \text{ s}^{-1}$) are generally in the northwestern cavity (Fig. 5.3, slices F4, F5 and F6). This is the region where tidal currents reach their maxima velocity (Fig. 4.23), leading to strong vertical shear due to frictional effects at the upper and lower boundaries. Near the Filchner Through (Fig. 5.3, slices F1), AK_v is reduced compared to the slices located to the west due to the thicker water column. In the southernmost portion of FRIS, maxima AK_v values are up to 50 times weaker than the shallower northern cavity (Fig. 5.3, slices F5) and vertical mixing is likely to play only a small role in modifying the water column structure [Makinson and Nicholls, 1999]. Compared to the shelf and shelf break regions, vertical mixing under FRIS is more enhanced. While at the shelf break maxima values of AK_v were around $1 \times 10^{-2} \text{ m}^2 \text{ s}^{-1}$ in specific areas, they can reach $5 \times 10^{-2} \text{ m}^2 \text{ s}^{-1}$ for large portions of the cavity.

In general, summer and winter vertical viscosity coefficients have similar spatial distribution and magnitude, but in isolated areas near the Ronne Ice Shelf front AK_v values were slightly higher ($\approx 5 \times 10^{-2} \text{ m}^2 \text{ s}^{-1}$) during winter than during summer. As described in Sec-

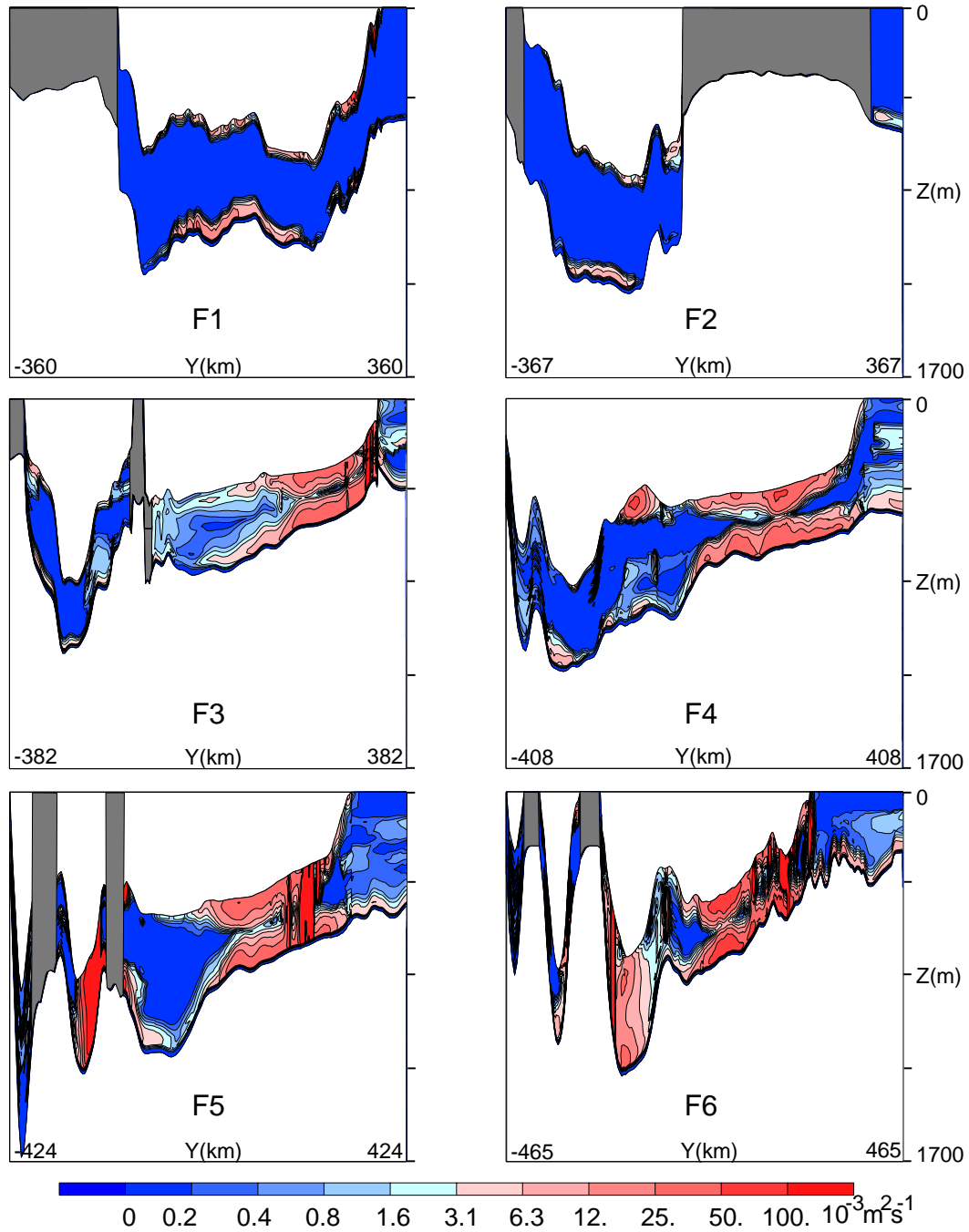


Figure 5.3: Summer mean (20 days) eddy viscosity coefficients ($\text{m}^2 \text{s}^{-1}$) beneath Filchner-Ronne Ice Shelf, considering M_2 and S_2 forcing at the northern boundary for the slices (F1-F6) indicated in Fig. 4.22.

tion 4.4, the ocean in the cavity is mainly isolated from seasonal changes, but the inflow of HSSW is reduced during summer since sea ice formation ceases in the coastal polynya [Nicholls, 1996]. This causes a decrease in the thickness of the HSSW layer in the cavity, leading to a change in depth where vertical shear (produced at the interface between ISW and HSSW) occurs. During winter, the interface between ISW and HSSW is closer of the ice shelf

base. Consequently, vertical shear between the two water masses, and between ISW and the ice shelf base are close, resulting an increase in AK_v values.

5.2 Combined Effects of Semidiurnal and Diurnal Tidal Constituents

The potential contribution of the eight main tidal constituents, semidiurnal and diurnal, (M_2 , S_2 , N_2 , K_2 , K_1 , O_1 , P_1 , Q_1) to the internal tide mixing is considered next. As discussed in the Subsection 3.3.1, most of the tidal energy at the southern Weddell Sea shelf break is at the K_1 frequency due to the existence of barotropic shelf waves [Middleton *et al.*, 1987]. The quantitative characteristics of these waves (wavelength, wavenumber, etc.) depend on the along-shelf topographic variations [Thomson and Crawford, 1982]. Thus, they will not be represented in the 3D-model with a high level of accuracy, since the grid resolution in the along-slope direction is coarse, but their generation process should be covered by the simulations. The forcing mechanism highly depends on the cross-slope bathymetry [Thomson and Crawford, 1982], which in turn is sufficiently resolved in the model. The summer density profile was used in order to avoid mixing produced by low static stability. Therefore, we retain only mixing caused by shear close to the bottom and pycnocline.

The mean vertical eddy viscosity for the forcing with all eight constituents is shown in Fig. 5.4. The spatial distribution of AK_v is similar to that computed with the two semidiurnal constituents (Fig. 5.1; note that Fig. 5.1 and Fig. 5.4 have different color scales). However, high values of AK_v extend to a larger portion of the water column and increased one order of magnitude at the shelf break ($1 \times 10^{-2} \text{ m}^2 \text{ s}^{-1}$, slice 1). Such magnification could be caused by the continental shelf waves of diurnal period, since their maximum amplitude is located above the upper slope close to the shelf break, attenuating very fast on both sides of the shelf break [Foldvik *et al.*, 1990].

In order to verify this hypothesis, the power spectral density (PSD) of a time series of AK_v was computed for points located near the shelf break of slices 1 and 6 (Fig. 5.5). The PSD describes how the power (or variance) of a time series is distributed with frequency. At slice 1 (Fig. 5.5, top), the major signal is related to the semidiurnal period followed by a broad diurnal band and higher frequencies (period of, e.g., $\approx 6.21 \text{ h}$). At slice 6 (Fig. 5.5, bottom), the semidiurnal frequency still dominates, but its aspect ratio with the diurnal period is reduced to 3 (at slice 1, it was ≈ 8). Due to the geographic configuration of the Weddell Sea, the

critical latitude is exactly located at the shelf break of slice 1, while at slice 6 its position is in the middle of the continental shelf (see Fig. 4.12). This implies that at the eastern side of the southern Weddell Sea, semidiurnal frequencies are most significant to generate turbulence at the shelf break. Trapped waves and higher frequencies will contribute to increase AK_v values. At the western side of the southern Weddell Sea, both frequencies (diurnal, semidiurnal, and

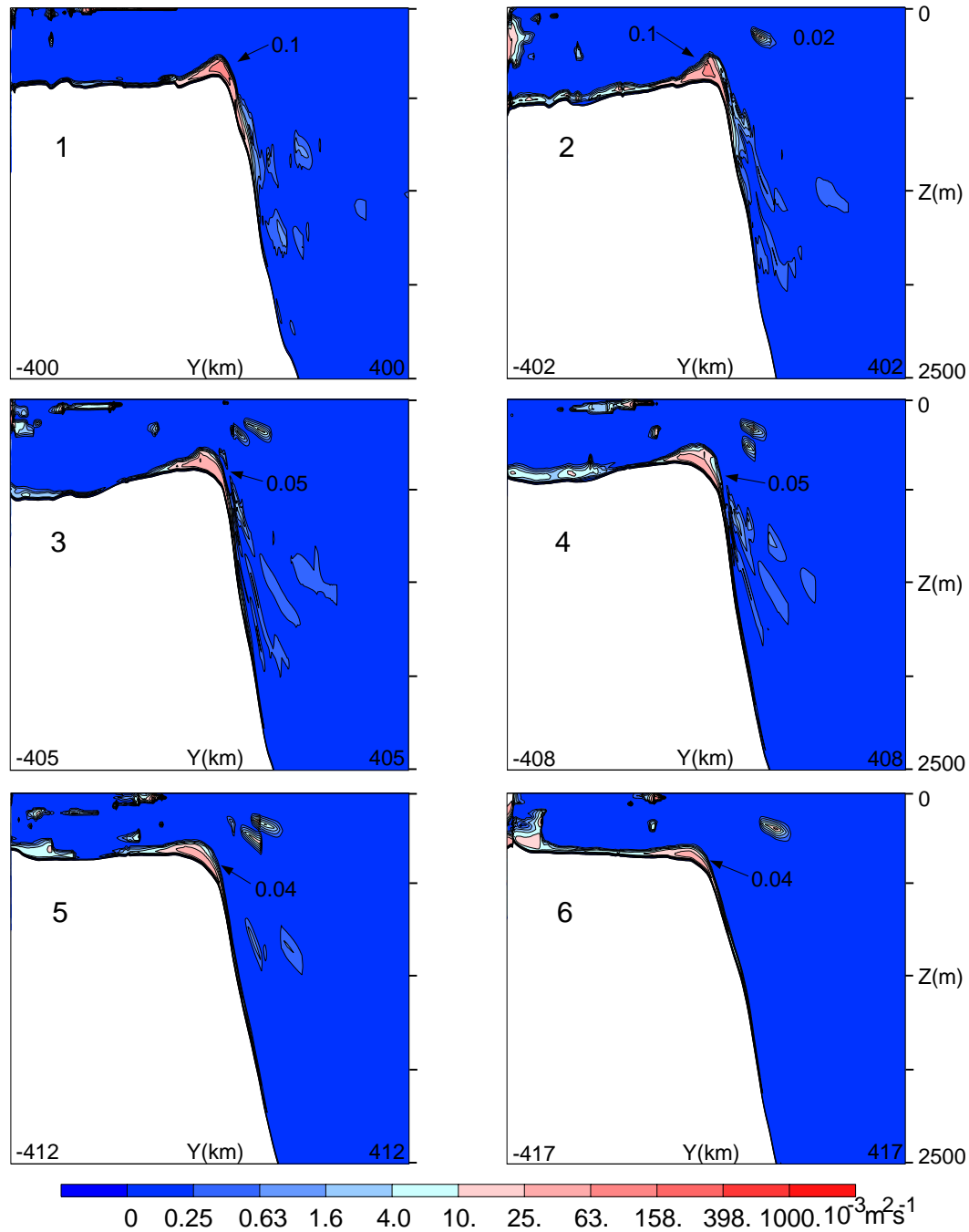


Figure 5.4: Summer mean (20 days) eddy viscosity coefficients ($\text{m}^2 \text{ s}^{-1}$) at the shelf break region of the southern Weddell Sea, considering the eight main tidal constituents in the forcing at the northern boundary for the slices (1-6) indicated in Fig. 4.12.

higher frequencies) will generate similar levels of turbulence.

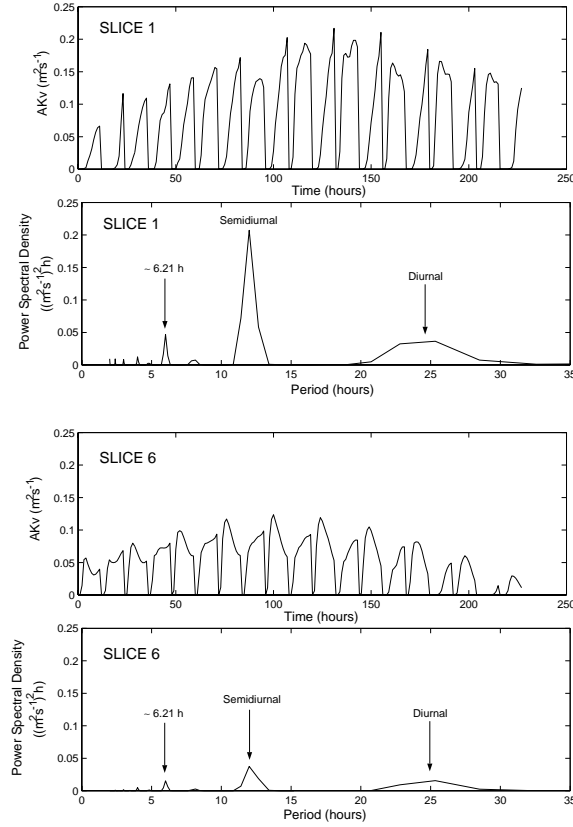


Figure 5.5: Time series and power spectral density (PSD) of the vertical eddy viscosity coefficient for a point located at the continental shelf break of the southern Weddell Sea from slice 1 (top) and slice 6 (bottom) using eight tidal constituents for the forcing.

The 6.21 hours period signal corresponds to the overtide M_4 . This tidal frequency is a higher harmonic, which does not have its origin in a corresponding forcing period but is a simple fraction of it (in this case M_2). Higher harmonics occur as a result of the nonlinear terms in the model equations, which are large in shallow waters; they do not exist in the deep ocean and are, therefore, known as shallow water tides. Its signal is also evident in the power spectrum of observed tidal currents near the ice shelf edge [Foldvik *et al.*, 2001].

Unfortunately, the modeled time series is not long enough to make a clear separation between all the diurnal and semidiurnal frequencies included in the open boundary forcing, which explains the broad area under the diurnal period obtained by the PSD analysis. One would need, for example, around six months of recorded data to distinguish K_1 from P_1 . The model results suggest that continental shelf waves and higher frequencies both increase turbulence near the bottom boundary layer at the shelf break.

Similarly to the shelf break region, vertical eddy viscosities are increased under FRIS when

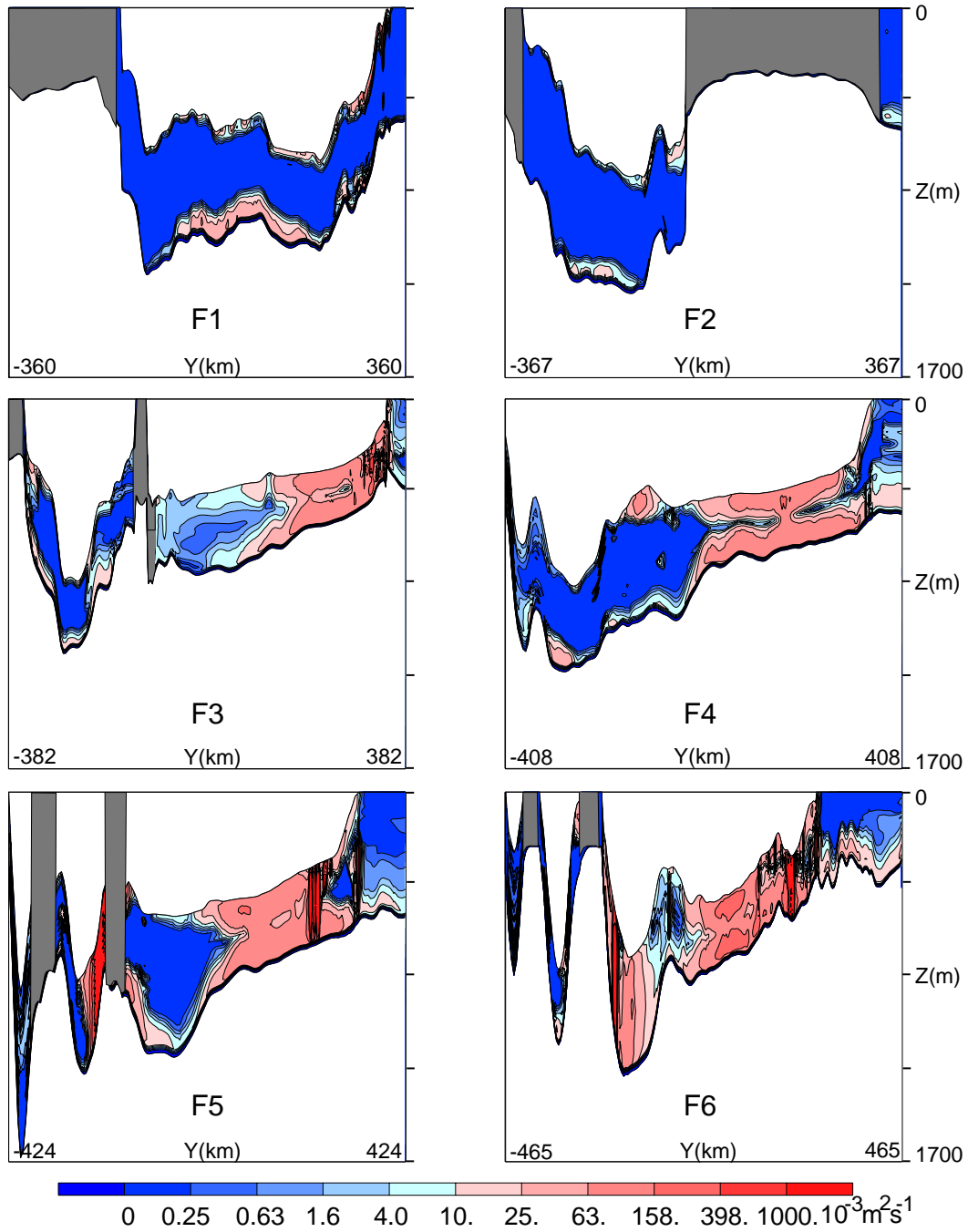


Figure 5.6: Summer mean (20 days) eddy viscosity coefficients ($\text{m}^2 \text{s}^{-1}$) beneath Filchner-Ronne Ice Shelf, considering eight tidal constituents in the forcing at the northern boundary for the slices (F1-F6) indicated in Fig. 4.22.

eight tidal constituents are considered (Fig. 5.6; note that Fig. 5.6 and Fig. 5.3 have different color scales). The spatial distribution of AK_v is the same as in the first simulation (Fig. 5.3), but a significant increase occurs in the northern cavity. The magnitude of the instantaneous tidal currents is higher with the inclusion of several tidal constituents, increasing the vertical shear between the free stream region and the boundary layers and, consequently, the eddy

coefficients. In the southern cavity, AK_v values are slightly increased (Fig. 5.6) compared to that obtained with two tidal constituents only (Fig. 5.3).

5.3 Computation for a Cross-Slice (y-z) Domain

In a two-dimensional (y-z) domain, only Poincaré waves can be modeled if a surface barotropic wave is prescribed at the open boundary. In order to gain some insight into the consequences of employing this approach to quantify internal tide mixing in a region where the surface barotropic wave travels as a Kelvin wave, the model was set up in such a configuration.

The model is identical to the one described in Chapters 2 and 4, except for the grid which now has 800 points in the \mathcal{Y} direction. The cross-shelf resolution and the shelf slope topography correspond exactly to that of slice 1/F1 in the full three-dimensional model. The domain is periodic in the east-west directions with all variables constant in the along-slope direction including density and depth. While the southern boundary is closed, the northern is open. The initial density field corresponds to summer stratification and the model was forced only with the M_2 frequency.

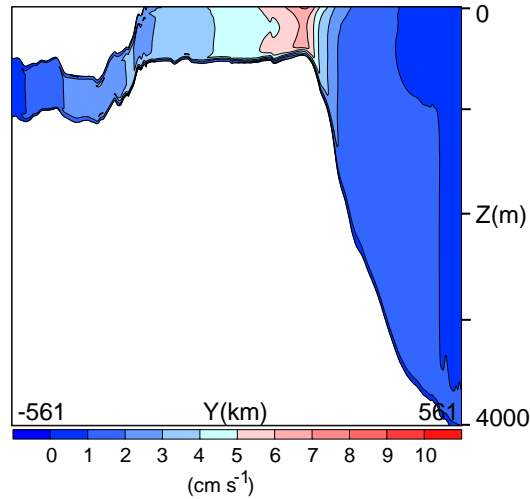


Figure 5.7: Major axis of the M_2 tidal ellipse cm s^{-1} obtained considering a 2D cross-slope domain.

In Fig. 5.7, the major axis of the M_2 tidal ellipse is presented. Interaction between tidal frequencies used as forcing may produce different three-dimensional tidal currents compared to that forced with a single frequency. However, since the major axis results produced with single and two-frequency forcings were only slightly different, Fig. 4.16 slice 1 can be used for comparison with Fig. 5.7.

The magnitude of the major axis of the tidal ellipse (Fig. 5.7) has a maximum at the shelf break ($\approx 7 \text{ cm s}^{-1}$), decreasing towards the ice shelf edge. The vertical shear near the pycnocline is reduced, and an internal tide was generated at the middle slope. Comparing these results with Fig. 4.16, slice 1, it is evident that the model response is different since the wave physics for this model setup are entirely different. Differences in the form of the tidal ellipse are also found: in this simulation tidal ellipses (not shown) are much more circular on the shelf than in 3D case, due to the periodic perpendicular forcing which reaches the shelf break and the continental shelf. Beneath FRIS, while with the 3D-model (Fig. 4.23) maxima M_2 tidal currents were about 7.5 cm s^{-1} near the ice shelf edge (considering the semi-major axis), with the 2D-approach they reach only 2 cm s^{-1} .

In Fig. 5.8a and 5.8b, mean AKv values are shown using the 3D and the 2D (y-z) approaches. While at the shelf break and in the cavity, the maximum AKv value (Fig. 5.8b) is reduced by ≈ 5 times compared to results from the 3D model (Fig. 5.8a), on the shelf, mixing in the bottom boundary layer increases. For both phenomena, the main reason must be related to differences in the along-slope velocities as already suggested by the circular form of the tidal ellipse. Furthermore, there is no apparent turbulent mixing at the pycnocline as in the previous results. This suggests that the trapped wave found in the 3D-model results propagates as a Kelvin wave, explaining why this wave is not influenced by the critical latitude singularity and, thus, propagates southward from it (Subsection 4.7.1). Near the surface layer at the upper slope, high values of AKv are due to the shear in the water column created by the internal tide.

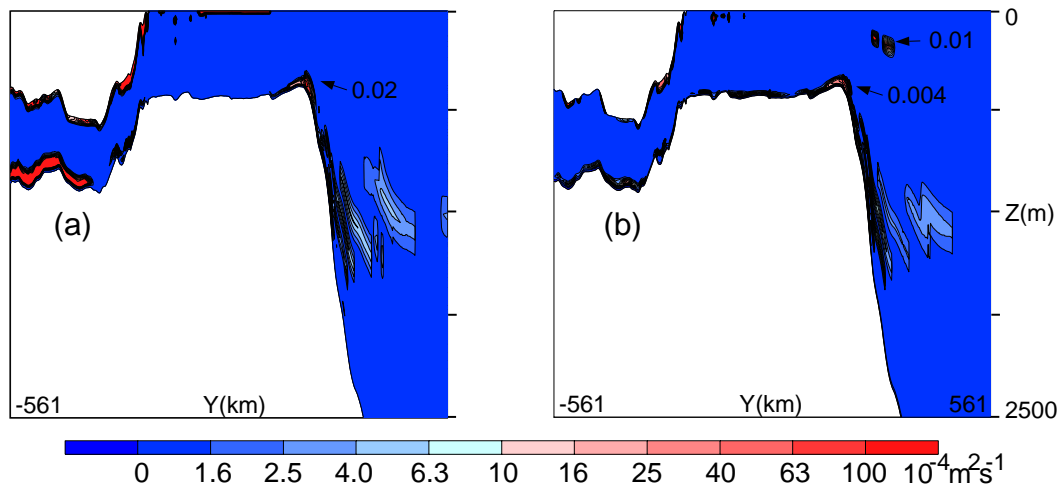


Figure 5.8: (a) Mean vertical eddy viscosity $\text{m}^2 \text{s}^{-1}$ obtained by forcing the numerical model only with the M_2 frequency and using (a) the 3D approach and (b) considering a 2D cross-slope domain.

5.4 Summary

The model results show that tidal mixing is concentrated at the continental shelf break and on the shelf. Its intensity is higher at the eastern than at the western shelf break, due to the location of the M_2 critical latitude in the southern Weddell Sea. Power spectral density plots of points located at the shelf break show the decay of the semidiurnal signal in the vertical viscosity from east to west indicating a high spatial variability of the vertical viscosity (and diffusivity, see Appendix C). Shallow water constituents (e.g., M_4) also contribute significantly to tidal mixing at the shelf break. This is true throughout the year. Differences, however, are found in the upper water column. During winter, due to the low static stability, turbulent mixing influences a broad portion of the water column, while in summer, the mixing is limited to the bottom boundary layer and the pycnocline. Because the velocity difference between the generated internal tide and the surroundings is less than 1 cm s^{-1} , the corresponding shear leads to only moderately increased values of vertical viscosity.

Beneath Filchner-Ronne Ice Shelf, tidal vertical mixing is strongly related to rough topography (western side) and to the water column thickness (northern cavity). These are the regions where maxima tidal currents and high predicted or observed [Makinson and Nicholls, 1999] melting rates (Subsections 4.7.2 and 4.8.2) are found. Therefore, vertical mixing competes with the stratifying influence of the basal melting, and a balance between them must exist, causing tidal fronts (a hydrographic transition between a vertically well-mixed and a stratified region) [MacAyeal, 1984a]. Makinson and Nicholls [1999] affirm that, with the exception of the ice shelf front area, the possible density contrast across a mixing front beneath FRIS (0.2 kg m^{-3}) is too small for the development of frontal flows. The seasonal variability in stratification beneath FRIS leads to slightly higher values of AK_v during winter at isolated points. If tidally induced mixing is higher and a larger volume of HSSW is available during winter [Nicholls, 1996], this could imply in enhanced ISW formation during this season compared to summer.

The inclusion of the diurnal frequencies in the open boundary forcing have a great impact on the values of AK_v , increasing them equally at the shelf break and beneath Filchner-Ronne Ice Shelf. Because the instantaneous tidal velocity is higher, the vertical shear at the boundary layers is increased and, consequently, also the eddy coefficients.

The y-z cross-slope approach (Subsection 5.3), frequently used in simulations of internal tides [e.g., Holloway, 1996; Robertson, 2001], proved to be not appropriate for shelf seas where

the tidal wave propagates as a Kelvin wave. With such approach, the wave dynamics are different and the angle of incidence of the Kelvin wave (or the surface barotropic tide) cannot be accurately modeled. As pointed out by Guizien *et al.* [1999], the angle of incidence plays an important role in determining the dissipation rate of tidal energy on the shelf and, consequently, in the generation of internal tides.

The model results demonstrate the importance of the three-dimensionality of the numerical approach and the number of tidal constituents when investigating tidal mixing. A grid resolution capable to solve small topographic features is also needed, because they are associated with high levels of turbulent mixing [Polzin *et al.*, 1997]. The values of vertical eddy coefficients obtained through tidal forcing were considerably high, reaching values up to 1×10^{-1} at the shelf break and beneath FRIS. Considering the background value for vertical diffusivity in the open ocean of $\approx 1 \times 10^{-5} \text{ m}^2 \text{ s}^{-1}$ [Polzin *et al.*, 1997; Webb and Sugimotohara, 2001], the model results support earlier hypothesis based on observations [e.g., Foster *et al.*, 1987] and barotropic tidal models [e.g., Makinson and Nicholls, 1999] that tides increase mixing and may be the major contributor to the generation of turbulence in the southern Weddell Sea which is necessary for the formation of deep and bottom waters.

Chapter 6

Conclusions and Outlook

The Weddell Sea, Antarctica, has been recognized as being the major site of deep and bottom water formation in the Southern Ocean [Brennecke, 1921; Carmack, 1977; Orsi *et al.*, 1999]. Because tides are supposed to play an important role in this formation process contributing the energy for mixing of different water masses, they recently have been the subject of intensive studies to determine their relative importance for polar oceanography.

In this study, tidal processes and their effects in the Weddell Sea have been investigated using the S-Coordinate Primitive Equation Ocean Model (SCRUM). The model was modified to allow for the inclusion of the horizontal component of the Earth's rotation vector, the equilibrium tide, and ice shelf cavities. Versions with 2D (x-y, y-z) and 3D equations served to simulate barotropic and baroclinic tides, and the resulting tidally induced mixing in the southern Weddell Sea.

The strongest tidal currents in the southern Weddell Sea are found at the shelf break, on the continental shelf and Filchner-Ronne Ice Shelf (FRIS) cavity. There is a distinct predominant frequency in each of these regions: while in shallower areas, as continental shelf and ice shelf cavity, semidiurnal frequencies are the dominant period, at steep topographic changes, as the shelf break, diurnal frequencies predominate.

Associated with the strongest currents are the regions with high tidally induced mixing. In general, tidal currents increase the level of turbulence in the water column through friction between the flow and the boundary layers, i.e. seabed and base of the ice shelf in the case of ice covered regions. But several other mechanisms also contribute to increase friction and, consequently, mixing:

- resonance at the M_2 critical latitude which results in a depth-dependent profile of the

tidal current,

- diurnal continental shelf waves,
- waves trapped to the pycnocline,
- internal tides, and
- overtides.

A schematic representation of the mechanisms and regions in the southern Weddell Sea susceptible to strong tidally induced mixing is presented in Fig. 6.1. All these mechanisms and physical processes produce locally large vertical viscosity and diffusivity coefficients as high as $1 \times 10^{-1} \text{ m}^2 \text{ s}^{-1}$. This is a significant increase compared to the background value in the open ocean of $\approx 1 \times 10^{-5} \text{ m}^2 \text{ s}^{-1}$ [Polzin *et al.*, 1997; Webb and Sugimotohara, 2001].

Although the mechanisms listed above have the same source of energy, i.e. the barotropic tide, their mixing effects are felt in different portions of the water column (see Fig. 6.1b). For example, while the resulting depth-dependent profile of M_2 tidal currents near the critical latitude produces mixing almost throughout the water column because of the thick bottom boundary layer, the turbulence associated with diurnal continental shelf waves is more restricted to the near bottom layers; and, trapped waves increase mixing only near the pycnocline. From Fig. 6.1b, it is possible to visualize that strong mixing is generally found along vertical and horizontal “boundaries”, as the continental margin and ice shelf edge, bottom and surface boundary layers, and pycnocline which is a boundary between two different water masses.

Besides the vertical variability of the tidal mixing, also a large horizontal variability of the magnitude of the tidally induced turbulence occurs. As shown in Fig. 6.1a, all cited processes and mechanisms act together at the eastern Weddell Sea continental shelf break, leading to increased net mixing in that area. Further west, only diurnal continental shelf waves can significantly produce turbulence at the shelf break. In the FRIS cavity, tidal mixing is stronger near the northwestern corner than eastward due to the increased bottom roughness in that area.

The western Weddell Sea is normally covered by thick sea ice (multi-year ice) all year long [e.g., Heygster *et al.*, 1996]. Frictional drag at the sea ice/ocean interface would produce vertical shear, increasing the level of turbulence in that region, as demonstrated by Furevik and Foldvik [1996] for the Barents Sea and modeled here beneath FRIS. The thickness of this surface layer increases when approaching the M_2 critical latitude which is located in the middle

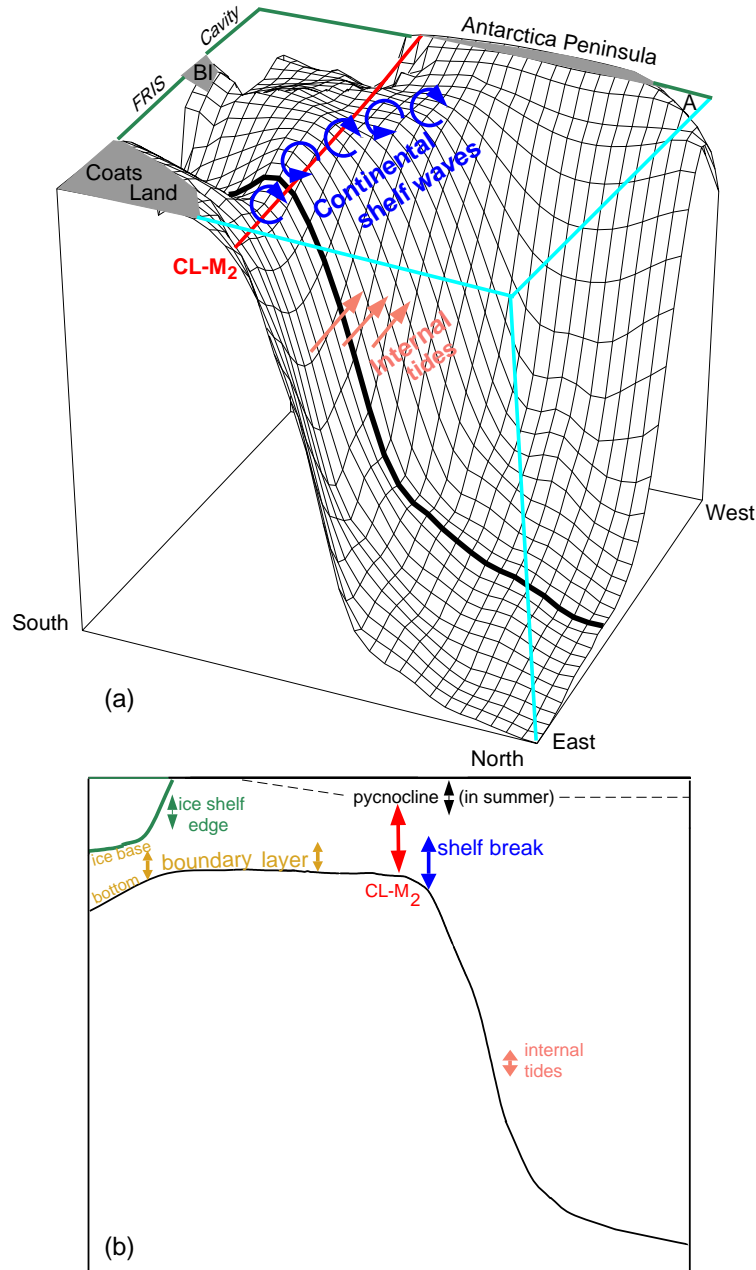


Figure 6.1: Schematic representation of regions and processes of tidally induced vertical mixing in the southern Weddell Sea. (a) 3D-view on the southern Weddell Sea from the NE; (b) vertical slice along the thick line. Size of the double arrows are qualitatively proportional to the strength of the mixing.

of the western continental shelf. In the eastern Weddell Sea, interactions between sea ice and tidal currents are not expected to intensify turbulent mixing near the surface, since thin sea ice is more common in this area. In this case, sea ice does not behave as a rigid lid, but it will drift according to the tidal currents [Padman and Kottmeier, 2000].

Tidal mixing can be interpreted as energy available to mix different water masses, and the results presented in this work suggest that tides contribute significantly to the turbulent mixing

in the southern Weddell Sea. Especially at the continental shelf break, tidally induced mixing might be essential for the formation of deep and bottom waters [Gordon, 1998]. Convection at the shelf break, possibly producing eddy coefficients of the same order, might also contribute to water mass formation but is limited mainly to the winter season whereas tides act continuously.

Beneath FRIS, tidal mixing plays a crucial role. While at the continental shelf break, the generation of turbulence will contribute to water mass *formation*, at ice shelf cavities, it will contribute to water mass *modification* through heat transport to the boundary layer resulting in ISW formation.

One- [e.g., Jenkins, 1991], two- [e.g., Hellmer and Olbers, 1989] and three-dimensional [e.g., Gerdes *et al.*, 1999] models for the circulation under FRIS do not consider tidal motion. Therefore, while reproducing fairly accurate melt rates beneath Filchner Ice Shelf and the central Ronne Ice Shelf, they fail to reproduce the observed values for the ice shelf edges and the grounding lines. According to the tidal model results, these are exactly the areas where maxima values of vertical viscosity and diffusivity coefficients are found, which are almost three orders of magnitude greater than the constant value used in the ice shelf cavity models (about $1 \times 10^{-4} \text{ m}^2 \text{ s}^{-1}$). Although only in selected shallow areas beneath the ice shelf tidally driven mixing is high enough to cause increased heat exchange at the ice shelf base, the induced melting might modify significantly the thermohaline response of the cavity in the ice shelf cavity models [Makinson and Nicholls, 1996].

Tides and Lead Formation

Besides the thermodynamic effect of tides on the formation of water masses beneath ice shelves, tidal currents also contribute dynamically to this formation process, especially at the continental shelf break, through opening leads in the ice cover.

The periodic tidal currents generate the periodic change in the ice concentration distribution. If during half of the tidal period, sea ice divergence occurs, a lead is opened which increases significantly heat fluxes between ocean and atmosphere [Launiainen and Vihma, 1994]. This leads to sea ice formation [Kowalik and Proshutinsky, 1994] and, consequently, salt flux into the upper ocean. During the second half of the tidal period, the converging motion may result in ice ridging. The effect of periodic tidal currents on sea ice concentration is more important in areas where tidal currents are strong as steep topographic changes at continental

shelf breaks [Kowalik and Proshutinsky, 1994] and close to the ice shelf edge [Padman and Kottmeier, 2000]. Also at isolated banks (e.g., General Belgrano Bank) and seamounts (e.g., Maud Rise), tidal currents are increased and tides can contribute to reduction of sea ice concentration, but in this case, the lead formation occurs due to vertical heat transport by topographic waves resulting in the formation of deep waters [Beckmann *et al.*, 2001].

A quantitative estimate of the lead formation is calculated by multiplying half of the tidal period by the standard deviation of the divergence of the horizontal tidal velocities at the surface. An observational study in the Weddell Sea [Padman and Kottmeier, 2000] shows that lead formation due tidal action are expected along the Ronne ice front and at narrow bands along the continental shelf break. The model results confirm this picture (Fig. 6.2). Over deep water, weak tidal currents will not produce lead formation.

Maxima values for the lead formation are found at the shelf break, reaching 14% when 8 tidal constituents are included in the open boundary forcing (Fig. 6.2). Most of this increased divergence can be attributed to the continental shelf waves at diurnal period. When only M_2 and S_2 are considered, the percentage reduces to 4% at the shelf break, although near the FRIS edge percentages are basically the same as the previous simulation. The lead formation generated by tidal currents computed with a 2D (x-y) model is also decreased due to the proximity of the M_2 critical latitude. For this slice, the critical latitude is located at the shelf break which leads to depth-dependent tidal currents as shown in Chapter 4. In a 2D-approach, the depth-integrated currents will not feel this effect, resulting in weaker currents and, consequently, weaker divergent.

Satellite images do not show any reduction of ice concentration at the southern shelf break of the Weddell Sea [Heygster *et al.*, 1996] which could be attributed to tidal activity. This may be due to the relatively coarse spatial resolution of SSM/I. In addition, wind and the mean oceanic flow may contribute much more to sea ice motion than tidal divergence, but for small spatial and short time scales, tidal divergence may enhance the fluxes of heat and salt, increasing the density of the upper levels of the water column. This dense water triggers the formation of HSSW and modifies the water characteristic at the ice shelf and shelf break fronts. The contribution of the high-frequency ice divergence to the total salt flux into the upper ocean in the western Weddell Sea was estimated to $\approx 40\%$ [Padman and Kottmeier, 2000].

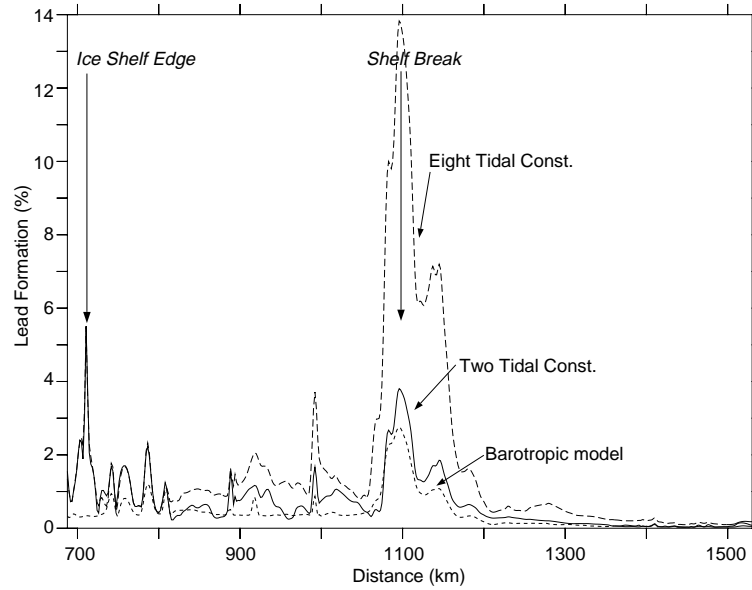


Figure 6.2: Percentage of lead formation along slice 1 (Fig. 4.12) starting at the FRIS edge and including M_2 and S_2 (solid line) and the eight main tidal constituents (M_2 , S_2 , N_2 , K_2 , K_1 , O_1 , P_1 , Q_1 , dashed line) for the open boundary forcing. Short-dashed line is the lead formation calculated using barotropic velocities obtained with the 2D (x-y) barotropic model.

Outlook

The three-dimensional experiments presented in this study were conducted with a coarse along-slope grid resolution which smoothes the topography such that small scale variations in this direction are absent. As demonstrated in Chapter 3 and already observed by Foldvik *et al.* [1990], diurnal frequencies have the highest barotropic velocities at the continental shelf break due to the existence of continental shelf waves. Since such waves depend on the along-slope bathymetry, this 3D-model cannot accurately represent them. In addition, modeled tidal mixing shows that these waves significantly contribute to the mixing at the Weddell Sea continental shelf break. This especially on the western side where the effect of the critical latitude on the semidiurnal frequencies is reduced and mixing can be of the same order for diurnal and semidiurnal frequencies. These waves also play an important role by increasing the divergence of the horizontal tidal velocities at the surface and, thus, the percentage of lead formation. Therefore, to accurately estimate tidal mixing and tidally induced lead formation in the Weddell Sea, these waves need to be considered in a 3D-tidal model which resolves bottom topography on fine scales (about 4-5 km). A grid resolution of 2 km in the cross-slope direction to accurately represent internal tides, as used in this study, is not necessary. As demonstrated, internal tides are not the main source of turbulent mixing in the southern Weddell Sea and an accurate

estimate of tidally induced mixing can be obtained without their consideration.

Tides and their effects have so far been disregarded in climate models. Only in the last 2-3 years, developers and users of climate models start to pay attention to them. In this study, the tides' capability to modify the local ocean physics was demonstrated, showing the necessity and motivating ongoing efforts to include tidal effects in regional and global climate models. However, the biggest difficulty is related to the grid resolution. In general, climate models are too coarse (about 2° to 4°) for an accurate representation of tides. Although some kind of parameterization could be made, it remains to be a challenging task. E.g., a parameterization of the tidal vertical mixing should account for the effects of the critical latitude and of the diurnal continental shelf waves. Both processes are related to tides but produce a completely different distribution of internal shear in the water column and, consequently, different levels of vertical mixing. Perhaps, a parameterization for different tidal bands (e.g., diurnal and semidiurnal) could be a first step. Another, even simpler parameterization would be to prescribe vertical mixing as a function of location, taken from tidal models. According to it, higher values of eddy coefficients could be applied at "boundary" regions as continental shelf breaks and boundary layers. They could also vary in time, representing the variability of the tidal currents during a tidal period.

The interaction between tidal currents and seamounts is a topic which still needs further investigation. As investigated by Beckmann *et al.* [2001] at Maud Rise, tidal motion is capable of modifying the mixed layer above the seamount enough to delay and reduce sea ice formation throughout the winter. Similarly, tidal mixing over Arctic seamounts transfers heat from the warm Atlantic water to the surface [Kowalik and Proshutinsky, 1994], decreasing sea ice concentration in the region. Detailed studies with a full tidal sea ice-ocean coupled model applied for e.g. the Maud Rise region would be the next step to further identify the relative importance of this seamount for the local oceanography and sea ice cover.

Additional effort should also be made in the collection of data. Because magnitude and direction of tidal currents are strongly dependent on depth and affected by small topographic features, high resolution bathymetric data sets are necessary for the polar regions, especially for ice shelf areas where a lack of ice shelf thickness and bottom topography still exists. Deployment of moorings, especially along the southern Weddell Sea shelf break, would give important information about the wave characteristics of the continental shelf waves and would

help to validate tidal model results.

Appendix A

Current Meter Data

In the following table, details about the current meter data used for model comparison are given. If the depth of the observational site is not known, then it is indicated as NaN in the table.

| Latitude | Longitude | Depth _{obs} (m) | Depth _{mod} (m) | Reference |
|----------|-----------|--------------------------|--------------------------|-------------------------------|
| 59°08'S | 37°57'W | 2870 | 2781 | Barber and Crane [1995] |
| 60°11'S | 38°08'W | 2969 | 2580 | Barber and Crane [1995] |
| 62°05'S | 40°35'W | 3375 | 3259 | Barber and Crane [1995] |
| 63°10'S | 42°46'W | 3855 | 3858 | Barber and Crane [1995] |
| 63°29'S | 52°06'W | 950 | 1448 | Fahrback <i>et al.</i> [1994] |
| 63°31'S | 41°45'W | 4580 | 4397 | Barber and Crane [1995] |
| 63°45'S | 50°54'W | 2460 | 2412 | Fahrback <i>et al.</i> [1994] |
| 63°56'S | 40°54'W | 4575 | 4688 | Barber and Crane [1995] |
| 63°57'S | 49°09'W | 3480 | 3418 | Fahrback <i>et al.</i> [1994] |
| 64°01'S | 01°20'W | 3721 | 3568 | Bersch <i>et al.</i> [1992] |
| 64°24'S | 00°22'W | 5019 | 4006 | Bersch <i>et al.</i> [1992] |
| 64°25'S | 45°51'W | 4390 | 4347 | Fahrback <i>et al.</i> [1994] |
| 64°49'S | 42°29'W | 4650 | 4638 | Fahrback <i>et al.</i> [1994] |
| 64°58'S | 02°00'W | 4331 | 4946 | Bersch <i>et al.</i> [1992] |
| 65°38'S | 36°30'W | 4742 | 4795 | Fahrback <i>et al.</i> [1994] |
| 65°39'S | 37°42'W | 4730 | 4701 | Fahrback <i>et al.</i> [1994] |
| 65°55'S | 35°49'W | 4770 | 4746 | Barber and Crane [1995] |
| 65°58'S | 33°20'W | 4800 | 4744 | Fahrback <i>et al.</i> [1994] |
| 66°03'S | 00°47'W | 4100 | 4291 | Bersch <i>et al.</i> [1992] |
| 66°16'S | 30°18'W | 4750 | 4754 | Fahrback <i>et al.</i> [1994] |
| 66°26'S | 41°03'W | 4590 | 4482 | Middleton and Foster [1977] |
| 66°37'S | 27°07'W | 4836 | 4807 | Fahrback <i>et al.</i> [1994] |
| 66°48'S | 55°01'W | NaN | 1755 | Levine <i>et al.</i> [1997] |
| 66°48'S | 54°27'W | NaN | 2146 | Levine <i>et al.</i> [1997] |

continued on next page

Table A.1: *continued*

| Latitude | Longitude | Depth _{obs} (m) | Depth _{mod} (m) | Reference |
|----------|-----------|--------------------------|--------------------------|--------------------------------|
| 66°59'S | 04°59'E | 4158 | 387 | Bersch <i>et al.</i> [1992] |
| 66°59'S | 53°11'W | 2900 | 2899 | Levine <i>et al.</i> [1997] |
| 67°04'S | 24°52'W | 4840 | 4888 | Fahrbach <i>et al.</i> [1994] |
| 67°37'S | 55°19'W | NaN | 1602 | Levine <i>et al.</i> [1997] |
| 67°40'S | 54°43'W | NaN | 2001 | Levine <i>et al.</i> [1997] |
| 67°50'S | 53°18'W | 2900 | 2715 | Levine <i>et al.</i> [1997] |
| 68°28'S | 53°09'W | 2900 | 2428 | Levine <i>et al.</i> [1997] |
| 68°49'S | 17°54'W | 4740 | 4734 | Fahrbach <i>et al.</i> [1994] |
| 69°07'S | 55°46'W | NaN | 1242 | Levine <i>et al.</i> [1997] |
| 69°19'S | 53°38'W | 2700 | 2616 | Levine <i>et al.</i> [1997] |
| 69°25'S | 52°10'W | NaN | 3127 | Levine <i>et al.</i> [1997] |
| 69°39'S | 15°42'W | 4728 | 4714 | Fahrbach <i>et al.</i> [1994] |
| 70°19'S | 13°39'W | 4330 | 3031 | Fahrbach <i>et al.</i> [1994] |
| 70°23'S | 13°32'W | 2900 | 2847 | Fahrbach <i>et al.</i> [1994] |
| 70°26'S | 08°18'W | 468 | 471 | Fahrbach <i>et al.</i> [1992] |
| 70°29'S | 13°07'W | 2364 | 2343 | Fahrbach <i>et al.</i> [1994] |
| 70°30'S | 13°09'W | 2450 | 2343 | Fahrbach <i>et al.</i> [1994] |
| 70°42'S | 12°21'W | 2123 | 1455 | Fahrbach <i>et al.</i> [1994] |
| 70°55'S | 11°58'W | 1555 | 722 | Fahrbach <i>et al.</i> [1994] |
| 70°56'S | 11°58'W | 1522 | 722 | Fahrbach <i>et al.</i> [1994] |
| 70°59'S | 11°49'W | 2364 | 575 | Fahrbach <i>et al.</i> [1994] |
| 71°02'S | 11°45'W | 676 | 575 | Fahrbach <i>et al.</i> [1994] |
| 71°03'S | 11°46'W | 467 | 575 | Fahrbach <i>et al.</i> [1994] |
| 71°03'S | 11°44'W | 380 | 575 | Fahrbach <i>et al.</i> [1994] |
| 71°06'S | 20°47'W | 4440 | 4370 | Fahrbach <i>et al.</i> [1994] |
| 71°08'S | 12°12'W | 682 | 487 | Fahrbach <i>et al.</i> [1992] |
| 72°53'S | 19°37'W | 415 | 1121 | Fahrbach <i>et al.</i> [1992] |
| 73°37'S | 26°07'W | 3360 | 1633 | Fahrbach <i>et al.</i> [1994] |
| 73°43'S | 38°36'W | 1915 | 1328 | Middleton <i>et al.</i> [1982] |
| 74°06'S | 39°22'W | 720 | 664 | Middleton <i>et al.</i> [1982] |
| 74°08'S | 39°19'W | 650 | 591 | Foldvik <i>et al.</i> [1990] |
| 74°23'S | 37°39'W | 475 | 467 | Foldvik <i>et al.</i> [1990] |
| 74°24'S | 39°06'W | 465 | 430 | Middleton <i>et al.</i> [1982] |
| 74°26'S | 39°24'W | 475 | 412 | Middleton <i>et al.</i> [1982] |
| 74°40'S | 33°56'W | 475 | 534 | Middleton <i>et al.</i> [1982] |
| 74°42'S | 60°48'W | 613 | 512 | Woodgate <i>et al.</i> [1998] |
| 75°09'S | 58°43'W | 601 | 471 | Woodgate <i>et al.</i> [1998] |
| 76°29'S | 53°00'W | 431 | 237 | Foldvik <i>et al.</i> [2001] |
| 78°42'S | 64°53'W | 330 | 369 | Makinson and Nicholls [1996] |
| 78°52'S | 71°20'W | 485 | 319 | Makinson and Nicholls [1996] |

Appendix B

Tidal Ellipse Complex Demodulation

An ellipsoidal current motion, as tidal currents, is entirely described by four parameters:

U maximum current velocity, or semi-major axis

e eccentricity, i.e. the ratio of semi-minor (V) to semi-major axis. Negative values indicates that the ellipse rotates in an anticyclonic sense.

ψ inclination, or angle between east (x) direction and semi-major axis

ϕ phase angle, i.e. time of maximum velocity with respect to a chosen origin of time (normally, the Greenwich Meridian).

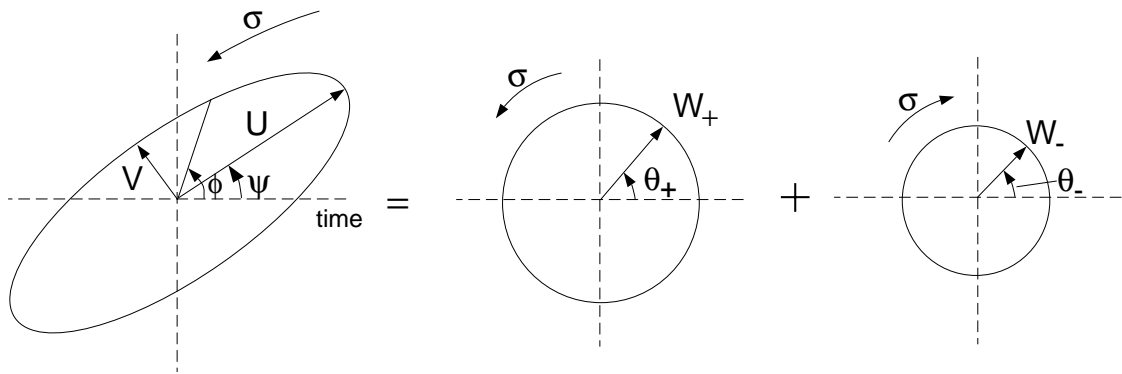


Figure B.1: Decomposition of a tidal current ellipse (frequency σ), specified by the four ellipse parameters: magnitude of the semi-major axis U , eccentricity $e=V/U$ (V : semi-minor axis), inclination ψ and phase angle ϕ , into two counterrotating currents of constant magnitudes $W_{(+,-)}$ and directions $\theta_{(+,-)}$.

Following Prandle [1982], to understand the vertical structure of these four parameters, the tidal ellipse is decomposed into two counterrotating circular velocity components with fixed amplitudes ($W_{(+,-)}$) and phases ($\theta_{(+,-)}$) by complex demodulation (Fig. B.1). Subscripted

positive and negative signals indicate anticlockwise and clockwise rotation, respectively. In terms of these rotation vector parameters:

$$U = W_+ + W_-$$

$$e = (W_+ - W_-)/(W_+ + W_-)$$

$$\psi = (\theta_- + \theta_+)/2$$

$$\phi = (\theta_- - \theta_+)/2.$$

Appendix C

The Effect of the \tilde{f} -Terms

As outlined in Chapter 2, the equations of motion for this modeling study have been extended to include the horizontal component of the Earth's rotation (\tilde{f}). Generally, the \tilde{f} -terms modify the character of the propagation of internal waves. Baines and Miles [2000] demonstrate that it causes lateral displacements of their rays and local changes in their slope and, although these changes are locally small (13 km for propagation through a depth change of 4000 m), the effect is cumulative so that the displacements can be substantial at large distances from the source.

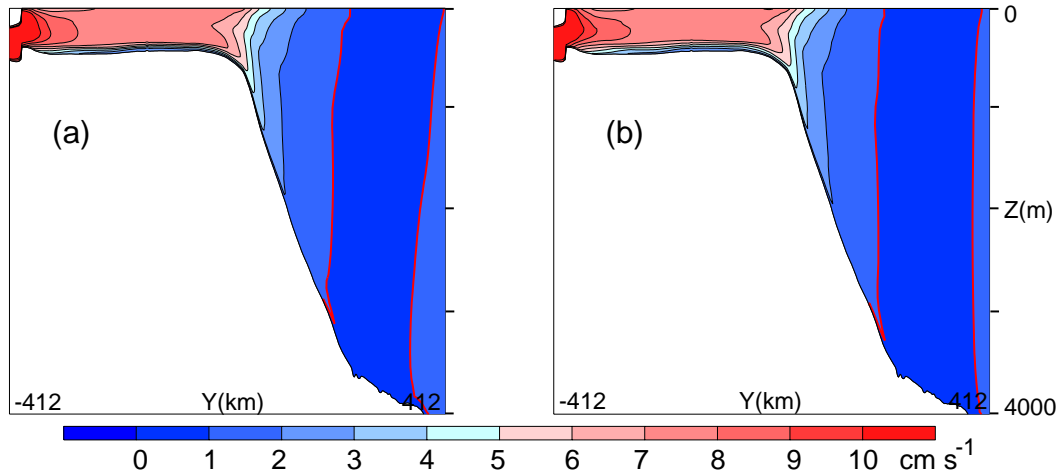


Figure C.1: Major axis of the M_2 tidal ellipse (cm s^{-1}) obtained including (a) and not including (b) \tilde{f} in the model equations. The red isolines evidence the difference between the two figures.

The model results, however, show only a small tilt of the isolines of the major axis of the tidal ellipse toward the equator (Fig. C.1, more evident in the red isolines). When \tilde{f} is considered, the vector of the Earth's rotation is no longer vertical relative to the local cartesian coordinate system, but tilted to the North [Beckmann and Diebels, 1994] what causes a slight inclination of the isolines (the small inclination of the isoline near the surface in the simulation

without \tilde{f} (Fig. C.1b) is due to a trapped wave at the pycnocline).

Apparently, the generated internal tide dissipates rapidly (Subsection 4.7.1), and does not propagating through a long distance to show some cumulative effect. Furthermore, this lateral displacement is stronger at deep waters, and the internal tide in the model propagates along-slope what can be considered still 'shallow waters' for this effect be felt.

Summarizing, the inclusion of \tilde{f} in the model equations did not produce any significant difference with respect to tidal currents and tidally induced mixing if compared to results without it. In regions with strong propagating internal tides or for internal tides which propagate for thousand kilometers, its effect may be more evident. Also in the vicinity of isolated topographic features, such as seamounts, the inclusion of \tilde{f} -terms in the hydrodynamic equations will produce significantly different results [Beckmann and Diebels, 1994].

Appendix D

Stability Functions in the MY2.5 Scheme

In the model results, the vertical viscosity and diffusivity coefficients had approximately the same order of magnitude and spatial distribution. According to Mellor-Yamada Scheme, level 2.5 (Subsection 4.3.2), both coefficients have identical form. The only difference between them is the stability functions S_m (for momentum) and S_h (for tracers) used to calculate them:

$$S_h = \frac{0.493928}{1. + 34.6764 * G_h}$$

$$S_m = \frac{21.3624 * S_h * G_h + 0.393272}{1. + 6.12720 * G_h}$$

where G_h is the stability function Galperin *et al.* [1988] which is dependent of the Brunt-Väisälä frequency N .

In Fig. D.1, S_m and S_h are plotted versus G_h . Both coefficients have very similar values when $G_h > 0$ (stable water column). When G_h is negative, the water column is statically unstable. Thus, in order to enhancing mixing, the values of S_m and S_h are increased, as well the difference between them. The form of these damping functions was chosen to better fit oceanographic data [see Mellor and Yamada, 1982; Galperin *et al.*, 1988].

In the numerical model, stratification in all model domain is initialized stable. Instability will only result if vertical shear of horizontal flow is sufficiently strong to advect denser water above lighter because other effects that could produce instabilities, such as surface cooling

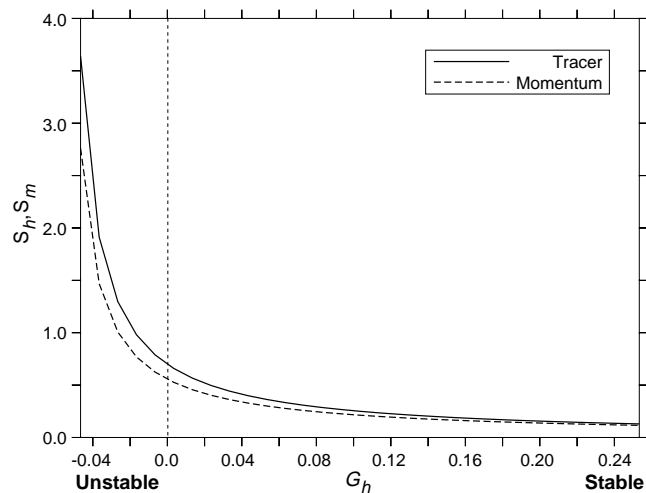


Figure D.1: Stability functions for momentum (thick dashed line) and tracers (solid line) used in the Mellor-Yamada closure scheme, level 2.5.

or salinization, are not included in the BRIOS tidal model. Since the time-mean values of AK_v and AK_d were similar in the model results, static instability did not occur often during the simulations. This may be explained by the periodicity of the tidal currents: if temporary instability occurs during the ebb, the water column is stabilized again due to the reverse flood current. And this sequence of stable-unstable-stable water column may occur in a too short time scale (equal to half of a tidal period) to make a significant difference in the time-mean value of AK_v and AK_d .

Appendix E

Gyroscopic Waves

When simulating a 3D-homogeneous ocean with the BRIOS tidal model, a signal very similar to baroclinicity due to stratification appeared at the continental shelf and slope (Fig. E.1a). The referred signal was a *gyroscopic wave*.

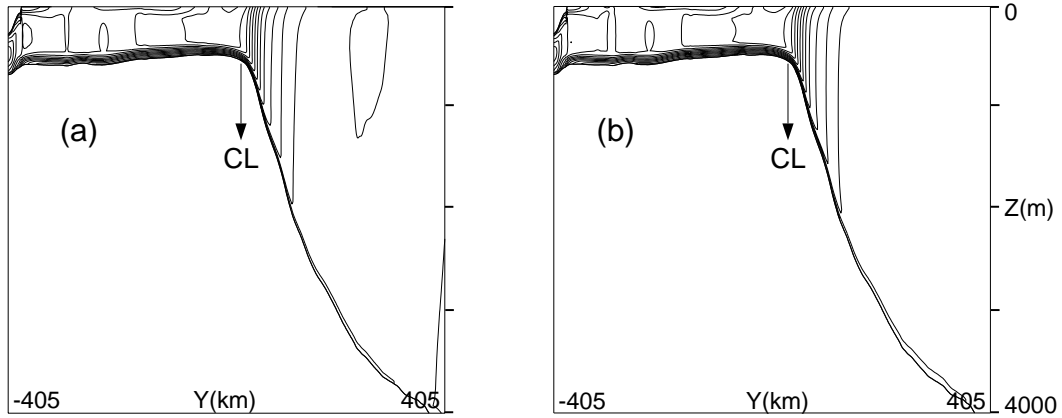


Figure E.1: M_2 major axis (cm s^{-1}) in a homogeneous ocean obtained including (a) and not including (b) \tilde{f} in the model equations. CL indicates the location of the critical latitude for the M_2 frequency.

Gyroscopic waves exist in a rotating, but unstratified fluid and their existence arise due to the Coriolis force [LeBlond and Mysak, 1978]. If only the f -terms are taken into account, their wave regime is restricted to $\omega \leq f$ and they are only possible at subinertial frequencies. In Fig. E.1b, the M_2 major axis is plotted for a cross-slice in the Weddell Sea considering a homogeneous ocean and disregarding \tilde{f} -terms. The inertial frequency (critical latitude, CL) is located exactly at the shelf break. In this case, gyroscopic waves appear only at the continental shelf and are seen as a velocity intensification near the surface and bottom boundaries due to reflections. With the same model configuration, an artificial M_4 tidal wave was prescribed at the northern boundary of the domain (see Subsection 4.3.1). This frequency is superiner-

tial throughout the model domain and, for this reason, gyroscopic waves were not generated (Fig. E.2).

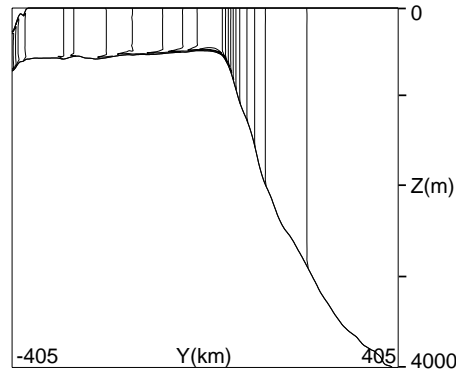


Figure E.2: Amplitude of the M_4 cross-slope component (cm s^{-1}) in a homogeneous ocean obtained not considering \tilde{f} in the model equations.

If the full Coriolis term is considered (f and \tilde{f} -terms), gyroscopic waves are possible over the whole range of latitudes, including the equatorial regions [L. Maas, pers. comm.]. In Fig. E.1a, the full Coriolis term is considered in the model equations, and gyroscopic waves are found not only on the continental shelf, but also at the slope.

Although these internal modes of motion in a homogeneous fluid are common in laboratory experiments [see Maas, 2001], in the ocean they may be more rare. As pointed out by Miles [1974], just a tiny bit of stratification alters the wave regime entirely.

Bibliography

- Andersen, P. W., O. B. and R. A. Flather [1995] Intercomparison of recent ocean tide models. *J. Geophys. Res.*, **100**(C12), 25,261–25,282.
- Arakawa, A. and V. R. Lamb [1976] Computational design of the basic dynamical processes of the UCLA general circulation model. In: *Methods of Computational Physics*, volume 17, pp. 174–265. Academic Press.
- Baines, P. G. [1973] The generation of internal tides by flat-bump topography. *Deep-Sea Res.*, **20**, 179–205.
- Baines, P. G. [1974] The generation of internal tides over steep continental slopes. *Philos. Trans. R. Soc. London*, **A277**, 27–58.
- Baines, P. G. [1982] On internal tide generation models. *Deep-Sea Res.*, **29**(3A), 307–338.
- Baines, P. G. and J. W. Miles [2000] On topographic coupling of surface and internal tides. *Deep-Sea Res.*, **47**, 2395–2403.
- Baines, P. G. and F. Xin-Hua [1985] Internal tide generation at a continental shelf/slope junction: a comparison between theory and laboratory experiment. *Dyn. Atmos. Oceans*, **8**, 297–314.
- Barber, M. and D. Crane [1995] Current flow in the northwest Weddell Sea. *Antarctic Science*, **7**, 39–50.
- Beckmann, A. and S. Diebels [1994] Effects of the horizontal component of the Earth's rotation on wave propagation on an f-plane. *Geophys. Astrophys. Fluid Dyn.*, **76**, 95–119.
- Beckmann, A., H. H. Hellmer and R. Timmermann [1999] A numerical model of the Weddell Sea: large-scale circulation and water mass distribution. *J. Geophys. Res.*, **104**(C10), 23,375–23,391.

- Beckmann, A., R. Timmermann, A. F. Pereira and C. Mohn [2001] The effect of flow at Maud Rise on the sea-ice cover - numerical experiments. *Ocean Dyn.*, **52**(1), 11–25.
- Bersch, M., G. A. Becker, H. Frey and K. P. Koltermann [1992] Topographic effects of the Maud Rise on the stratification and circulation of the Weddell Gyre. *Deep-Sea Res.*, **39**, 303–331.
- Bowden, K. F. [1983] *Physical oceanography of coastal waters*. Ellis Horwood in Marine Science. Ellis Horwood Limited, Chichester.
- Brennecke, W. [1921] Die ozeanographischen Arbeiten der deutschen antarktischen Expeditionen 1911-1912. *Archiv der Deutschen Seewarte*, **39**(1), 1–216.
- Broecker, W. S. [1987] The great Ocean Conveyor. *Oceanography*, **4**(2), 79–89.
- Carmack, E. C. [1974] A quantitative characterization of water masses in the Weddell Sea during summer. *Deep-Sea res.*, **21**, 431–443.
- Carmack, E. C. [1977] Water characteristics of the Southern Ocean south of the Polar Front. In: *A Voyage of Discovery, George Deacon 70th Anniversary Volume* (edited by Angel, M.), pp. 15–41. Pergamon, Tarrytown, New York.
- Carmack, E. C. and T. D. Foster [1975] Circulation and distribution of oceanographic properties near the Filchner Ice Shelf. *Deep-Sea Res.*, **22**, 77–90.
- Cartwright, D. E. [1969] Extraordinary tidal currents near St. Kilda. *Nature*, **233**, 928–932.
- Cartwright, D. E. [1999] *Tides: a scientific history*. Cambridge University Press, New York.
- Craig, P. D. [1987] Solutions for the internal tide generation over coastal topography. *J. Mar. Res.*, **45**, 83–105.
- Davies, A. M. [1985] On determining current profiles in oscillatory flows. *Appl. Math. Modelling*, **9**, 419–428.
- Doake, C. S. M. [1978] Dissipation of tidal energy by Antarctic ice shelves. *Nature*, **275**, 304–305.

- Doake, C. S. M. [1992] Gravimetric tidal measurement on Filchner Ronne Ice Shelf. Number 6 in Filchner-Ronne Ice Shelf Programme, pp. 34–39. Alfred-Wegener Institute for Polar and Marine Research, Bremerhaven.
- Egbert, G. D., A. F. Bennett and M. G. G. Foreman [1994] TOPEX/POSEIDON tides estimated using global inverse model. *J. Geophys. Res.*, **99**(C12), 24,821–24,852.
- Egbert, G. D. and S. Erofeeva [2000] Efficient inverse modeling of barotropic ocean tides. *submitted to J. Atmos. Oceanic Technol.*
- Egbert, G. D. and R. D. Ray [2000] Significant dissipation of tidal energy in the deep ocean inferred from satellite altimeter data. *Nature*, **405**(6788), 775–778.
- Eriksen, C. C. [1985] Implications of ocean bottom reflection for internal wave spectra and mixing. *J. Phys. Oceanogr.*, **15**, 1145–1156.
- Fahrbach, E., G. Rohardt and G. Krause [1992] The Antarctic coastal current in the southeastern Weddell Sea. *Polar Biology*, **12**, 171–182.
- Fahrbach, E., G. Rohardt, M. Schröder and V. Strass [1994] Transport and structure of the Weddell Gyre. *Ann. Geophys.*, **12**, 840–855.
- Fanjul, E. A., B. P. Gómez and I. R. Sánchez-Arévalo [1997] A description of tides in the eastern north Atlantic. *Prog. Oceanogr.*, **40**, 217–244.
- Flather, R. A. [1980] Results from a model of the north east Atlantic relating to the Norwegian coastal current. In: *The Norwegian Coastal Current* (edited by Sætre, R. and M. Mork), volume 11, pp. 427–458. University of Bergen, Geilo, Norway.
- Flather, R. A. [1987] A tidal model of the northeast Pacific. *Atmos. Ocean.*, **25**(1), 22–45.
- Foldvik, A., T. Gammelsrød and T. Tørresen [1985a] Circulation and water masses on the southern Weddell Sea. In: *Oceanology of the Antarctic Continental Shelf* (edited by Jacobs, S. S.), volume 43 of *Antarctic Research Series*, pp. 5–20. American Geophysical Union, Washington, D.C.
- Foldvik, A., T. Gammelsrød, E. Nygaard and S. Østerhus [2001] Current measurements near Ronne Ice Shelf: implications for circulation and melting. *J. Geophys. Res.*, **106**(C3), 4463–4477.

- Foldvik, A., T. Gammelsrød, N. Slotsvik and T. Tørresen [1985b] Oceanographic conditions on the Weddell Sea Shelf during the German Antarctic Expedition 1979/80. *Polar Res.*, **3**, 209–226.
- Foldvik, A., T. Gammelsrød and T. Tørresen [1985c] Physical oceanography studies in the Weddell Sea during the Norwegian Antarctic Research Expedition 1978/79. *Polar Res.*, **3**, 195–207.
- Foldvik, A., T. Kvinge and T. Tørresen [1985d] Bottom currents near the continental shelf break in the Weddell Sea. In: *Oceanology of the Antarctic Continental Shelf* (edited by Jacobs, S. S.), volume 43 of *Antarctic Research Series*, pp. 21–34. American Geophysical Union, Washington, D.C.
- Foldvik, A., J. H. Middleton and T. D. Foster [1990] The tides of the southern Weddell Sea. *Deep-Sea Res.*, **37**(8), 1345–1362.
- Foreman, M. G. G. [1977] *Manual for tidal height analysis and prediction*. Pacific Marine Sci. Rep. 77-10, Victoria, B. C.
- Foreman, M. G. G. [1978] *Manual for tidal currents analysis and prediction*. Pacific Marine Sci. Rep. 78-6, Victoria, B. C.
- Foreman, M. G. G. and R. F. Henry [1989] The harmonic analysis of tidal model time series. *Adv. Water Resour.*, **12**, 109–120.
- Foreman, M. G. G., R. F. Henry, R. A. Walters and V. A. Ballantyne [1993] A finite element model for tides and resonance along the north coast of British Columbia. *J. Geophys. Res.*, **98**(C2), 2509–2531.
- Foster, T. D. and E. C. Carmack [1976] Frontal zonal mixing and Antarctic Bottom Water formation in the southern Weddell Sea. *Deep Sea Res.*, **23**, 301–317.
- Foster, T. D., A. Foldvik and J. H. Middleton [1987] Mixing and bottom water formation in the shelf break region of the southern Weddell Sea. *Deep Sea Res.*, **34**(11), 1771–1794.
- Francis, O. and P. Mazzega [1990] Global charts of the ocean tide loading effects. *J. Geophys. Res.*, **95**(C7), 11,411–11,424.

- Furevik, T. and A. Foldvik [1996] Stability at M_2 critical latitude in the Barent Sea. *J. Geophys. Res.*, **101**(C4), 8823–8837.
- Galperin, B., L. H. Kantha, S. Hassid and A. Rosati [1988] A quasi-equilibrium turbulent energy model for geophysical flows. *J. Atmos. Sci.*, **45**, 55–62.
- Genco, M. L., F. Lyard and C. L. Provost [1994] The oceanic tides in the South Atlantic Ocean. *Ann. Geophys.*, **12**, 868–886.
- Gerdes, R., J. Determann and K. Grosfeld [1999] Ocean circulation beneath Filchner-Ronne Ice Shelf from three-dimensional model results. *J. Geophys. Res.*, **104**(C7), 15,827–15,842.
- Gill, A. E. [1973] Circulation and bottom water production in the Weddell Sea. *Deep Sea Res.*, **20**, 111–140.
- Gill, A. E. [1982] *Atmosphere-ocean dynamics*, volume 30 of *International Geophysics Series*. Academic Press, New York.
- Godin, G. [1972] *The analysis of tides*. University of Toronto Press, Toronto.
- Gordon, A. L. [1986] Inter-ocean exchange of thermohaline water. *J. Geophys. Res.*, **91**(C4), 5037–5046.
- Gordon, A. L. [1998] Western Weddell Sea thermohaline stratification. In: *Ocean, Ice, and Atmosphere: Interactions at the Antarctic Continental Margin* (edited by Jacob, S. S. and R. Weiss), volume 75 of *Antarctic Research Series*, pp. 215–240. American Geophysical Union, Washington, DC.
- Grosfeld, K., N. Blindow and F. Thyssen [1992] Bottom melting on Filchner-Ronne Ice Shelf, Antarctica, using different measuring techniques. *Polarforschung*, **62**(2/3), 71–76.
- Guizien, K., E. Barthélemy and M. E. Inall [1999] Internal tide generation at a shelf break by oblique barotropic tide: observations and modeling. *J. Geophys. Res.*, **104**(C7), 15,655–15,668.
- Haidvogel, D. B. and A. Beckmann [1999] *Numerical ocean circulation modeling*, volume 2 of *Series on Environmental Science and Management*. Imperial College Press, London.

- Han, G. [2000] Three-dimensional modeling of tidal currents and mixing quantities over the Newfoundland Shelf. *J. Geophys. Res.*, **105**(C5), 11,407–11,422.
- Hansen, W. [1949] Die halbtägigen Gezeiten im Nordatlantischen Ozean. *Deutsche Hydrogr. Z.*, **2**, 44–51.
- Hedström, K. S. [1997] *User's manual for an S-coordinate primitive equation ocean circulation model*. Inst. Mar. Coast. Sci., Rutgers University.
- Hellmer, H. H. and D. J. Olbers [1989] A two-dimensional model for the thermohaline circulation under an ice shelf. *Antartic Science*, **1**, 325–336.
- Hendershott, M. C. [1972] The effects of solid earth deformation on global ocean tides. *Geophys. J. R. Astron. Soc.*, **29**, 389–402.
- Hendershott, M. C. [1981] Long waves and ocean tides. In: *Evolution of Physical Oceanography* (edited by Warren, B. and C. Wunsch), pp. 292–341. MIT Press, Cambridge, Massachusetts.
- Hendry, R. M. [1977] Observations of the semidiurnal tide in the western North Atlantic Ocean. *Phil. Trans. R. Soc. London*, **A286**, 1–24.
- Heygster, G., L. T. Pedersen, J. Turner, C. Thomas, T. Hunewinkel, H. Schottmüller and T. Viehoff [1996] PELICON: Project for estimation of long-term variability of ice concentration. *Tech. Report Contract EV5V-CT93-0268 (DG I2)*, European Community, EC.
- Holdsworth, G. [1977] Tidal interaction with ice shelves. *Ann. Geophys.*, **33**, 133–146.
- Holloway, P. E. [1985] A comparison of semi-diurnal internal tides from different bathymetric locations on the Australian North West Shelf. *J. Phys. Ocean.*, **15**, 240–251.
- Holloway, P. E. [1996] A numerical model of internal tides with application to the Australian North West Shelf. *J. Phys. Oceanogr.*, **26**, 21–37.
- Holloway, P. E. and B. Barnes [1998] A numerical investigation into the bottom boundary layer flow and vertical structure of internal waves on a continental slope. *Cont. Shelf Res.*, **18**, 31–65.

- Holloway, P. E. and M. A. Merrifield [1999] Internal tide generation by seamounts, ridges and islands. *J. Geophys. Res.*, **104**(C11), 25,937–25,951.
- Huthnance, J. M. [1989] Internal tides and waves near the continental shelf edge. *Geophys. Astrophys. Fluid Dyn.*, **48**, 81–106.
- Huthnance, J. M. [1995] Circulation, exchange and water masses at the ocean margin: the role of physical processes at the shelf edge. *Prog. Oceanog.*, **35**, 353–431.
- Ivey, G. N. and R. I. Nokes [1989] Vertical mixing due to the breaking of critical internal waves on sloping boundaries. *J. Fluid Mech.*, **204**, 479–500.
- Jenkins, A. [1991] A one-dimensional model of ice shelf-ocean interaction. *J. Geophys. Res.*, **96**(C11), 20,671–20,677.
- Jenkins, A. and C. S. M. Doake [1991] Ice-ocean interaction on Ronne Ice Shelf, Antarctica. *J. Geophys. Res.*, **96**(C1), 791–813.
- Johnson, M. R. and A. M. Smith [1997] Seabed topography under the southern and western Ronne Ice Shelf. *Antartic Science*, **9**, 201–208.
- Kantha, L. H. [1995] Barotropic tides in the global oceans from a nonlinear tidal model assimilating altimetric tides 1. Model description and results. *J. Geophys. Res.*, **100**(C12), 25,283–25,308.
- Kantha, L. H. and C. C. Tierney [1997] Global baroclinic tides. *Prog. Oceanog.*, **40**, 163–178.
- Kowalik, Z. and A. Y. Proshutinsky [1994] The Arctic Ocean Tides. In: *The Polar Oceans and Their Role in Shaping the Global Environment* (edited by Johannessen, O. M., R. D. Muench and J. E. Overland), volume 85 of *Geophysical Monograph*, pp. 137–158. American Geophysical Union.
- Launiainen, J. and T. Vihma [1994] On the surface heat fluxes of the Weddell Sea. In: *The Polar Oceans and Their Role in Shaping the Global Environment* (edited by Johannessen, O. M., R. D. Muench and J. E. Overland), volume 85 of *Geophysical Monograph*, pp. 399–419. American Geophysical Union.
- Laurent, L. S. and C. Garrett [2001] The role of internal tides in mixing the deep ocean. *J. Phys. Ocean.*. Submitted.

- LeBlond, P. H. [1966] On the damping of internal gravity waves in a continuously stratified ocean. *J. Fluid Mech.*, **25**, 121–142.
- LeBlond, P. H. and L. A. Mysak [1978] *Waves in the Ocean*, volume 20 of *Elsevier Oceanography Series*. Elsevier, Amsterdam.
- Levine, M. D., L. Padman, R. D. Muench and J. H. Morison [1997] Internal waves and tides in the western Weddell Sea: observations from Ice Station Weddell. *J. Geophys. Res.*, **102**(C1), 1073–1089.
- Lewis, E. L. and R. G. Perkin [1986] Ice pumps and their rates. *J. Geophys. Res.*, **91**(C10), 11,756–11,762.
- Maas, L. R. M. [2001] Wave focusing and ensuing mean flow due to symmetry breaking in rotating fluids. *submitted to J. Fluid Mech.*.
- Maas, L. R. M. and J. T. F. Zimmerman [1989a] Tide-topography interactions in a stratified shelf sea I. Basic equations for quasi-nonlinear internal tides. *Geophys. Astrophys. Fluid Dyn.*, **45**, 1–35.
- Maas, L. R. M. and J. T. F. Zimmerman [1989b] Tide-topography interactions in a stratified shelf sea II. Bottom trapped internal tides and baroclinic residual currents. *Geophys. Astrophys. Fluid Dyn.*, **45**, 37–69.
- MacAyeal, D. R. [1984a] Numerical simulations of the Ross Sea tides. *J. Geophys. Res.*, **89**(C1), 607–615.
- MacAyeal, D. R. [1984b] Thermohaline circulation below the Ross Ice Shelf: a consequence of tidally induced vertical mixing and basal melting. *J. Geophys. Res.*, **89**(C1), 597–606.
- Makinson, K. [2001] Modeling tidal currents profiles and vertical mixing beneath Filchner-Ronne Ice Shelf, Antarctica. *J. Phys. Ocean.* Submitted.
- Makinson, K. and K. W. Nicholls [1996] Modelling tidal currents beneath Filchner-Ronne Ice Shelf. Number 10 in Filchner-Ronne Ice Shelf Programme, pp. 58–67. Alfred-Wegener Institute for Polar and Marine Research, Bremerhaven.

- Makinson, K. and K. W. Nicholls [1999] Modeling tidal currents beneath Filchner-Ronne Ice Shelf and on the adjacent continental shelf: their effect on mixing and transport. *J. Geophys. Res.*, **104**(C6), 13,449–13,465.
- Martinsen, E. A. and H. Engedahl [1987] Implementation and testing of a lateral boundary scheme as an open boundary condition in a barotropic ocean model. *Coastal Eng.*, **11**, 603–627.
- Mellor, G. L. and T. Yamada [1982] Development of a turbulent closure model for geophysical fluid problem. *Rev. Geophys.*, **20**, 851–875.
- Mensch, M., R. Bayer, J. L. Bullister, P. Schlosser and R. F. Weiss [1996] The distribution of tritium and CFCs in the Weddell Sea during the mid-1980s. *Prog. Oceanog.*, **38**, 377–415.
- Meredith, M. P., A. J. Watson, K. A. V. Scoy and T. W. N. Haine [2001] Chlorofluorocarbon-derived formation rates of deep and bottom waters of the Weddell Sea. *J. Geophys. Res.*, **106**(C2), 2899–2919.
- Middleton, J. H. and T. Denniss [1993] The propagation of tides near the critical latitude. *Geophys. Astrophys. Fluid Dyn.*, **68**, 1–13.
- Middleton, J. H. and T. D. Foster [1977] Tidal currents in the central Weddell Sea. *Deep-Sea Res.*, **24**, 1195–1202.
- Middleton, J. H., T. D. Foster and A. Foldvik [1982] Low-frequency and continental shelf waves in the southern Weddell Sea. *J. Phys. Oceanogr.*, **12**, 618–634.
- Middleton, J. H., T. D. Foster and A. Foldvik [1987] Diurnal shelf waves in the southern Weddell Sea. *J. Phys. Oceanogr.*, **17**, 784–791.
- Miles, J. W. [1974] On Laplace's tidal equations. *J. Fluid Mech.*, **66**(2), 241–260.
- Munk, W. [1966] Abyssal recipes. *Deep Sea Res.*, **13**, 707–730.
- Munk, W. and C. Wunsch [1998] Abyssal recipes II: energetics of tidal and wind mixing. *Deep Sea Res. I*, **45**, 1977–2010.
- Nicholls, K. W. [1996] Temperature variability beneath Ronne Ice Shelf, Antarctica. *J. Geophys. Res.*, **101**(C1), 1199–1210.

- Nøst, E. [1994] Calculating tidal current profiles from vertically integrated models near the critical latitude in the Barent Sea. *J. Geophys. Res.*, **99**(C4), 7885–7901.
- Orsi, A. H., G. C. Johnson and J. L. Bullister [1999] Circulation, mixing, and production of Antarctica Bottom Water. *Prog. Oceanog.*, **43**, 55–109.
- Padman, L. and C. Kottmeier [2000] High-frequency ice motion and divergence in the Weddell Sea. *J. Geophys. Res.*, **105**(C2), 3379–3400.
- Pekeris, C. L. and Y. Accad [1969] Solution of Laplace's equations for the M_2 tide in the world oceans. *Philos. Trans. R. Soc. London*, **265**(1165), 413–436.
- Pérenne, N., A. Pichon and P. Huet [2000] A numerical study of stratified tidal rectification. *Cont. Shelf Res.*, **20**, 37–68.
- Petterson, O. [1907] Sturmstudien vid Östersjöns portar. *Inst. Mar. Res. Lysekil Ser. Biol. Rep.*, **3**.
- Polzin, K. L., J. M. Toole, J. R. Ledwell and R. W. Schmitt [1997] Spatial variability of turbulent mixing in the abyssal ocean. *Science*, **276**, 93–96.
- Pond, S. and G. L. Pickard [1978] *Introductory Dynamical Oceanography*. Butterworth-Heinemann Ltd., Oxford, England.
- Potter, J. R., J. G. Paren and M. Pedley [1985] Tidal behaviour under an Antarctic ice shelf. *Br. Antarc. Survey Bull.*, **68**, 1–18.
- Prandle, D. [1982] The vertical structure of tidal currents. *Geophys. Astrophys. Fluid Dyn.*, **22**, 29–49.
- Prinsenbergh, S. J. and E. B. Bennett [1989] Vertical variations of tidal currents in shallow land fast ice-covered regions. *J. Phys. Ocean.*, **19**, 1268–1278.
- Prinsenbergh, S. J. and M. Rattray, Jr [1974] Generation and dissipation of coastal internal tides. *Deep-Sea Res.*, **21**, 263–281.
- Pugh, D. T. [1987] *Tides, surges and mean sea level: a handbook for engineers and scientists*. John Wiley and Sons Ltd., Swindon.

- Ray, R. [1993] Global ocean tide models on the eve of TOPEX/POSEIDON. *IEEE Trans. Geosci. Remote Sens.*, **31**(2), 355–364.
- Rignot, E., L. Padman, D. R. MacAyeal and M. Schmeltz [2000] Observation of ocean tides below the Filchner and Ronne Ice Shelves, Antarctica, using synthetic aperture radar interferometry: comparison with tide model predictions. *J. Geophys. Res.*, **105**(C8), 19,615–19,630.
- Robertson, R. [2001] Internal tides and baroclinicity in the southern Weddell Sea. Part I: Model description. *J. Geophys. Res.*, **106**(C12), 27,001–27,016.
- Robertson, R., L. Padman and G. D. Egbert [1998] Tides in the Weddell Sea. In: *Ocean, Ice, and Atmosphere: Interactions at the Antarctic Continental Margin* (edited by Jacob, S. S. and R. Weiss), volume 75 of *Antarctic Research Series*, pp. 341–369. American Geophysical Union, Washington, DC.
- Robinson, A., K. Makinson and K. W. Nicholls [1994] The oceanic environment beneath the northwest Ronne Ice Shelf, Antarctica. *Ann. Glac.*, **20**, 386–390.
- Robinson, I. S. [1981] Tidal vorticity and residual circulation. *Deep-Sea Res.*, **28A**(3), 195–212.
- Saint-Guily, B. [1976] Sur la propagation des ondes de seconde class le long d'un talus continental. *C. R. Acad. Sci. Paris*, **B282**, 141–144.
- Scheduikat, M. and D. J. Olbers [1991] A one-dimensional mixed layer model beneath the Ross Ice Shelf with tidally induced vertical mixing. *Antarct. Sci.*, **2**(1), 29–42.
- Schenke, H. W., H. Hinze, S. Dijkstra, B. Hoppmann, F. Niederjasper and T. Schne [1998] The new bathymetric charts of the Weddell Sea: AWI BCWS. In: *Ocean, Ice, and Atmosphere* (edited by Jacobs, S. S. and R. F. Weiss), volume 75 of *Antarctic Research Series*, pp. 373–382. American Geophysical Union, Washington, D.C.
- Schott, F. [1977] On the energetics of baroclinic tides in the North Atlantic. *Geophys. Res. Letters*, **33**, 41–62.
- Schwiderski, E. W. [1980] On charting global ocean tides. *Rev. Geophys. Space Phys.*, **18**(1), 243–268.

- Shum, C. K., P. L. Woodworth, O. B. Andersen, G. D. Egbert, C. K. O. Francis, C. L. P. S. M. Klosko, X. Li, J.-M. Molines, M. E. Parke, R. D. Ray, M. G. Schlax, D. Stammer, C. C. Tierney, P. Vincent and C. I. Wunsch [1997] Accuracy assessment of recent ocean tide models. *J. Geophys. Res.*, **102**(C11), 25,173–25,194.
- Smith, W. H. F. and D. T. Sandwell [1997] Global sea floor topography from satellite altimetry and ship depth soundings. *Science*, **277**, 1956–1962.
- Smithson, M. J., R. A. Flather and A. V. Robinson [1995] Tidal modelling under the Filchner-Ronne Ice Shelf. *Ann. Geophys.*, **13**(Supplement II), C261.
- Smithson, M. J., A. V. Robinson and R. A. Flather [1996] Ocean tides under the Filchner-Ronne Ice Shelf, Antarctica. *Ann. Glaciol.*, **23**, 217–225.
- Song, Y. and D. B. Haidvogel [1994] A semi-implicit ocean circulation model using a generalized topography-following coordinate system. *J. Comput. Phys.*, **115**(C1), 228–244.
- Thiel, E., A. P. Crary, R. A. Haubrich and J. C. Behrendt [1960] Gravimetric determination of ocean tide, Weddell and Ross Seas, Antarctica. *J. Geophys. Res.*, **65**(2), 629–636.
- Thomson, R. E. and W. R. Crawford [1982] The generation of diurnal period shelf waves by tidal currents. *J. Phys. Ocean.*, **12**, 635–643.
- Timmermann, R., A. Beckmann and H. H. Hellmer [2001] Simulation of ice-ocean dynamics in the Weddell Sea. Part I: model configuration and validation. *submitted to J. Geophys. Res.*.
- Vaughan, D. G. [1995] Tidal flexure at ice shelf margins. *J. Geophys. Res.*, **100**(B4), 6213–6224.
- Wahr, J. M. [1981] Body tides on an elliptical rotating, elastic and oceanless Earth. *Geophys. J. R. Astron. Soc.*, **64**, 677–703.
- Wahr, J. M. [1988] The Earth's rotation. *Annu. Rev. Earth Planet. Sci.*, **16**, 231–249.
- Webb, D. J. and N. Sugimotohara [2001] Vertical mixing in the ocean. *Nature*, **409**, 37.

- Weigand, J. G., H. G. Farmer, S. J. Prinsenbergh and M. Rattray, Jr [1969] Effects of friction and surface tide angle of incidence on the coastal generation of internal tides. *J. Mar. Res.*, **27**, 241–259.
- Whewell, W. [1833] Towards a first approximation to a map of cotidal lines. *Philos. Trans. R. Soc. London*, **123**, 147–236.
- Whewell, W. [1836] On the results of an extensive system of tide observations made on the coasts of Europe and America in June 1835. *Philos. Trans. R. Soc. London*, **126**, 289–341.
- Woodgate, R. A., M. Schröder and S. Østerhus [1998] Moorings from the Filchner Trough and the Ronne Ice Shelf Front. Number 12 in Filchner-Ronne Ice Shelf Programme, pp. 85–90. Alfred-Wegener Institute for Polar and Marine Research, Bremerhaven.
- Wunsch, C. [1975] Internal tides in the ocean. *Rev. Geophys. Space Phys.*, **13**(1), 167–182.
- Xing, J. and A. M. Davies [1998] A three-dimensional model of internal tides on the Malin-Hebrides shelf and shelf-edge. *J. Geophys. Res.*, **103**(C12), 27,821–27,847.
- Zeilon, N. [1934] Experiments on boundary tides. *Göteborgs Kgl. Vetensk. Vitterhets Samhälles Handl.*, **5**, 1–8.